Voyages on the Frontier: Exploring competing orders in strongly correlated lattice models

A Dissertation Presented for the

Doctor of Philosophy

Degree

The University of Tennessee, Knoxville

Andy Tanjaroon Ly

August 2026

© by Andy Tanjaroon Ly, 2026
All Rights Reserved.

For my great aunt Nab,

and for Lillie

It is the struggle itself that is most important. We must strive to be more than we are. It does not matter that we will not reach our ultimate goal. The effort itself yields its own reward.

Gene Roddenberry

ACKNOWLEDGEMENTS

I always joked that it takes a very special kind of person to complete a Ph.D. in physics; I suppose that the joke is now on me.

First and foremost, I would like to express my sincerest gratitude to my advisor Prof. Steven Johnston. When I first joined UTK, I was unsure what kind of research would be a good fit for me. That was until I attended the research seminar for new graduate students where Steve talked about the research his group did. He warned me that the learning curve would be appreciable but encouraged me every step of the way. I especially thank him for putting up with all of the mistakes I made while always pushing me towards success.

I would like to thank all of the consummate professionals that I have encountered in my travels. First, to Prof. Louk Rademaker, for hosting me while I lived in Geneva, challenging me to look at problems from different perspectives, and encouraging me to network. Special thanks to Profs. Thierry Giamarchi and Christophe Berthod for lively lunch discussions, even those that did not involve physics. Thank you to Dr. Thomas Maier, for hosting me at ORNL and setting a prime example of what it means to be a world-class physicist and always providing his signature dry wit. Special thanks to my friend and colleague Dr. Philip Dee, for our thought-provoking yet often humorous lunches together at IAMM and ORNL. Perhaps this form of communication was merely to maintain connections...or something like that.

Now, an ode to the other people that I've encountered during the course of my time in grad school. To my fellow friends and colleagues of the IAMM/South College office: Dr. Ben Cohen-Stead, for insightful discussions on the Julia programming language and begin each others' "rubber ducks" while debugging our respective software packages. Also, for putting up with me while stuck at the Harry Reid airport after a long and eventful March meeting; Sohan, with whom I ruminated on the nature of life and food with (especially those "useless" animals); Harini, for always being kind, always messaging me when a cool new restaurant opens in town,

and always willing to talk about *The Legend of Zelda: Tears of the Kingdom*; Jinu, for the fun times we had exploring Chicago, where I was mistaken for a local, despite the fact that you had lived in Chicago. And for support we gave each other in the face of grueling postdoc applications; James, for giving me advice in life in addition to always making us laugh. Outside of the office, I offer special thanks to Lucas, for the absolutely brutal games of Uno, caring for our cats, and always being down for a trip to Yassin's or Waffle House. The biggest thanks of all to my fellow expat friends: Rea, Naomi, Lorenzo, Sofia, Rob, Sanje, and those at UNIGE: Guilia, Michael, and Dario. You all made my time abroad a special one.

To my family, particularly my uncle Chakree who inspired me to travel down the path of science. To my parents, thank for letting me pursue anything that I wanted, providing world-class encouragement, and making some of the best food in the world. And of course, I have to thank my tireless partner Daniel, who puts up with me despite that fact that I work in condensed matter and not particle physics. For being there for me at my highest and lowest moments. You are my star, my perfect silence.

Finally, I would to thank my cats Max and Lillie and all of the comfort they brought at the end of a long day of writing or debugging, whether I wanted it or not.

ABSTRACT

Understanding the microscopic origin of high-temperature superconductivity in the cuprates remains on the frontier of condensed matter physics. While BCS theory successfully describes conventional superconductors, it fails to capture the behavior of the cuprate materials, which host a complex phase diagram including antiferromagnetic, pseudogap, strange metal, and charge- and spin-ordered phases alongside unconventional superconductivity. Low-energy effective models such as the Hubbard model have been widely employed to study these intertwined orders; however, questions persist regarding whether such models alone can capture the essential physics of the cuprates. In particular, nonperturbative numerical studies frequently find nearly degenerate stripe and superconducting ground states, and results can be sensitive to model parameters such as next-nearest-neighbor hopping. Moreover, experimental evidence from angle-resolved photoemission spectroscopy, resonant inelastic X-ray scattering, and scanning tunneling microscopy points to a significant role for electron-phonon interactions.

This dissertation explores the interplay between electron-electron and electron-phonon interactions through three related studies using state-of-the-art numerical methods. First in Chapter 3, the effect of Holstein phonon coupling on stripe and uniform d-wave superconducting states in the Hubbard model is examined using variational Monte Carlo (VMC) at zero temperature and determinant quantum Monte Carlo (DQMC) at finite temperature. In Chapter 4, a systematic comparison of pairing correlations across the Holstein, bond-, and optical-Su-Schrieffer-Heeger models is carried out using DQMC, including an assessment of recent claims regarding SSH-driven bipolaronic superconductivity. Finally in Chapter 5, a ground state phase diagram of the Su-Schrieffer-Heeger-Hubbard model is mapped out through finite-size scaling analysis of DQMC data, revealing a potential coexistence region between antiferromagnetic (AFM) and bond-order-wave (BOW) states. Together, these studies refine our understanding of how lattice interactions modify

strongly correlated behavior in the Hubbard model and expand the body of knowledge on the less-explored SSH-type electron-phonon models, contributing toward a more complete theoretical description of the cuprate superconductors and related materials.

TABLE OF CONTENTS

1 Introduction 1

1.1 Roadmap of this dissertation 7

2 Models & Methods 9

2.1 The Hubbard model 9

2.2 Models of electron-phonon interaction 10

2.2.1 The Holstein model 12

2.2.2 The Su-Schrieffer-Heeger model 13

2.2.3 The dimensionless electron-phonon coupling constant 14

2.3 Monte Carlo methods 16

2.3.1 Variational Monte Carlo 17

2.3.2 Trial wavefunctions for VMC 23

2.3.3 Determinant Quantum Monte Carlo 28

2.3.4 Assessing system properties using DQMC 36

3 Stripe correlations in the two-dimensional Hubbard-Holstein model . . 37

3.1 Introduction 37

3.2 Results 39

3.3 Discussion 52

4 Comparative study of the superconductivity in the Holstein and optical Su-Schrieffer-Heeger models 55

4.1 Introduction 55

4.2 Results 57

4.3 Discussion 66

5 Antiferromagnetic and bond-order-wave phases in the half-filled two-dimensional optical Su-Schrieffer-Heeger-Hubbard model 69

5.1 Introduction 69

5.2 Results . . . 71
5.3 Discussion . . . 80

6 Conclusions . . . 83
6.1 Open Problems and Future Work . . . 85
6.1.1 Stripes in the Hubbard-SSH model . . . 85
6.1.2 The relative importance of anharmonic terms . . . 86
6.2 Final Remarks . . . 87

Bibliography . . . 88

Appendices . . . 114

A Spin and charge stripe evolution in VMC and DQMC simulations . . . 115

B Finite size effects in VMC simulations . . . 121

C Sign changes in the effective hopping integral in the Su-Schrieffer-Heeger model . . . 123

D The Fermion sign problem and finite size effects in DQMC simulations . . . 125

E Effective interaction of the optical SSH model in the anti-adiabatic limit . . . 129

F Additional observables in the SSH-Hubbard model . . . 132

Citations to Published Work . . . 136

Vita . . . 138

LIST OF TABLES

1 Local updates to Fermions with the Metropolis algorithm 20
2 Stochastic Reconfiguration 20
3 Overview of the VMC simulation structure 24
4 Overview of DQMC simulation structure 35

A.1 The type of stripe correlations found in our VMC calculations, distinguishing between bond- and site-centered. 115

LIST OF FIGURES

1.1 Schematic phase diagram of the cuprates. 4

1.2 Schematic diagram of cuprate "stripes". 6

2.1 Illustration of the Hubbard and Holstein models in two-dimensions. 11

2.2 Illustration of the *optical* and *bond* Su-Schrieffer-Heeger models in two-dimensions. 15

3.1 Variational Monte Carlo (VMC) results for static stripe order in the two-dimensional Hubbard-Holstein model. 40

3.2 Variational Monte Carlo estimates for the energies of the two-dimensional Hubbard-Holstein model with $t' = 0$ and various phonon energies Ω as a function of λ. 43

3.3 Variational Monte Carlo estimates for the energies of the two-dimensional Hubbard-Holstein model with $t' = -0.25t$ and various phonon energies Ω as a function of λ. 44

3.4 The energy per hole $\varepsilon(\delta)$ for $t' = -0.25t$ and $t' = 0$ (insets) at different phonon energies. 47

3.5 Determinant quantum Monte Carlo results for the fluctuating spin and charge stripes in the Hubbard-Holstein model. 49

3.6 Determinant quantum Monte Carlo results for the fluctuating spin and charge stripes of the Hubbard-Holstein model in momentum space. 50

4.1 DQMC results for pairing and dominant charge/bond correlations obtained on 14×14 lattices at $\beta = 16/t$ and $\lambda = 0.3$. 58

4.2 (a) The expectation value of the number operator $\langle n_{k,\sigma} \rangle$ for the optical-SSH model as a function of λ, plotted along the $k = (k_x, 0)$ direction of the first Brillouin zone (FBZ). (b) The effective mass $m^*(k)/m$ along $(k_x, 0)$ for the Holstein (red $\bigcirc$), optical- (blue $\square$), and bond-SSH (black $\triangle$) models for $\lambda = 0.3$. 62

4.3 DQMC results for the Holstein (red ○), and bond-, (blue □), and optical- (black △) SSH models. 63
4.4 A comparison of the temperature dependence of the s-wave pair-field susceptibilities for the Holstein (red ○), and bond- (blue □), and "optical" SSH (oSSH) (black △) models at fixed $\lambda = 0.3$ and $\langle n \rangle = 0.7$. 64
4.5 The temperature dependence of the uniform s-wave and extended s-wave pair-field susceptibilities. 67
5.1 Phase diagram of the optical SSH-Hubbard model at half-filling $\langle n \rangle = 1$ with a fixed phonon frequency $\Omega/t = 0.5$. 72
5.2 Correlation ratios for the (a) bond-ordered-wave and (b) antiferromagnetic phases as a function of λ for fixed $U/t = 3$. 73
5.3 Correlation ratios for the bond-ordered-wave and antiferromagnetic orders as a function of λ for the pure oSSH model ($U/t = 0$). 75
5.4 A summary of several local observables for the optical Su-Schrieffer-Heeger (SSH)-Hubbard model. 77
5.5 Finite temperature susceptibilities in different regions of the phase diagram. 79

A.1 Variational Monte Carlo results for static spin and charge stripes in the Hubbard-Holstein model with $U = 8t$ and $t' = 0$. 116
A.2 Variational Monte Carlo results for static spin and charge stripes in the Hubbard-Holstein model with $U = 8t$ and $t' = -0.25t$. 117
A.3 The evolution of the antiferromagnetic (left) and d-wave superconducting order parameters. 118
A.4 DQMC results for the fluctuating spin stripes in the Hubbard-Holstein model at a filling of $\langle \hat{n} \rangle = 0.8$ and an inverse temperature of $\beta = 4/t$ and obtained on $N = 16 \times 4$ clusters with $t' = -0.25t$ and $U = 6t$. . . 119

A.5 DQMC results for the fluctuating charge stripes in the Hubbard-Holstein model at a filling of $\langle \hat{n} \rangle = 0.8$ and an inverse temperature of $\beta = 4/t$ and obtained on $N = 16 \times 4$ clusters with $t' = -0.25t$ and $U = 6t$. 119
A.6 DQMC results of the ratio between spin and charge incommensurability $r = \delta_s/\delta_c$ in the Hubbard-Holstein model at a filling of $\langle \hat{n} \rangle = 0.8$ and an inverse temperature of $\beta = 4/t$. 120
A.7 DQMC results for the fluctuating charge stripes in the Hubbard-Holstein model at a filling of $\langle \hat{n} \rangle = 0.8$ and an inverse temperature of $\beta = 4/t$ and obtained on $N = 16 \times 4$ clusters with $t' = -0.25t$ and $U = 6t$. 120

B.1 The energies of the variational wave functions obtained on $16 \times L_y$ clusters with model parameters $t' = -0.25t$, $U = 8t$, $\Omega = t$, and $\lambda = 0.25$. 122

C.1 Sign switching of the hopping integral as a function of filling for (a) the bond-SSH model in the x-direction (closed $\square$) and in the y-direction (open $\square$). 124

D.1 The average value of the Fermion sign obtained for the simulations with $U = t/2$ presented in Fig. 4.5 of Chapter 4. 126
D.2 All panels are DQMC results for $\Omega = 4t$, $\lambda = 0.3$ at $\beta t = 16$ on different $L \times L$ lattices. 128

F.1 The (a) compressibility κ and (b) local single particle Green's function $\beta G(r = 0, \tau = \beta/2)$ for the optical SSH-Hubbard model as a function of λ and U. 133
F.2 (a) Bond-ordered-wave and (b) antiferromagnetic (AFM) correlation ratios for $U/t \in (0, 8)$. 134

F.3 Antiferromagnetic susceptibility χ_{AFM} for $L = 14$, $\Omega/t = 0.5$ and 2, $\beta t = 14$ and $\beta t = 28$ compared to the non-interacting solution (black dotted line). 135

CHAPTER 1:
INTRODUCTION

The most elementary and valuable statement in science,
the beginning of wisdom, is, "I do not know".
— Lt. Cmdr. Data, *Star Trek: The Next Generation*

In the field of physics, there are a vast number of topics which have been classified as being on the "frontier", problems whose answers still lie in the unknown. Physicists serve as the explorers of these frontiers, boldly charting a course through unknown territory. Within condensed matter physics, perhaps there is no greater frontier than that of superconductivity. On the surface, this seems paradoxical in nature, as there historically have been successful theories that describe their properties. High-temperature or high-T_c superconductors, have fascinated and confounded physicists since their discovery. What makes these materials so different that their microscopic properties cannot be explained by a highly reproduced theory? A great many number of explorers in this area have made great progress, but are we any closer to a definitive answer than we were since the beginning of it all? Such questions bear investigation.

The first person to chart a course into this great frontier was the Dutch physicist Heike Kammerlingh Onnes. In his laboratory at Leiden University in 1911, Onnes submerged a piece of solid mercury wire in liquid helium and observed that the resistance of the wire dropped to zero at 4.2 K [1]. Onnes recognized that the mercury wire had passed on to a new "superconductive state", becoming the first person to discover this phenomenon. After his initial discovery, other superconducting materials would be identified, thanks in part to the helium refrigeration technique that he devised. While Onnes went on to win a Noble prize in 1913, others would continue the journey that he started. Peering into the further properties of superconductors, William Meissner and Robert Ochsenfeld

found in 1933 that superconducting materials expelled magnetic fields [2]. This phenomenon is recognizable today as the *Meissner effect*. Soon after in 1935, a phenomenological breakthrough was made by the brothers Fritz and Heinz London. Looking for an explanation for the Meissner effect, they showed that the free energy in a superconductor is minimized when the magnetic field is expelled [2]. While these early explorers made incremental progress in experimenting with this new form of conductivity, any cohesive theory remained absent until 1950, when Lev Landau and Vitaly Ginzburg formulated the first phenomenological theory of superconductivity [2]. The *Ginzburg-Landau theory* found its basis in phase transitions and provided a framework for describing the macroscopic properties of superconductors. This theory also gave rise to the classification of superconductors into two types. Type-I superconductors are elemental and characterized by their persistent Meissner effect below their critical temperature and critical magnetic field. Type-II superconductors are compounds and differ from type-I in that they allow for the existence of a state in between the two critical magnetic field values (upper and lower) and experience partial flux penetration. It would not be until 1957 that a successful microscopic theory of superconductivity would be discovered by the intrepid explorers John Bardeen, Leon Cooper, and John Schrieffer (BCS). The *BCS theory* [3] explained that superconductivity was due to the manifestation of a superfluid of "Cooper pairs", electrons which were bound together by interactions with phonons. In great synergy just two years later, Lev Gor'kov [4] showed that BCS theory reduced to the Ginzburg-Landau theory when near the superconducting critical temperature. BCS theory was hailed as a massive success, particularly for type-I superconductors, and Bardeen, Cooper, and Schrieffer were awarded a Nobel prize in 1972. While the search for other superconductors continued with this new theory in hand, another major breakthrough would happen in the 1980s.

Most superconducting materials found before 1986 had transition temperatures which did not exceed 20 K. Though these temperatures were accessible thanks to the work of Onnes, practical applications of superconductivity were hindered by

the necessity for extremely low temperatures. That was until the discovery made by yet another set of explorers, Georg Bednorz and Karl Alex Müller. At their IBM laboratory near Zürich, Bednorz and Müller observed something remarkable: a ceramic material whose superconducting transition temperature was 35 K. The perovskite material, known as Lanthanum Barium Copper Oxide (LBCO) [5], was the first copper oxide or "cuprate" superconductor. Just a year later in 1987, further work showed that replacing Lanthanum with Yttrium raised the critical temperature to 90 K [6], just above the boiling point of liquid nitrogen (77 K). These represented a turning point in the study of superconductors and the discovery of LBCO earned Bednorz and Müller a Noble prize that same year.

The question now becomes: like the elemental superconductors that came before, is there a cohesive microscopic theory of the cuprates? One of the earliest attempts was by the late, great Philip W. Anderson with his Resonating Valence Bond theory, but it was not enough; the journey was far from over. The quest to understand the cuprates, and by extension other high-T_c superconductors, has garnered even more explorers since the time of Bednorz and Müller. Many have tried different avenues and techniques, sometimes inciting more questions than before. And while some may consider the problem of the cuprates to be an old one, it is undeniable that it remains an interesting one, and that it behooves us as explorers of this frontier to apply our past knowledge and our current technologies into this endeavor.

The exploration has continued by those who aim to map out and understand other orders in the cuprates [7]. While these materials are most famous for their superconductivity (SC), there also exist many other interesting orders as shown in Figure 1.1, including antiferromagnetic (AFM), pseudogap (PG), strange metal (SM), and Fermi liquid (FL). There also exist interesting spin and charge orders denoted by "SO" and "CO", respectively. Neutron scattering experiments [8, 9] on $La_{1.48}Nd_{0.4}Sr_{0.12}CuO_4$ and $La_{1.875}Ba_{0.125}CuO_4$ have revealed regions of antiferromagnetism separated by anti-phase domain walls known as "stripes", (Fig. 1.2) which appear as the system is hole-doped. These coexisting

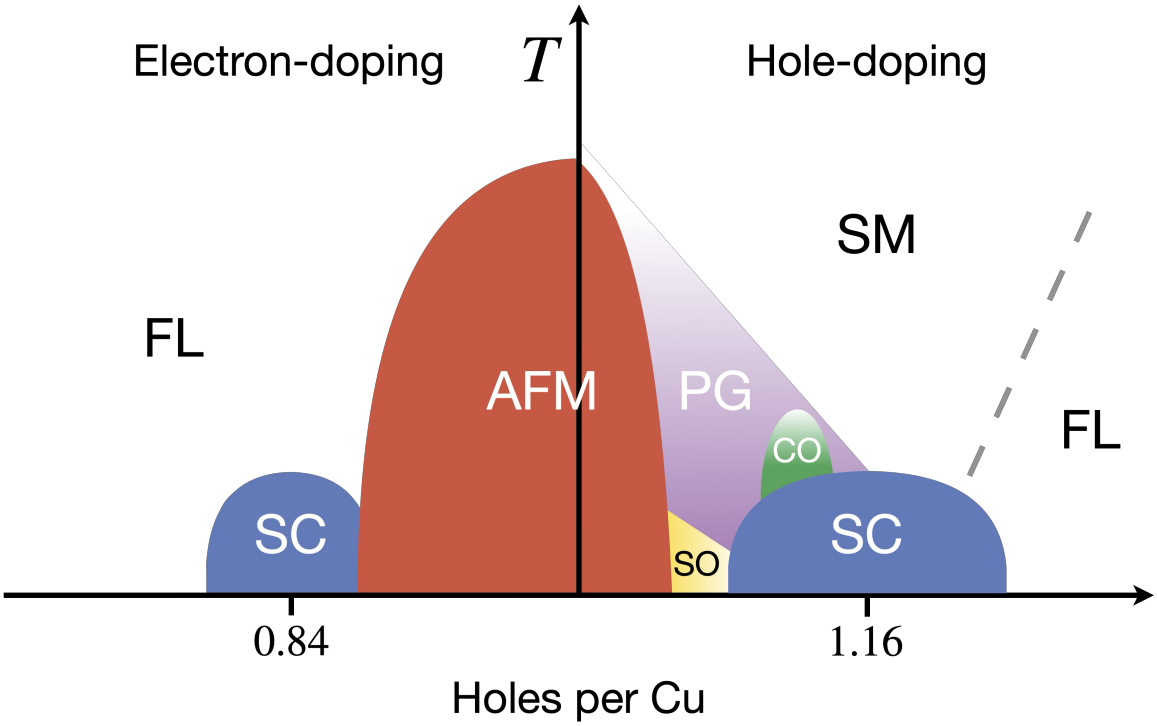

Figure 1.1: Schematic phase diagram of the cuprates.

charge and spin orders have also been observed in resonant soft X-ray scattering and muon spin spectroscopy experiments [10, 11]. It remains a question whether such orders compete or cooperate with unconventional superconductivity [8]. Studies of low-energy effective (or "toy") models, such as the famed Hubbard model [12], have also observed this stripe phenomenon. For example, non-perturbative numerical studies of at zero temperature [13–17] often identify several nearly degenerate stripe and superconducting states using model parameters relevant to the cuprates.

The matter of which state, stripe or superconducting, is the ground state can be sensitive to model parameters. This is seen through the addition of next nearest-neighbor hopping, t' [15, 19], in these "toy" models. A rather large question that remains pertains to whether the Hubbard model is the correct model for describing the cuprates [20–22]. For instance, density matrix renormalization group (DMRG) studies on multi-leg, hole-doped Hubbard ladders with a finite t', find a superconducting ground state [15]; however, these results do not have the correct $d_{x^2-y^2}$ pairing symmetry [23] consistent with the cuprates [24]. On the other hand, DMRG studies on six- and eight-leg *t-J* cylinders obtain the correct pairing symmetry, albeit on the electron-doped side of the phase diagram [25]. Such results cast doubt on the notion that the hole-doped cuprates can be described solely by the Hubbard model.

Another set of ongoing questions is whether electron-phonon (e-ph) coupling is a missing ingredient in the description of different systems, and how they could influence the behavior of phases seen in the Hubbard model. In addition to strong correlations, e-ph interactions have been observed in different cuprates in angle resolved photoemission spectroscopy [26, 27], resonant inelastic X-ray scattering [28, 29], and scanning tunneling microscopy [30, 31] experiments. The vibrational modes observed in the cuprates are the oxygen bond-buckling [32] and bond-stretching [33, 34] modes. Buckling vibrations can be modeled by the Holstein interaction, where the lattice is allowed to couple to local charge density [35]. The Holstein model has been extensively studied [36–38]; specifically

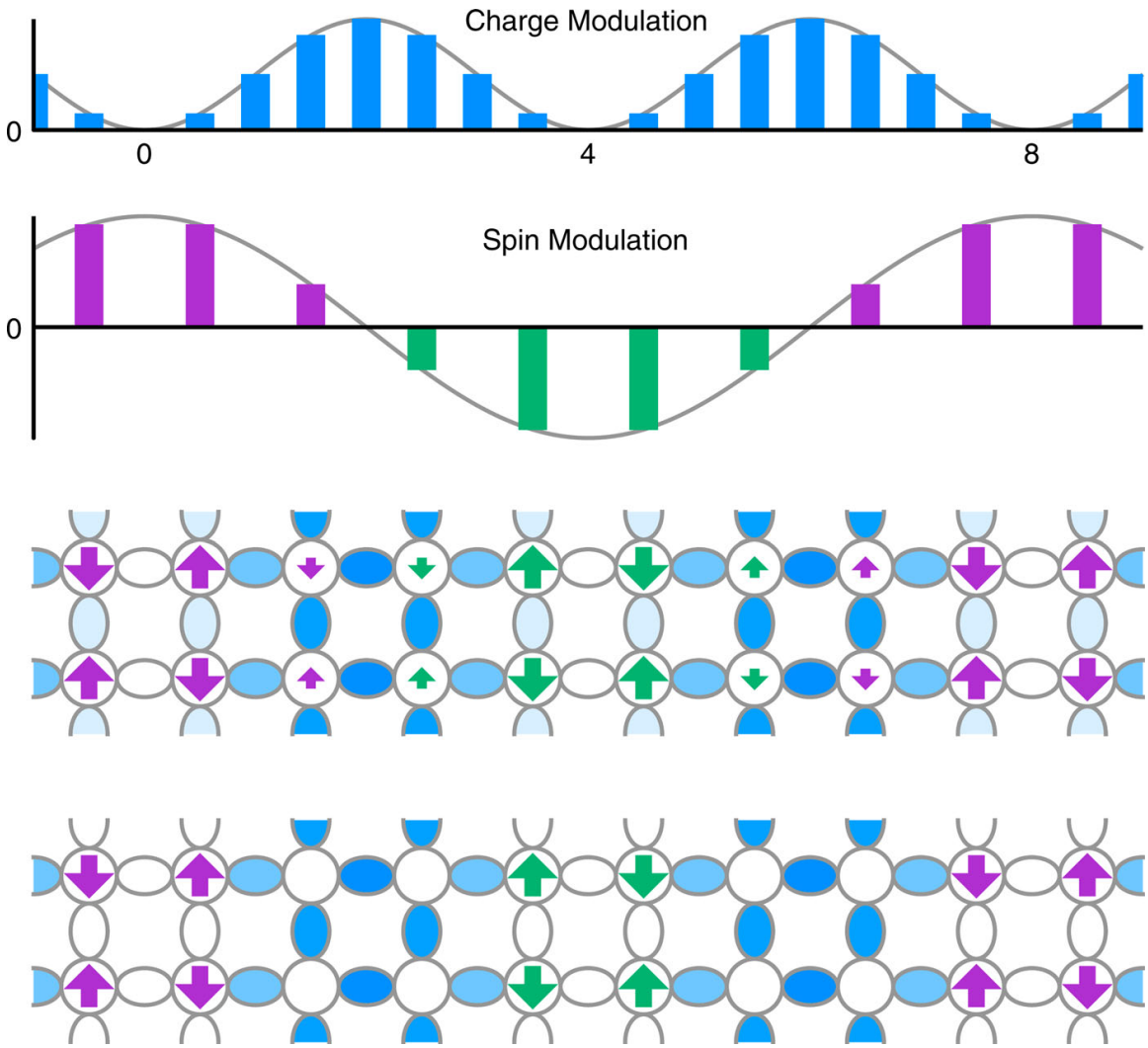

Figure 1.2: Schematic diagram of cuprate "stripes" taken from Ref. [18].

the formation of polarons, and its connections to superconductivity and charge-density-waves (CDW). On the other hand, stretching phonon modes can be modeled using Su-Schrieffer-Heeger (SSH)-type interactions [39], in which the lattice is coupled to the kinetic energy of electrons hopping between atomic sites. Interest in these SSH models are not limited to the cuprates; iron-based and bismuthate superconductors [40–45] have also been studied using these interactions. Further, recent numerical studies [46, 47] suggest that such a coupling could lead to light bipolaron formation, creating a bipolaronic superfluid, and enhancing the superconducting T_c.

Given these recent developments, further study of *e*-ph coupling in the context of low-energy effective models is deserved. For instance, what is the influence of Holstein and SSH couplings on the Hubbard model? Knowing how these interactions affect different phases could provide a more complete description of cuprates as well as other materials. Another less explored aspect is the distinction between the different forms of the SSH model. In the *optical* model, atoms themselves are displaced [48], whereas the *bond* model describes the change of the individual bonds between atoms [49]. Understanding the behavior of these *e*-ph models relative to each other should be explored before adding further complexities such as *e*-*e* interactions. Thus, we embark on an exploration into the Hubbard model with models of electron-phonon (*e*-ph) interaction using advanced numerical methods.

1.1 Roadmap of this dissertation

This dissertation explores four related projects, each related to intertwined orders in the Hubbard and electron-phonon models. The document is organized in the following manner:

1. **Chapter 2:** Provides a detailed background on the Hubbard, Holstein, and SSH models, and explains numerical methods; namely, VMC and DQMC.

2. **Chapter 3:** Describes the effect that Holstein phonons have on stripes and uniform d-wave superconductivity in the Hubbard model by examining ground state properties using VMC and finite temperature properties with DQMC.

3. **Chapter 4:** Makes a systematic comparison of pairing correlations in the Holstein, "bond" SSH (bSSH), "optical" SSH (oSSH) models using DQMC and provides a critique on recent work regarding SSH-driven bipolaronic superconductivity.

4. **Chapter 5:** Through a finite size scaling analysis on DQMC data, this chapter maps out a ground state phase diagram of the oSSH-Hubbard model, revealing a potential coexistence region between AFM and BOW states.

Together, these works refine our understanding of how including lattice interactions in the Hubbard model affects strongly correlated behavior. Further, they expand the body of knowledge on the properties of the less-explored SSH-type models. Finally, Chapter 6 synthesizes these insights and discusses extensions for future work.

CHAPTER 2:
MODELS & METHODS

Risk...risk is our business.
That's what this starship is all about. That's why we're aboard her.

— Capt. James T. Kirk, *Star Trek*

This chapter outlines the theoretical tools used in obtaining results that will be shown in the remainder of this dissertation. First, we introduce the Hubbard model, a successful minimal model for strong correlations, followed by various models of e-ph interactions. Next, details are provided for quantum Monte Carlo methods; namely, variational and determinant quantum Monte Carlo.

2.1 The Hubbard model

In 1963, the intrepid explorers Martin Gutzwiller [50], Junjiro Kanamori [51], and John Hubbard [12], independently discovered what is now regarded as the "standard model" of electronic correlations. This model was an extension of existing tight-binding formalism, and although Hubbard was the last to publish, his subsequent work [52, 53] would refine the model that now bears his name.

Focusing on two-dimensional (2D) square lattices, we define a generic model Hamiltonian of the form $\hat{H} = \hat{H}_e + \hat{H}_{e-e}$ where

$$\hat{H}_e = \sum_{i,\nu,\sigma} t_{a_\nu} (\hat{c}^\dagger_{i,\sigma} \hat{c}_{i+a_\nu,\sigma} + \text{H.c.}) - \mu \sum_{i,\sigma} n_{i,\sigma}, \tag{2.1}$$

describes a system of non-interacting electrons. Here, $\hat{c}^\dagger_{i,\sigma}$ ($\hat{c}_{i,\sigma}$) creates (annihilates) a spin-σ ($=\uparrow,\downarrow$) electron at lattice site i, $n_{i,\sigma} = \hat{c}^\dagger_{i,\sigma}\hat{c}_{i,\sigma}$ is the number operator, and H.c. denotes the Hermitian conjugate. The index ν runs over the $\hat{x}$ and $\hat{y}$ spatial dimensions, a_ν are primitive lattice vectors, $t_{i,i+a_\nu}$ is the hopping integral between

sites i and $i + a_\nu$, and μ is the chemical potential. To obtain the *Hubbard* model, we set $t_{a_\nu} = t$, and add the interaction term

$$\hat{H}_{e-e} = U \sum_i n_{i,\uparrow} n_{i,\downarrow}, \tag{2.2}$$

where U represents the on-site Coulomb repulsion. Now often referred to as the "Hubbard U", this notation was likely popularized by Philip Anderson, as Hubbard himself used I instead. An illustration of the model is shown in Fig. 2.1a and the idea is simple: electrons are allowed to hop to neighboring sites, paying an energy cost U if electrons of opposite spin occupy the same site. This simplicity, however, is deceiving; an exact solution has only been isolated for a one-dimensional system [54]. Even with current computational power, the Hubbard model is a difficult one to solve in higher dimensions. This was all alluded to from the time of Gutzwiller's, Kanamori's, and Hubbard's independent discoveries, as all three described different physics.

2.2 Models of electron-phonon interaction

While it may be considered as the "standard model" of electronic correlations, the Hubbard model neglects details such as long-range interactions, multiple orbitals, etc. A notable example is that the model does not include lattice degrees of freedom nor does it include the interaction of the lattice with electrons. In 1933, Lev Landau introduced the notion of the "polaron" [57], a quasiparticle used in the understanding of the interaction between electrons and atoms. Herbert Fröhlich would later introduce a model for describing polaron dynamics with phonons [58], which considered free electrons interacting with a single phonon branch. Because of its derivation in the continuum, it could easily describe properties such as the dielectric constant; however, the Fröhlich model assumes that the e-ph interaction is not strong compared to the electronic bandwidth.

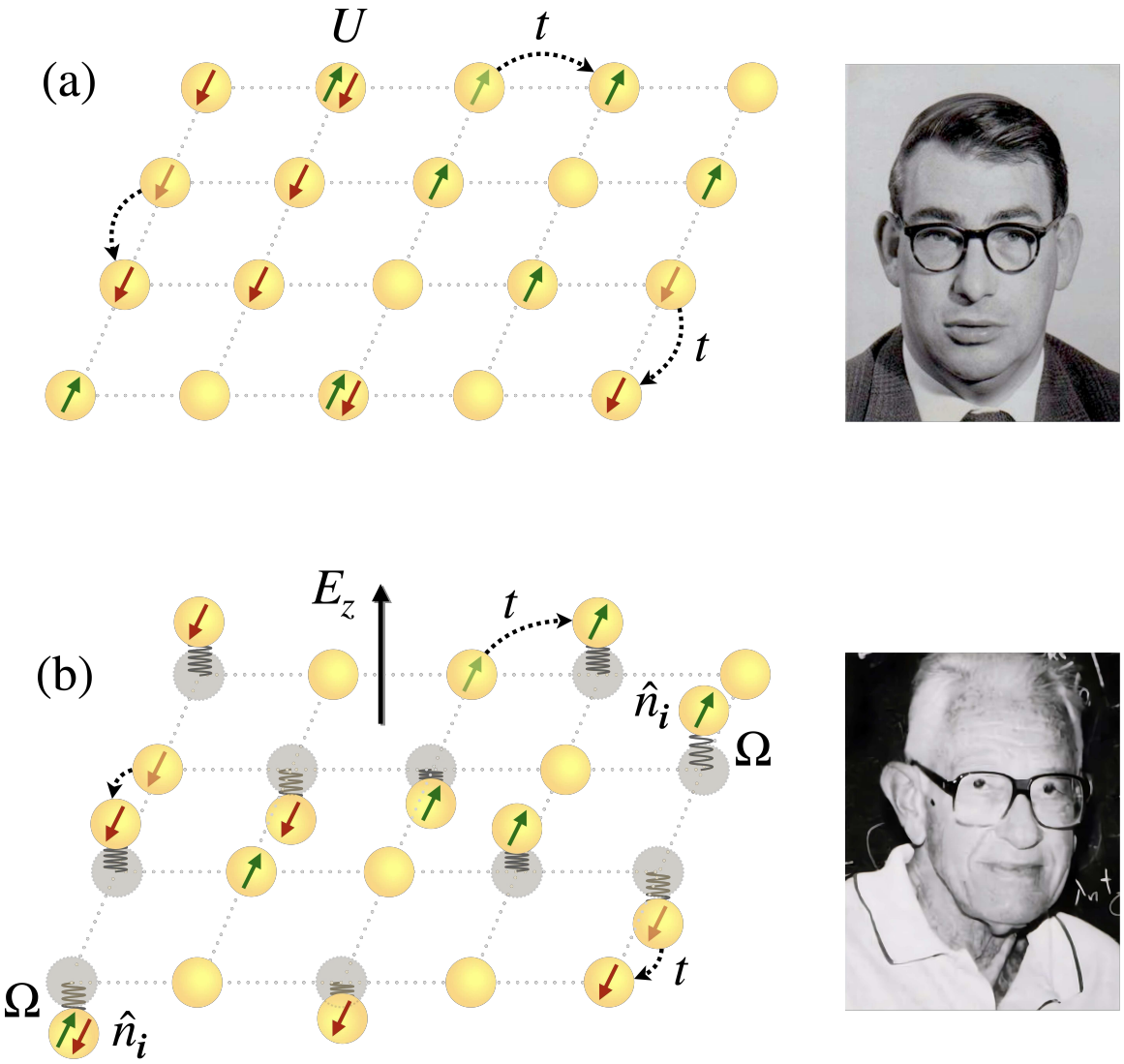

Figure 2.1: (a) Illustration of the Hubbard model in two-dimensions (2D). Spin-up (green arrows) and spin-down (red arrows) electrons hop between atoms (spheres) with amplitude t and pay an energy cost U if they occupy the same site. Photo of John Hubbard [55]. (b) Illustration of the Holstein model in 2D. On-site phonons (springs) oscillate out-of-plane with frequency Ω when subject to an electric field E_z and couple to the local electron density $\hat{n}_i$. Photo of Theodore Holstein [56].

2.2.1 The Holstein model

Theodore Holstein contributed to the body of work surrounding polaron motion in 1959 with two papers describing what we now call the *Holstein* model [35, 59]. Unlike the model of Fröhlich, this e-ph interaction is assumed to be local, with a small electronic bandwidth with the tight-binding approximation. We can once again define a generic Hamiltonian $\hat{H} = \hat{H}_e + \hat{H}_{\text{ph}} + \hat{H}_{e-\text{ph}}$, where $\hat{H}_e$ is the non-interacting electronic Hamiltonian (see Equation 2.1), and phonons are introduced as local harmonic oscillators on each site

$$\hat{H}_{\text{ph}} = \sum_i \left(\frac{1}{2M} \hat{P}_i^2 + \frac{1}{2} M\Omega^2 \hat{X}_i^2 \right) \tag{2.3}$$

$$= \Omega \sum_i \left(\hat{b}_i^\dagger \hat{b}_i + \frac{1}{2} \right), \tag{2.4}$$

where $\hat{X}_i$ ($\hat{P}_i$) is the position (momentum) operator for a dispersionless optical phonon at lattice site i with energy Ω (assuming $\hbar = 1$, going forward), and ion mass M. Equation 2.4 rewrites the model in terms of phonon creation/annihilation operators by using the transformation

$$\begin{aligned} \hat{X} &= \frac{1}{\sqrt{2M\Omega}} \left(\hat{b}_i^\dagger + \hat{b}_i \right), \\ \hat{P} &= i\sqrt{\frac{M\Omega}{2}} \left(\hat{b}_i^\dagger - \hat{b}_i \right). \end{aligned} \tag{2.5}$$

The electronic and phononic subsystems are then coupled via the term

$$\hat{H}_{e-\text{ph}}^{\text{h}} = g \sum_{i,\sigma} (\hat{n}_{i,\sigma} - \tfrac{1}{2})(b_i^\dagger + b_i) = \alpha \sum_{i,\sigma} \hat{X}_i (\hat{n}_{i,\sigma} - \tfrac{1}{2}), \tag{2.6}$$

where $g = \alpha / \sqrt{2M\Omega}$ parameterizes the strength of the e-ph coupling. An illustration of this model can be found in Fig. 2.1b.

2.2.2 The Su-Schrieffer-Heeger model

While Holstein formulated his model to study polarons, the study of a different quasiparticle, the soliton, inspired Wu-Pei Su, John Schrieffer, and Alan Heeger to formulate their model of lattice motion. Studying polyacetylene chains [39], their model studied the chain motion of the lattice. As formulated by Su, Schrieffer, and Heeger, it described acoustic phonons, meaning the phonon frequency Ω acquires momentum dependence. A later variation, the *optical*-SSH model [60], would instead have (dispersionless) optical phonons. An interesting caveat is that although it now holds their namesakes, a similar model was actually formulated nearly a decade earlier in three-dimensions by Jean-Philippe Labbé, Slaven Barišić, and Jacques Friedel [61] (so perhaps we should actually be calling it the *LBF model*).

We again define a generic Hamiltonian $\hat{H} = \hat{H}_e + \hat{H}_{\text{ph}} + \hat{H}_{e-\text{ph}}$, where $\hat{H}_e$ is the non-interacting electronic Hamiltonian (see Equation 2.1). In contrast to the Holstein model, we introduce simple harmonic oscillators along the directions of the lattice such that

$$\hat{H}_{\text{ph}} = \sum_{i,\nu} \left(\frac{1}{2M} \hat{P}_{i,\nu}^2 + \frac{1}{2} M \Omega^2 \hat{X}_{i,\nu}^2 \right), \tag{2.7}$$

where ν are the directions of the lattice and $\hat{X}_{i,\nu}$ and $\hat{P}_{i,\nu}$ are the corresponding displacement and momentum operators. Figure 2.2a summarizes how this model works in two-dimensions: on-site phonons vibrate in the x- and y-directions with frequency Ω, causing displacements between sites i and $i \pm a_\nu$, where $\nu = \{x, y\}$. These displacements affect the electronic hopping integral such that the modulated hopping amplitude is $t_{\text{eff}} = t \mp \left(\hat{X}_{i,\nu} - \hat{X}_{i \pm a_\nu} \right)$. We can express the form of the coupling using the following Hamiltonian

$$\hat{H}_{e-\text{ph}}^{\text{oSSH}} = \alpha \sum_{i,\nu,\sigma} \left(\hat{X}_{i,\nu} - \hat{X}_{i \pm a_\nu} \right) \left(\hat{c}_{i,\sigma}^\dagger \hat{c}_{i+a_\nu,\sigma} + \text{H.c.} \right). \tag{2.8}$$

A further simplification can be made to this model by considering the placement of phonons. In the *bond* SSH model [62], the oscillators are located on the *bonds*, and are understood to describe the change in the relative distances between the atom at site i and $i \pm a_\nu$. This is demonstrated in Figure 2.2b and the form of the coupling can be expressed in the Hamiltonian

$$\hat{H}_{e-\mathrm{ph}}^{\mathrm{bSSH}} = \alpha \sum_{i,\nu,\sigma} \hat{X}_{i,\nu} \left(\hat{c}_{i,\sigma}^{\dagger} \hat{c}_{i+a_\nu,\sigma} + \mathrm{H.c.} \right). \tag{2.9}$$

It is noteworthy that how this model is written means that the kinetic energy modulation occurs along one bond at a time.

2.2.3 The dimensionless electron-phonon coupling constant

The microscopic coupling constant α (and g) is often referred to as the "dimensionful" e-ph constant; however, we can define a "dimensionless" constant to better characterize the strength of the coupling relative to the electronic kinetic energy. This definition can be traced back to the coupling in BCS theory. The dimensionless coupling for a momentum-dependent e-ph interaction $g_\nu(\mathbf{k}, \mathbf{q})$ is defined [63] as

$$\lambda = 2\mathcal{N}(0) \sum_{\nu} \left\langle\!\!\left\langle \frac{|g_\nu(k,q)|^2}{\Omega_{\nu,q}} \right\rangle\!\!\right\rangle_{\mathrm{FS}}, \tag{2.10}$$

where ν is a mode index, $\xi_k = \epsilon_k - \mu$ with $\epsilon_k = -2t \sum_\nu \cos(k_\nu a)$ is the non-interacting electron dispersion measured relative to the chemical potential, $\mathcal{N}(0) = \frac{1}{N} \sum_k \delta(\xi_k)$ is the density of states at the Fermi level per spin species, and $\langle\!\langle \cdot \rangle\!\rangle_{\mathrm{FS}}$ denotes a Fermi surface (FS) average

$$\left\langle\!\!\left\langle \frac{|g_\nu(k,q)|^2}{\Omega_{\nu,q}} \right\rangle\!\!\right\rangle_{\mathrm{FS}} = \frac{\frac{1}{N^2} \sum_{k,q} \frac{|g_\nu(k,q)|^2}{\Omega_{\nu,q}} \delta(\xi(k+q)) \delta(\xi(k))}{\frac{1}{N^2} \sum_{k,q} \delta(\xi(k+q)) \delta(\xi(k))}. \tag{2.11}$$

Thus, the full expression for λ is

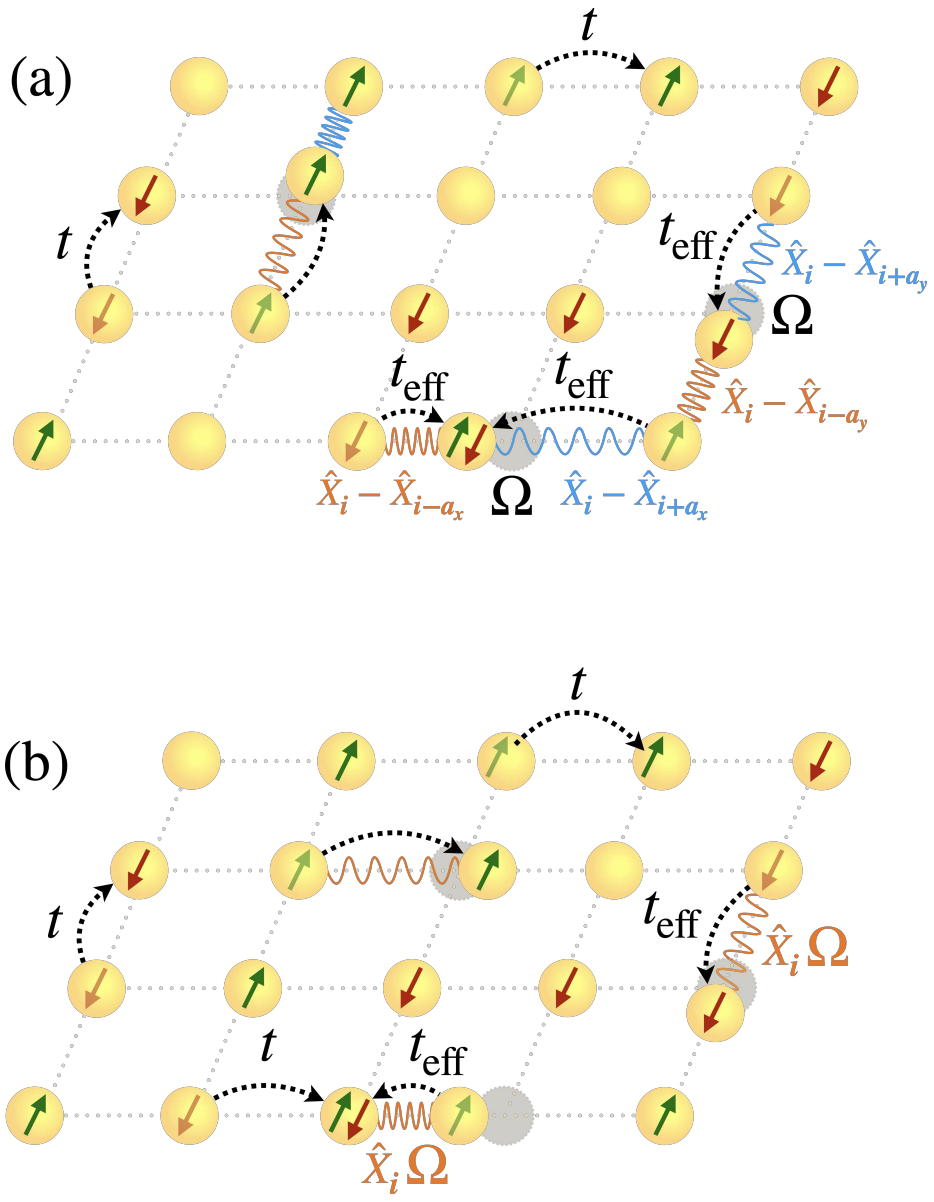

Figure 2.2: (a) Illustration of the *optical* SSH model in 2D. On-site phonons with frequency Ω and displacements $\hat{X}_i - \hat{X}_{i\pm a_\nu}$ ($\nu = \{x, y\}$), modulate the hopping of electrons with amplitude t_{eff}. (b) Illustration of the *bond* Su-Schrieffer-Heeger (SSH) model in two-dimensions (2D). A spin-up (green arrow) or spin-down (red arrow) hopping between atoms with amplitude t_{eff} absorbs/emits a bond phonon (orange springs) with frequency Ω and displacement $\hat{X}_i$. The unmodulated hopping integral has amplitude t.

$$\lambda = \frac{2}{\mathcal{N}(0)N^2} \sum_{k,q,\nu} \frac{|g_\nu(k,q)|^2}{\Omega_{\nu,q}} \delta(\xi(k+q))\delta(\xi(k)). \tag{2.12}$$

In the 2D Holstein model, the electrons couple to a single dispersionless phonon branch $\Omega_q = \Omega$ via a momentum-independent e-ph coupling $g_\mathrm{h} = \alpha_\mathrm{h}/\sqrt{2M_\mathrm{h}\Omega}$. In this case, the dimensionless coupling reduces to $\lambda_\mathrm{h} = \frac{\alpha_\mathrm{h}^2}{M_\mathrm{h}\Omega^2 W}$, where we have approximated $\mathcal{N}(0) \approx W^{-1}$, where $W = 8t$ the non-interacting bandwidth.

In the 2D optical and bond SSH models, the electrons couple to two dispersionless optical phonon branches $\nu = x, y$ with $\Omega_{x,q} = \Omega_{y,q} = \Omega$ via momentum-dependent e-ph coupling constants [64, 65]

$$\begin{aligned} g_\nu^\mathrm{o}(\mathbf{k},\mathbf{q}) &= 4\frac{\alpha_\mathrm{o}}{\sqrt{2M_\mathrm{o}\Omega}} \mathrm{i}\sin\left(\tfrac{q_\nu a}{2}\right)\cos((k_\nu + q_\nu/2)a), \\ g_\nu^\mathrm{b}(\mathbf{k},\mathbf{q}) &= 2\frac{\alpha_\mathrm{b}}{\sqrt{2M_\mathrm{b}\Omega}} e^{\mathrm{i}q_\nu a/2}\cos((k_\nu + q_\nu/2)a). \end{aligned} \tag{2.13}$$

for the optical and bond SSH models, respectively. The dimensionless coupling is obtained by performing the FS average as defined in Eq. 2.10. However, due to the finite size of clusters in lattice methods, performing accurate FS averages is prone to finite size effects, particularly away from half-filling. Therefore, we approximate Eq. 2.10 by replacing the FS average with a simple average over the first Brillouin zone. The corresponding dimensionless e-ph couplings are $\lambda_\mathrm{b} = \frac{4\alpha_\mathrm{b}^2}{M_\mathrm{b}\Omega^2 W}$ and $\lambda_\mathrm{o} = \frac{8\alpha_\mathrm{o}^2}{M_\mathrm{o}\Omega^2 W}$ for the bond- and optical-SSH models, respectively. For a more thorough discussion, see Ref. [66].

2.3 Monte Carlo methods

An important application of the Monte Carlo method is to compute multi-dimensional integrals which cannot be done analytically due to factors such as the large number of degrees of freedom associated with a physical process. Monte Carlo integration can be achieved by stochastically sampling a configuration space related to the

degrees of freedom of a system. We present two different quantum Monte Carlo methods for investigating different parameter regimes: zero temperature VMC, and finite temperature DQMC. The following sections detail the intricacies of each method.

2.3.1 Variational Monte Carlo

The VMC method uses Markov chains to stochastically sample particle configurations, whether they be Fermionic or Bosonic. Such configurations are then used in the optimization of parameters contained in a trial wavefunction. This method primarily relies on the variational principle, which states that the expectation value of the Hamiltonian $\hat{H}$ with any trial wavefunction $|\Psi_T\rangle$ will yield an upper bound on the exact ground state energy E_{GS}

$$E_{var} = \frac{\langle \Psi_T | \hat{H} | \Psi_T \rangle}{\langle \Psi_T | \Psi_T \rangle} \geq E_{GS}. \tag{2.14}$$

The VMC algorithm implements this such that optimizing the variational parameters minimizes the variational energy. Being a zero temperature method, this approach provides insight on ground state properties of a system. An advantage of VMC is its applicability to a wide range of toy models, irrespective of range of interaction and dimension of the local Hilbert space. This sets it apart from other ground state methods such as density matrix renormalization group (DMRG) method and exact diagonalization (ED). In the case of DMRG, complexity of the calculation increases with range of interactions and the size of the local Hilbert space [67, 68]. Despite advanced algorithms such as Lanczos, ED suffers from computer memory limitations; hence, such a method is limited to small system sizes.

Consider a configuration of electrons on a lattice $|x\rangle$ in which there are electrons with defined positions and spins quantized along the z-axis. The set of all possible

electron configurations form a basis for the many-particle Hilbert space. Recall that any wavefunction, $|\Psi\rangle$, can be expanded in this basis,

$$|\Psi\rangle = \sum_x |x\rangle \langle x|\Psi\rangle , \tag{2.15}$$

recalling that $\mathbb{1} = \sum_x |x\rangle \langle x|$. The expectation value for any quantum mechanical operator $\hat{O}$ is given by

$$\langle \hat{O} \rangle = \frac{\langle \Psi | \hat{O} | \Psi \rangle}{\langle \Psi | \Psi \rangle} = \frac{\sum_x \langle x|\Psi\rangle \langle x| \hat{O} |\Psi\rangle}{\sum_x \langle \Psi|x\rangle \langle x|\Psi\rangle} = \frac{\sum_x \frac{\langle x|\hat{O}|\Psi\rangle}{\langle x|\Psi\rangle} \langle \Psi|x\rangle \langle x|\Psi\rangle}{\sum_x \langle \Psi|x\rangle \langle x|\Psi\rangle} = \sum_x \hat{O}_x w_x, \tag{2.16}$$

where $w_x = \frac{|\langle x|\Psi\rangle|^2}{\sum_x |\langle x|\Psi\rangle|^2}$ is the weight of $|x\rangle$, and

$$\hat{O}_x = \frac{\langle x| \hat{O} |\Psi\rangle}{\langle x|\Psi\rangle} \tag{2.17}$$

is known as the local estimator [69] of the observable $\hat{O}$ for some configuration $|x\rangle$. In practice, these quantities are quite difficult to evaluate as the number of distinguishable configurations scales as $O(e^N)$, where N is the system size [70]. Since it is unfeasible to evaluate for all possible configurations, we must use importance sampling. In practice, this involves generating electronic configurations according to the probability distribution $p \propto |\langle x|\Psi\rangle|^2$; this is achieved by generating electronic configurations that have sufficient overlap with the wavefunction. The Markov process that is used to find such configurations is a combination of the Metropolis(-Hastings) algorithm [71] with local updates. An example procedure for performing local updates to Fermions is shown in Algorithm 1. A random particle β with spin σ in the configuration is randomly selected and a move is proposed to a random neighboring site k. Provided that site k does not have a particle β' such that $\sigma' = \sigma$ (assuming Fermions), the ratio of distributions between the proposed configuration $|x'\rangle$ and the starting configuration $a(x) = \frac{p(x')}{p(x)}$ is calculated. If this

ratio is larger than a randomly generated number m, then the move is accepted; otherwise, it is rejected.

A vital step for VMC is energy minimization through parameter optimization, which we achieve using a method known as Stochastic Reconfiguration (SR). Pioneered by the group of Sandro Sorella [72, 73], this method originally referred to mitigation of the sign problem in Green's function Monte Carlo via the fixed node approximation. This method allows for the optimization of large sets of variational parameters in a correlated manner while ensuring ergodicty and efficiency. An overview of the SR procedure can be seen in Algorithm 2.

We begin with a trial wavefunction $|\Psi_{\mathrm{T}}(\alpha)\rangle$ that depends on a set of p variational parameters $\alpha = \{\alpha_k\}$. To minimize the energy, we need to be able to compute the energy derivative with respect to α_k,

$$-\frac{\partial E_\alpha}{\partial \alpha_k} = -\frac{\partial}{\partial \alpha_k}\frac{\langle \Psi_{\mathrm{T}}(\alpha)|\,\hat{H}\,|\Psi_{\mathrm{T}}(\alpha)\rangle}{\langle \Psi_{\mathrm{T}}(\alpha)|\Psi_{\mathrm{T}}(\alpha)\rangle}. \tag{2.18}$$

To compute these derivatives in practice, it is convenient to expand $|\Psi_{\mathrm{T}}(\alpha)\rangle$ for small changes $\alpha_k \to \alpha_k + \delta\alpha_k$. Thus, to linear order

$$\begin{aligned}
|\Psi_{\mathrm{T}}(\alpha')\rangle &\simeq \delta\alpha_0\,|\Psi_{\mathrm{T}}(\alpha)\rangle + \sum_{k=1}^{p}\delta\alpha_k\frac{\partial}{\partial\alpha_k}\,|\Psi_{\mathrm{T}}(\alpha)\rangle \qquad (2.19)\\
&= \delta\alpha_0\,|\Psi_{\mathrm{T}}(\alpha)\rangle + \sum_{k=1}^{p}\delta\alpha_k\frac{\partial}{\partial\alpha_k}\sum_x |x\rangle\langle x\,|\Psi_{\mathrm{T}}(\alpha)\rangle\\
&= \delta\alpha_0\,|\Psi_{\mathrm{T}}(\alpha)\rangle + \sum_{k=1}^{p}\delta\alpha_k\sum_x\frac{\partial\,\langle x|\Psi_{\mathrm{T}}(\alpha)\rangle}{\partial\alpha_k}\,|x\rangle\\
&= \delta\alpha_0\,|\Psi_{\mathrm{T}}(\alpha)\rangle + \sum_{k=1}^{p}\delta\alpha_k\sum_x\frac{\partial\ln\langle x|\Psi_{\mathrm{T}}(\alpha)\rangle}{\partial\alpha_k}\,|x\rangle\langle x\,|\Psi_{\mathrm{T}}(\alpha)\rangle\\
&= \sum_{k=1}^{p}\delta\alpha_k\hat{\Delta}_{\Psi,k}\,|\Psi_{\mathrm{T}}(\alpha)\rangle\,, \qquad (2.20)
\end{aligned}$$

Algorithm 1 Local updates to Fermions with the Metropolis algorithm

Select a random Fermion (β, σ) and propose move to random neighboring site k.
if $(\beta', \sigma' \neq \sigma)$ is at site k **then**
    Calculate acceptance ratio $a(x) = \frac{p(x')}{p(x)}$.
    Generate random number $r \in [0, 1]$.
    if $a(x) \geq r$ **then**
        Accept move.
    else if $a(x) < r$ **then**
        Reject move.
    end if
else if $(\beta', \sigma' = \sigma)$ is at site k **then**
    Reject move.
end if

Algorithm 2 Stochastic Reconfiguration

Get current set of variational parameters $\{\alpha_k\}$.
Apply logarithmic derivative operator Δ_k.
Construct covariance matrix S and forces f.
Update parameters $\alpha_k \rightarrow \alpha_k + \eta \sum_i S_{ki}^{-1} f_i$.

where

$$\hat{\Delta}_{\Psi,k} = \begin{cases} \mathbb{I}, & k = 0 \\ \sum_x \frac{\partial \ln\langle x|\Psi_{\mathrm{T}}(\alpha)\rangle}{\partial \alpha_k} |x\rangle\langle x|, & k \neq 0 \end{cases}, \tag{2.21}$$

is the logarithmic derivative operator. To reduce the energy of the trial state, we use the power method, which repeatedly applies the operator $(\Lambda - \hat{H})$, where Λ is a diagonal operator with $\Lambda_{ii} = \lambda \in \mathbb{R}$. Thus, by expanding $|\Psi_{\mathrm{T}}\rangle$ in terms of eigenstates $|n\rangle$ of the Hamiltonian

$$|\Psi_{\mathrm{T}}(\alpha)\rangle = \sum_{n=0}^{\infty} \langle n|\Psi_{\mathrm{T}}(\alpha)\rangle |n\rangle \tag{2.22a}$$

$$\begin{aligned} \left(\Lambda - \hat{H}\right)^M |\Psi_{\mathrm{T}}(\alpha)\rangle &= \sum_{n=0}^{\infty} (\Lambda - E_n)^M \langle n|\Psi_{\mathrm{T}}(\alpha)\rangle |n\rangle \\ &= \langle n|\Psi_{\mathrm{T}}(\alpha_0)\rangle |n\rangle + \sum_{n=1}^{\infty} \left(\frac{\Lambda - E_n}{\Lambda - E_0}\right)^M \langle n|\Psi_{\mathrm{T}}(\alpha)\rangle |n\rangle, \end{aligned} \tag{2.22b}$$

where the elements of Λ are chosen such that $\lambda > (E_{\max} - E_0)/2$ and $E_{\max}$ is the maximum eigenvalue of $\hat{H}$. The consequence of this choice is that the ground state component of the expansion dominates as $M \to \infty$ up to some normalization factor and the trial state converges to the ground state as $O(e^M)$.

Returning to the first line of Eq. (2.22b), we impose the condition that the energy after projecting must be lower than the one before it by setting

$$\left(\Lambda - \hat{H}\right)|\Psi_{\mathrm{T}}(\alpha)\rangle = \sum_{k=1}^{p} \delta\alpha_k \hat{\Delta}_{\Psi,k} |\Psi_{\mathrm{T}}(\alpha)\rangle. \tag{2.23}$$

Projecting on both sides with the state $\hat{\Delta}^{\dagger}_{\Psi,k}|\Psi_{\mathrm{T}}(\alpha)\rangle$, we get

$$\begin{aligned} \sum_{k=1}^{p} \delta\alpha_k \langle \Psi_{\mathrm{T}}(\alpha)|\hat{\Delta}_{\Psi,k'}\hat{\Delta}_{\Psi,k}|\Psi_{\mathrm{T}}(\alpha)\rangle &= \langle \Psi_{\mathrm{T}}(\alpha)|\hat{\Delta}_{\Psi,k'}\left(\Lambda - \hat{H}\right)|\Psi_{\mathrm{T}}(\alpha)\rangle \\ \sum_{k=1}^{p} \delta\alpha_k \left\langle \hat{\Delta}_{\Psi,k'}\hat{\Delta}_{\Psi,k}\right\rangle &= \Lambda \left\langle \hat{\Delta}_{\Psi,k'}\right\rangle - \left\langle \hat{\Delta}_{\Psi,k'}\hat{H}\right\rangle, \end{aligned} \tag{2.24}$$

where in the last equation, we divided both sides by $\langle \Psi_T(\alpha) | \Psi_T(\alpha) \rangle$ to obtain expectation values. If $k' = 0$, then

$$\delta\alpha_0 + \sum_{k=1}^{p} \delta\alpha_k \left\langle \hat{\Delta}_{\Psi,k} \right\rangle = \Lambda - \left\langle \hat{H} \right\rangle, \tag{2.25}$$

and if $k' \neq 0$, we get

$$\delta\alpha_0 \left\langle \hat{\Delta}_{\Psi k'} \hat{\Delta}_{\Psi,k} \right\rangle + \sum_{k=1}^{p} \delta\alpha_k \left\langle \hat{\Delta}_{\Psi,k'} \hat{\Delta}_{\Psi,k} \right\rangle = \Lambda \left\langle \hat{\Delta}_{\Psi,k'} \right\rangle - \left\langle \hat{\Delta}_{\Psi,k'} \hat{H} \right\rangle. \tag{2.26}$$

We can solve the $k = 0$ equation for $\delta\alpha_0$ and perform a substitution

$$\left(\Lambda - \left\langle \hat{H} \right\rangle - \sum_{k=1}^{p} \delta\alpha_k \left\langle \hat{\Delta}_{\Psi k} \right\rangle \right) \left\langle \hat{\Delta}_{\Psi,k'} \hat{\Delta}_{\Psi k} \right\rangle + \sum_{k=1}^{p} \delta\alpha_k \left\langle \hat{\Delta}_{\Psi k'} \hat{\Delta}_{\Psi,k} \right\rangle = \Lambda \left\langle \hat{\Delta}_{\Psi,k'} \right\rangle - \left\langle \hat{\Delta}_{\Psi,k'} \hat{H} \right\rangle \tag{2.27}$$

which, after some re-arranging, we get

$$\begin{aligned} &\Lambda \left\langle \hat{\Delta}_{\Psi k'} \hat{\Delta}_{\Psi k} \right\rangle - \left\langle \hat{H} \right\rangle \left\langle \hat{\Delta}_{\Psi k'} \hat{\Delta}_{\Psi k} \right\rangle - \sum_{k=1}^{p} \delta\alpha_k \left\langle \hat{\Delta}_{\Psi k} \right\rangle \left\langle \hat{\Delta}_{\Psi k'} \hat{\Delta}_{\Psi k} \right\rangle \\ &\quad + \sum_{k=1}^{p} \delta\alpha_k \left\langle \hat{\Delta}_{\Psi k'} \hat{\Delta}_{\Psi k} \right\rangle = \Lambda \left\langle \hat{\Delta}_{\Psi k'} \right\rangle - \left\langle \hat{\Delta}_{\Psi k'} \hat{H} \right\rangle \\ \implies &\sum_{k=1}^{p} \delta\alpha_k \left(\left\langle \hat{\Delta}_{\Psi k'} \hat{\Delta}_{\Psi k} \right\rangle - \left\langle \hat{\Delta}_{\Psi k'} \right\rangle \left\langle \hat{\Delta}_{\Psi k} \right\rangle \right) = \left\langle \hat{\Delta}_{\Psi k'} \right\rangle \hat{H} - \left\langle \hat{\Delta}_{\Psi k} \hat{H} \right\rangle. \end{aligned} \tag{2.28}$$

We can tidy these equations by setting some of the terms to the following

$$\begin{aligned} \mathbf{S}_{k,k'} &= \left\langle \hat{\Delta}_{\Psi,k'} \hat{\Delta}_{\Psi,k} \right\rangle - \left\langle \hat{\Delta}_{\Psi,k'} \right\rangle \left\langle \hat{\Delta}_{\Psi,k} \right\rangle \\ f_{k'} &= \left\langle \hat{\Delta}_{\Psi,k'} \right\rangle \left\langle \hat{H} \right\rangle - \left\langle \hat{\Delta}_{\Psi,k} \hat{H} \right\rangle, \end{aligned} \tag{2.29}$$

where $\mathbf{S}_{kk'}$ is a covariance matrix and $f_{k'}$ is a generalized force proportional to the derivative of the energy. Thus, we obtain the following differential equation

$$f_{k'} = \sum_{k=1}^{p} \delta\alpha_k \mathbf{S}_{kk'}, \tag{2.30}$$

which can be used to define a steepest descent method for updating variational parameters

$$\alpha_k \rightarrow \alpha_k + \eta \sum_i \mathbf{S}^{-1}_{ki} f_i, \tag{2.31}$$

where η is chosen to ensure rapid convergence. The inclusion of the covariance matrix inverse allows for updates to all α to be performed in a correlated manner, unlike typical steepest descent methods.

Compiling all of these ingredients together, the general structure of a VMC simulation can be seen in Algorithm 3. With an initial set of variational parameters and a random configuration of electrons x, we construct the variational wavefunction at the start of each bin. Then iterating over the bin length n_{bin}, we equilibrate the systems before making measurements. After accumulation, the parameters are then updated using SR.

2.3.2 Trial wavefunctions for VMC

The success or failure of VMC depends on the trial wavefunction. Such an object is constructed considering the symmetries of the lattice Hamiltonian and how close the ground state energy is captured depends on how accurately the state is parameterized. Another aspect of this parameterization is that different trial wavefunctions may yield identical energies. Thus, it is not necessarily possible to conclude which is the true ground state. Recent improvements in techniques for constructing wavefunctions has mitigated this difficulty.

Algorithm 3 Overview of the VMC simulation structure

Initialize variational parameters
Initialize random particle configuration x.
for bin $\in [1, N_{\text{bins}}]$ **do**
    Construct variational wavefunction using particle configuration x.
    for $i \in [1, n_{\text{bin}}]$ **do**
        for $j \in [1, N_{\text{equil.}}]$ **do**
            Update particle configuration x using Algorithm 1.
            Update equal-time Green's function W.
            Update Jastrow vectors(s) T.
        end for
        Make measurements.
    end for
    Update variational parameters using Algorithm 2.
    Write average value of measurements in current bin to file.
end for
Average binned measurement to get final estimates for observables.

A standard choice of ansatz for variational calculations involving Fermions are the *Jastrow-Slater* trial states of the form

$$|\Psi_{\mathrm{T}}(\alpha)\rangle = \mathcal{J}^{e-e}\,\mathcal{P}(N_e)\,|\Phi(\alpha)\rangle\,, \tag{2.32}$$

where $\mathcal{P}(N_e)$ is the projector that fixes the number of electrons in the canonical ensemble, $\mathcal{J}^{e-e}$ is the electron-electron Jastrow correlation factor, and $|\Phi(\alpha)\rangle$ is the *Slater determinant state*

$$|\Phi(\alpha)\rangle = \exp\left[\sum_{i,j} f_{ij}(\alpha_k)\hat{c}^{\dagger}_{i,\uparrow}\hat{c}^{\dagger}_{j,\downarrow}\right]|0\rangle\,, \tag{2.33}$$

where $f_{ij}(\alpha_k)$ is the pairing function for variational parameter α_k. These pairing functions make up the auxiliary/mean-field Hamiltonian that is diagonalized to obtain the electronic trial state. If we consider the Hubbard model from Sec. 2.1, we can construct an appropriate auxiliary Hamiltonian $\hat{H}_{\mathrm{aux}}(\alpha)$ by considering the expected symmetries from the Hubbard Hamiltonian. Starting with the non-interacting tight-binding model (Eq. 2.1), we can add terms that model various phenomena induced by electronic correlations. For instance, we can consider (Néel) antiferromagnetism

$$\hat{H}_z^{\mathrm{mag}} = \Delta_z \sum_i (-1)^{i_x+i_y}\left(\hat{c}^{\dagger}_{i,\uparrow}\hat{c}_{i,\uparrow} - \hat{c}^{\dagger}_{i,\downarrow}\hat{c}_{i,\downarrow}\right), \tag{2.34}$$

d-wave pairing

$$\hat{H}_d^{\mathrm{pair}} = \sum_{\langle i,j\rangle} \Delta_d\left[\delta_{i+\hat{x},j} + \delta_{i-\hat{x},j} - \delta_{i+\hat{y},j} - \delta_{i-\hat{y},j}\right]\left(\hat{c}^{\dagger}_{i,\uparrow}\hat{c}^{\dagger}_{j,\downarrow} + \hat{c}^{\dagger}_{j,\uparrow}\hat{c}^{\dagger}_{i,\downarrow} + \mathrm{H.c.}\right), \tag{2.35}$$

and site-dependent spin and charge (stripes) order

$$\begin{aligned}\hat{H}^{\text{mag}}_{\text{stripe}} &= \sum_i \Delta^s_{i_x} (-1)^{i_x+i_y} \left(\hat{c}^\dagger_{i,\uparrow}\hat{c}_{i,\uparrow} - \hat{c}^\dagger_{i,\downarrow}\hat{c}_{i,\downarrow}\right) \\ \hat{H}^{\text{charge}}_{\text{stripe}} &= \sum_i \Delta^c_{i_x} \left(\hat{c}^\dagger_{i,\uparrow}\hat{c}_{i,\uparrow} + \hat{c}^\dagger_{i,\downarrow}\hat{c}_{i,\downarrow}\right),\end{aligned} \tag{2.36}$$

where Δ_z, Δ_d, $\Delta^s_{i_x}$, and $\Delta^c_{i_x}$ are all variational parameters that can be optimized using SR. Note that all of these Hamiltonians are quadratic in the operators which makes them simple to diagonalize to obtain the trial state. However, the pairing Hamiltonian in its present form cannot be straightforwardly diagonalized as it contains paired creation/annihilation operators. This necessitates the use of a (partial) particle-hole transformation

$$\begin{cases}\hat{c}^\dagger_{i,\uparrow} \to \hat{c}^\dagger_{i,\uparrow} \\ \hat{c}^\dagger_{i,\downarrow} \to \hat{c}_{i,\downarrow} \quad ,\end{cases} \tag{2.37}$$

which transforms particle in the spin-down sector. Note that this transformation would apply to all terms in the auxiliary Hamiltonian.

If phononic degrees of freedom are added to the model, then our ansatz should also include phononic correlations. For instance, consider the case of constructing a trial state for the *Hubbard-Holstein model*. The Jastrow-Slater state now has the form

$$|\Psi_{\text{T}}(\alpha)\rangle = \mathcal{J}^{e-e}\mathcal{J}^{e-\text{ph}}\mathcal{D}(N_e)\,|\Phi(\alpha)\rangle \otimes \left|\Phi^{\text{ph}}\right\rangle, \tag{2.38}$$

where $\mathcal{J}^{e-e}$, $\mathcal{D}(N_e)$, and $|\Phi(\alpha)\rangle$ are the same electronic quantities from Equations 2.32 and 2.33. The new additions are the electron-phonon Jastrow factor $\mathcal{J}^{e-\text{ph}}$ and the phononic state

$$\left|\Phi^{\text{ph}}\right\rangle = \sum_{N_{\text{ph}}} \exp\left(\mu_{\text{ph}} \sum_i n^{\text{ph}}_i\right) \frac{\left(\hat{b}^\dagger_{k=0}\right)^{N_{\text{ph}}}}{N_{\text{ph}}!}\,|0\rangle_{\text{ph}} \tag{2.39}$$

where μ_{ph} is the phonon fugacity, n_i^{ph} is the number of phonons at site i, N_{ph} is the total number of phonons, and

$$\hat{b}_{k=0}^{\dagger} = \frac{1}{\sqrt{N}} \sum_i \hat{b}_i^{\dagger}, \tag{2.40}$$

creates a phonon in the momentum state $k = 0$ for N lattice sites. Note the phonon fugacity is an additional variational parameter that is optimized by SR.

The role of the *Jastrow factors* in Equations 2.32 and 2.38 is to (re-) introduce correlations beyond the level of Pauli exclusion and Fermion exchange. This is because there are no further correlations beyond these in the mean-field solution. The type of correlations that can be added vary; for example, we have the density-density Jastrow factor

$$\mathcal{J}_d^{e-e} = \exp\left(-\frac{1}{2}\sum_{i,j} v_{ij} n_i n_j\right), \tag{2.41}$$

where v_{ij} are pseudo-potentials that depend on the distance between sites i and j $\left[v_{ij} = v\left(r_{ij}\right)\right]$. These pseudo-potentials are parameters that can also be optimized. Applying this to the Slater determinant creates a sum of Slater determinants which have their double occupancies projected out. Other forms of the Jastrow factor exist for spin correlations

$$\mathcal{J}_s^{e-e} = \exp\left(-\frac{1}{2}\sum_{ij} v_{ij} S_i S_j\right), \tag{2.42}$$

and even between electron and phonon densities

$$\mathcal{J}^{e-\text{ph}} = \exp\left(-\sum_{ij} w_{ij} n_i^e n_j^{\text{ph}}\right). \tag{2.43}$$

The importance of the Jastrow factor lies in capturing essential Hubbard model physics, such as the correct Mott insulator for a finite Hubbard U [74, 75]. Further,

the e-ph Jastrow factor has demonstrated itself to be essential in capturing the correct ground state charge fluctuations found for microscopic e-ph coupling α [76].

2.3.3 Determinant Quantum Monte Carlo

The DQMC method computes Green's functions by stochastically sampling auxiliary fields. After splitting a Hamiltonian into its non-interacting and interacting parts, a Hubbard-Stratonovich transformation is performed to introduce an auxiliary field on each lattice site, and recast the interacting terms into being quadratic in operators. Thus, an interacting problem is made into a non-interacting one. This method can be used to compute a number of different observables and correlations functions, and is numerically exact barring controllable discretization errors and the presence of the Fermion sign problem. DQMC is advantageous over perturbative methods as it treats interactions exactly.

Suppose we have a Hamiltonian matrix of the form $H = K + V$ where K is the non-interacting part and V is an interacting part. The primary goal is to evaluate the partition function, which can be expressed as a thermodynamic trace $Z = \mathrm{Tr} e^{-\beta H}$. By dividing the inverse temperature interval $[0, \beta]$ into small imaginary time slices $\Delta\tau = \beta / L_\tau$ (for number of time slices L), one can rewrite the partition function in the following manner

$$Z = \mathrm{Tr} e^{-\beta H} = \mathrm{Tr} e^{-\Delta\tau L_\tau H} = \mathrm{Tr}\left[e^{-\Delta\tau V_{l,\sigma}} e^{-\Delta\tau K_{l,\sigma}}\right]^{L_\tau} + O(\Delta\tau^2) \tag{2.44}$$

$$\approx \mathrm{Tr} \prod_l \left[e^{-\Delta\tau V_{l,\sigma}} e^{-\Delta\tau K_{l,\sigma}}\right], \tag{2.45}$$

where $V_{l,\sigma}$ and $K_{l,\sigma}$ are the potential and kinetic energy matrices, respectively, for a spin-σ electron at imaginary time slice l. The last step of Eq. (2.45) is obtained via application of the Trotter approximation [77–79].

For further illustration, we will consider the case of the (single-band) Hubbard model, which has interaction term $V = U\sum_i n_{i,\uparrow}n_{i,\downarrow}$. This term can be made quadratic by the introduction of an auxiliary field $\phi_{i,l} = \pm 1$ on each site and at each time slice [80]. Through the Hubbard-Stratonovich (HS) transformation, we obtain

$$e^{\alpha n_{i,\uparrow}n_{i,\downarrow}} = \begin{cases} \frac{1}{2}e^{\alpha(n_{i,\uparrow}+n_{i,\downarrow})/2}\sum_{\phi_{i,l}=\pm 1} e^{-\lambda\phi_{i,l}(n_{i,\uparrow}-n_{i,\downarrow})} & (\alpha > 0) \\ \frac{1}{2}e^{\alpha(n_{i,\uparrow}+n_{i,\downarrow})/2}\sum_{\phi_{i,l}=\pm 1} e^{-\lambda\phi_{i,l}(n_{i,\uparrow}-n_{i,\downarrow}-1)+\frac{\alpha}{2}} & (\alpha < 0) \end{cases}, \tag{2.46}$$

where $\lambda = \ln\left(e^{|\alpha|/2} + \sqrt{|\alpha|-1}\right)$ and $\alpha = \Delta\tau U > 0$. Returning to the partition function

$$\begin{aligned} Z &= \mathrm{Tr}\prod_l \left[e^{-\Delta\tau V_{l,\sigma}}e^{-\Delta\tau K_{l,\sigma}}\right] \\ &= \mathrm{Tr}\prod_l \left\{\left[\prod_i \frac{1}{2}e^{\alpha(n_{i,\uparrow}+n_{i,\downarrow})/2}\sum_{\phi_{i,l}=\pm 1} e^{-\lambda\phi_{i,l}(n_{i,\uparrow}-n_{i,\downarrow})}\right]e^{-\Delta\tau K_{l,\sigma}}\right\}. \end{aligned} \tag{2.47}$$

We can simplify by absorbing the term $e^{\alpha(n_{i,\uparrow}+n_{i,\downarrow})/2}$ into the chemical potential via a transformation $\mu \to \mu + U/2$ such that $K'_{l,\sigma} = K_{l,\sigma} + \sum_i \frac{U}{2}(n_{i\uparrow} + n_{i,\downarrow})$. If we identify the following (propagator) matrices

$$B_{l,\sigma} = e^{\mp\sum_i \lambda\phi_{i,l}n_{i,\sigma}}e^{-\Delta\tau K'_{l,\sigma}}, \tag{2.48}$$

they allow us to rewrite the partition function in the following form

$\mathrm{B}_{l,\downarrow} = \sum_{\phi_{i,l}=\pm 1} \mathrm{Tr}\left(B_{L_\tau,\uparrow}B_{L_\tau-1,\uparrow}\ldots B_{1,\uparrow}\right)\mathrm{Tr}\left(B_{L_\tau,\downarrow}B_{L_\tau-1,\downarrow}\ldots B_{1,\downarrow}\right).$

Now, in order to compute the partition function, we need to use the following property of the trace

$$\mathrm{Tr}\left(e^{\hat{c}^\dagger T_1\hat{c}}e^{\hat{c}^\dagger T_2\hat{c}}\ldots e^{\hat{c}^\dagger T_n\hat{c}}\right) = \det\left(\mathbb{I} + e^{T_1}e^{T_2}\ldots e^{T_n}\right), \tag{2.49}$$

where $\mathbb{I}$ is and $N \times N$ identity matrix (for system size N) and $\hat{c}^\dagger = \left[\hat{c}_1^\dagger, \hat{c}_2^\dagger, \ldots, \hat{c}_n^\dagger\right]$ is a row vector [81]. Hence,

$$Z = \sum_{\phi_{i,l}=\pm 1} \det\left(\mathbb{I} + B_{L_\tau,\uparrow} B_{L_\tau-1,\uparrow} \ldots B_{1,\uparrow}\right) \det\left(\mathbb{I} + B_{L_\tau,\downarrow} B_{L_\tau-1,\downarrow} \ldots B_{1,\downarrow}\right) \tag{2.50}$$

$$= \sum_{\phi_{i,l}=\pm 1} \det M_\uparrow \det M_\downarrow, \tag{2.51}$$

where $M_\sigma = \mathbb{I} + B_{L_\tau,\sigma} B_{L_\tau-1,\sigma} \ldots B_{1,\sigma}$.

Recall that the thermal expectation value of any observable $\hat{O}$ is given by

$$\langle \hat{O} \rangle = \frac{\mathrm{Tr}\left(\hat{O} e^{-\beta H}\right)}{Z}. \tag{2.52}$$

In order to find the expectation value, we need to sample HS fields, $\phi_{i,l}$, according to the probability distribution $(\det M_\uparrow \det M_\downarrow)/Z$; however Z cannot be known *a priori*, thus we employ the use of Markov chains. Each time slice and site is initialized with some initial HS field, and an update is proposed which flips the field at a single site and time slice. This update is then accepted or rejected via the Metropolis algorithm.

A caveat to the DQMC method is the so-called *Fermion sign problem*. This occurs when the weights (probabilities) in the Monte Carlo simulation become negative or complex. To illustrate this, suppose we construct a many-body state $|\Psi\rangle$ by acting on the vacuum state the operator $\hat{c}_{i\sigma}^\dagger$. Depending on the order of creation operators that have been applied to construct this state, acting further on $|\Psi\rangle$ with the operator $\hat{c}_{j\sigma}^\dagger$ will acquire a phase of ± 1. In practice, the order of operators used to construct $|\Psi\rangle$ is not known for the numerical simulation leading to the sign problem. To this end, we introduce a reference system in which the sign problem is absent to reweigh the thermal expectation value

$$\begin{aligned}\langle \hat{O} \rangle &= \frac{\sum_{i,l} \hat{O}(\phi_{i,l}) W(\phi_{i,l})}{\sum_{\phi} W(\phi_{i,l})} \\ &= \frac{\sum_{i,l} \hat{O}(\phi_{i,l}) s(\phi_{i,l}) |W(\phi_{i,l})| / \sum_{i,l} |W(\phi_{i,l})|}{\sum_{i,l} s(\phi_{i,l}) |W(\phi_{i,l})| / \sum_{i,l} |W(\phi_{i,l})|} \\ &= \frac{\langle s\hat{O} \rangle}{\langle s \rangle},\end{aligned} \tag{2.53}$$

where $\phi_{i,l}$ are the HS fields, $W(\phi_{i,l}) = \det M^{\uparrow} \det M^{\downarrow}$, and s is the sign of the weights. The *average Fermion sign* of the system is defined as $\langle s \rangle = Z/Z'$ and is the ratio of the partition function of the system with weights $W(\phi_{i,l})$ and the partition function of a reference system with weights $|W(\phi_{i,l})|$ [82]. If $\langle s \rangle$ is vanishingly small, statistical fluctuations will hinder the evaluation of $\langle \hat{O} \rangle$, reflecting that evaluating this expectation value is exponential in complexity rather than polynomial. At low temperature ($T \to 0$) however, there can be a reduction in the sign problem due to the system partition function Z and the reference partition function Z' approaching the same ground state. For the case of Fermions, a good reference can be chosen such that $Z \geq Z'$, which will place a lower bound on the sign.

The value of the average sign is generally sensitive to model parameters [83, 84], in particular strength of interaction. An extreme case is the doped Hubbard model at low temperature, where the particle-hole asymmetry results in a small average sign. There are models where the sign problem is not an issue due to the preservation of particle-hole symmetry, such as the half-filled Hubbard model, or in electron-phonon models like Holstein and SSH.

A further addition to the base DQMC algorithm is the inclusion of the hybrid Monte Carlo (HMC) (sometimes referred to as Hamiltonian Monte Carlo) algorithm. This method formulates and then time evolves an energy conserving Hamiltonian dynamics, to construct global updates with a high acceptance rate, thereby

reducing autocorrelation times and accelerating Monte Carlo simulations. The original application for this algorithm was for calculations in lattice quantum chromodyanmics [85]. For our purposes, we define a fictitious Hamiltonian dynamics to efficiently sample the phonon fields.

To outline the basics of this algorithm, we first redefine the Monte Carlo weights W from DQMC as

$$W(\phi_{i,l}, x) = \exp\big[-S(\phi_{i,l}, x)\big], \tag{2.54}$$

where

$$S(\phi_{i,l}, x) = S_{\mathrm{B}}(x) + S_{\mathrm{F}}(\phi_{i,l}, x), \tag{2.55}$$

is an effective action involving a purely bosonic piece S_{B} and a fermionic piece

$$S_{\mathrm{F}}(\phi_{i,l}, x) = S_{\uparrow}(\phi_{i,l}, x) + S_{\downarrow}(\phi_{i,l}, x) = \mathrm{Tr}\log|G_{\uparrow}(\tau,\tau)| + \mathrm{Tr}\log|G_{\downarrow}(\tau,\tau)|, \tag{2.56}$$

for all τ. The HS fields $\phi_{i,l}$ are treated as constants during updates to the phonon fields, so they will be ignored in this discussion.

For each phonon field x, we introduce a conjugate momentum p and define the following effective Hamiltonian

$$H(x,p) = S(x) + \frac{1}{2}p^T \mathcal{M}^{-1} p, \tag{2.57}$$

where $\mathcal{M}$ is the dynamical mass matrix. From this, we can define the Hamilton's equations of motion

$$\dot{x} = \frac{\partial H}{\partial p} = \mathcal{M}^{-1} p, \tag{2.58}$$

$$\dot{p} = -\frac{\partial H}{\partial x} = \frac{\partial S}{\partial x}. \tag{2.59}$$

Now, momentum is sampled according to the Boltzmann distribution

$$\exp\left(-p^T \mathcal{M}^{-1} p/2\right), \tag{2.60}$$

with $p = \sqrt{\mathcal{M}} R$, where R is a random vector whose elements are sampled from a normal distribution. Going forward, we will set the dynamical mass matrix equal to the identity matrix $\mathcal{M} = \mathbb{I}$ for simplicity. From there, the Hamiltonian dynamics are evolved using the leapfrog integration method

$$p_{t+1/2} = p_t + \frac{\Delta t}{2} f_t, \tag{2.61}$$

$$x_{t+1} = x_t + \Delta t \mathcal{M}^{-1} p_{t+1/2}, \tag{2.62}$$

$$p_{t+1} = p_{t+1/2} + \frac{\Delta t}{2} f_{t+1}, \tag{2.63}$$

for N_t times steps of step size Δt with force $f_t = -\partial S / \partial x_t$. Due to leapfrog integration being symplectic and time-reversible (similar to Hamilton's equations), barring any numerical instabilities, the total energy of the Hamiltonian will be conserved up to $O(\Delta t^2)$ for arbitrarily long trajectories. Finally, HMC accepts or rejects the new (x, p) configuration via the Metropolis algorithm.

A significant component of the HMC algorithm is the evaluation of the action derivative

$$\frac{\partial S}{\partial x} = \frac{\partial S_{\mathrm{B}}}{\partial x} + \frac{\partial S_{\mathrm{F}}}{\partial x}, \tag{2.64}$$

specifically, the evaluation of the fermionic part being the most intensive (scaling as $O(\beta N^3)$, for system size N) [86]. For spin species σ, the derivative of Equation 2.56 is

$$\frac{\partial S_{\mathrm{F},\sigma}}{\partial x_{l,\nu}} = \mathrm{Tr}\left[\frac{\partial B_{l,\sigma}}{\partial x_{l,\nu}} B_{l,\sigma}^{-1}(G_\sigma(\tau,\tau) - \mathbb{I})\right], \tag{2.65}$$

where l is the imaginary time slice and ν is the phonon mode. Placing in propagator matrices of the form $B_{l,\sigma} = \exp(-\Delta\tau V_{l,\sigma})\exp(-\Delta\tau K_{l,\sigma})$, then the derivative becomes

$$\frac{\partial S_{\mathrm{F},\sigma}}{\partial x_{l,\nu}} = \mathrm{Tr}\left[\frac{\partial \Lambda_{l,\sigma}}{\partial x_{l,\nu}} \Lambda_{l,\sigma}^{-1}(G_\sigma(\tau,\tau) - \mathbb{I})\right] \tag{2.66}$$

$$+ \mathrm{Tr}\left[\frac{\partial \Gamma_{l,\sigma}}{\partial x_{l,\nu}} \Gamma_{l,\sigma}^{-1}(\Lambda_l^{-1} G_\sigma(\tau,\tau) - \mathbb{I})\Gamma_l\right], \tag{2.67}$$

where $\Lambda_{l,\sigma} = \exp(\Delta\tau V_{l,\sigma})$ and $\Gamma_{l,\sigma} = \exp(\Delta\tau K_{l,\sigma})$. This base HMC algorithm still suffers with long correlation times due to the disparate timescales resulting from the bosonic action S_{B}; however, refining this method to incorporate exact Fourier acceleration and combining it with global updates reduces autocorrelation times and any issues with ergodicity [86].

Compiling all of these ingredients together, we can see the general structure of a DQMC simulation in Algorithm 4. Starting with random initial HS s and phonon fields x, we first thermalize the system for N_{therm} updates. Within this loop, we perform local and HMC updates as well as tuning the chemical potential [87]. Next, we iterate over N_{bins} to obtain measurements, making the same updates, before writing measurements to file.

Algorithm 4 Overview of DQMC simulation structure

Initialize Ising HS fields ϕ and phonon fields x to random initial configuration.
for $i \in [1, N_{\text{therm.}}]$ **do**
    Update Ising HS field ϕ
    Update phonon fields x.
    Update chemical potential.
end for
for bin $\in [1, N_{\text{bins}}]$ **do**
    for $i \in [1, n_{\text{bin}}]$ **do**
        Update Ising HS field ϕ.
        Update phonon fields x.
        Make measurements.
        Update chemical potential.
    end for
    Write average value of measurements in current bin to file.
end for
Average binned measurements to get final estimates for measured observables.

2.3.4 Assessing system properties using DQMC

A standard quantity that is computed by DQMC is the structure factor

$$S_\gamma(q,\tau) = \frac{1}{N}\sum_{i,\mathbf{j}} e^{-\mathrm{i}q\cdot(R_i - R_\mathrm{j})}\left\langle \hat{O}_{\gamma,i}(\tau)\hat{O}^\dagger_{\gamma,\mathbf{j}}(0)\right\rangle, \tag{2.68}$$

where the γ index can denote spin (s), bond (b), or pairing (p) correlations. To assess critical behavior (i.e. the behavior at a phase boundary), we compute the correlation ratio from the equal-time structure factors

$$R_\gamma(L) = 1 - \frac{S_\gamma(Q-\delta q_L, 0)}{S_\gamma(Q,0)},$$

where L denotes the cluster size, $|\delta q_L|$ is the smallest wavevector on the lattice, and Q is the ordering wavevector for the relevant order. R_γ is a renormalization group scale invariant quantity such that for sufficiently large L, the crossing of points for different cluster sizes will determine the critical point. This allows for the access to ground state properties [88–91]. Based on the definition of R_γ, as $R_\gamma \to 1$ for $L \to \infty$, the system will be in an ordered phase. Conversely, if $R_\gamma \to 0$, the system is disordered.

CHAPTER 3:
STRIPE CORRELATIONS IN THE TWO -DIMENSIONAL HUBBARD-HOLSTEIN MODEL

To many Humans, a mystery is irresistible.
It must be solved.

— Capt. Jean-Luc Picard, *Star Trek: The Next Generation*

This Chapter contains text from published work by the author [92] *with minor modifications where appropriate for this format. The author's contribution was doing all variational Monte Carlo simulations with input from Seher Karakuzu, including collecting the data, performing the analysis, and producing the figures.*

3.1 Introduction

The prevailing view of the high-temperature (high-T_c) cuprate superconductors is that they are governed by intertwined orders [93]. In this scenario, different coupled spin and charge orders (i.e., stripes) and their fluctuations compete/cooperate with unconventional superconductivity giving rise to a complex phase diagram [18, 93, 94]. This behavior is observed not only experimentally [10, 18, 95–98] but also in single- and multi-band Hubbard models [13–15, 99–105, 105–115]. For example, non-perturbative numerical methods that access zero-temperature properties frequently identify several nearly degenerate stripe and d-wave superconducting states for model parameters that are relevant to the cuprates [13–15, 17, 106, 110, 110, 111]. The state that ultimately wins out as the ground state, however, is sensitive to subtle factors like the value of the next-nearest-neighbor hopping t' [15, 110].

At finite temperature, Quantum Monte Carlo (QMC) methods [108, 109] find fluctuating spin stripes at $T \sim 0.22t$, where t is the nearest neighbor hopping integral. More recently, weaker charge stripe fluctuations have been reported in

DCA simulations on large extended clusters [113], where the charge correlations were observed to develop after the spin correlations as the temperature is lowered in the hole-doped system. This hierarchy of the spin and charge correlations appears to be a general property of the singleband Hubbard model at finite temperature; it has been observed in subsequent finite-temperature constrained-path auxiliary-field QMC [114] and DQMC [112] simulations. Curiously, the behavior in real cuprates is reversed, where charge modulations tend to develop before spin modulations [18].

The above mentioned results cast doubt on the idea that the Hubbard model is the correct low-energy effective model for the cuprates [15, 25, 105]. If this is true, then it is essential it identify the missing ingredient. While it is clear that strong electron correlations dominate cuprate physics, there is also a growing body of evidence that electron-phonon (e-ph) interactions are also relevant [26, 27, 32, 116–125]. For example, several resonant inelastic x-ray scattering (RIXS) experiments have found evidence for short-range charge-density-wave (CDW) order [126, 127], which appears to couple to the lattice as evidenced by anomalous softening of several oxygen phonon branches in the vicinity of the ordering wave-vector [32, 122–124]. This behavior calls for studies of the influence of the e-ph interaction on stripe order, particularly in light of the apparent sensitivity of stripes to perturbing interactions like t'.

The single-band Hubbard-Holstein model is the minimal model describing correlated electrons coupled to the lattice. This model has been widely studied at half-filling, where competition between antiferromagnetic Mott and $\mathbf{Q} = (\pi/a, \pi/a)$ CDW insulating phases is commonly observed [76, 128–134]. Away from half-filling, there are suggestions that the e-ph interaction can enhance d-wave pairing correlations for some parameter regimes [131, 135, 136]. However, we know comparatively little about how the e-ph interaction might influence stripe correlations and their competition with superconductivity.

Here we present a combined VMC and DQMC study of the two-dimensional doped Hubbard-Holstein model to determine how the Holstein coupling alters

static and fluctuating stripe correlations. We find that the coupling to the lattice can enhance the charge component of the stripes while also suppressing their spin component, depending on the value of the specific model parameters. Our results show that the *e*-ph coupling can alter the balance between the stripe and superconducting correlations and suggest a potential solution to how charge-stripes might appear before spin-stripes in a real material.

3.2 Results

We first examine the static stripe order in the Hubbard-Holstein model at $T = 0$ using VMC (see Chapter 2, Sections 2.1, 2.2.1, 2.3.2), focusing on the $\langle n \rangle = 0.875$, $t' = -0.25t$, and $U = 8t$ case (see Appendix A). Additional results for $t' = 0$ are also shown here and in Appendix B. For these parameters, we find that a long-range static stripe order produces a lower estimate for the ground state energy than a uniform state. For example, Figs. 3.1a and 3.1b plot the expectation values of the local staggered spin $S_i^{\text{stag}} = (-1)^{i_x+i_y}\langle \hat{S}_i^z \rangle$ and local excess hole density $\rho_i = 1 - \langle \sum_\sigma \hat{n}_{i,\sigma} \rangle$ operators, respectively, obtained from our optimized variational state when the *e*-ph coupling $\lambda = 0$. The results reveal the typical intertwined unidirectional spin and charge stripe observed in the cuprates, where antiphased regions of AFM ordered spins are separated by vertical hole-rich regions. For this value of t', the spin and charge modulations have periods $\frac{1}{2}\lambda_{\text{spin}} = \lambda_{\text{charge}} \approx 4a$. We also find that the stripe solution is lower in energy for $t' = 0$, but with a different period $\frac{1}{2}\lambda_{\text{spin}} = \lambda_{\text{charge}} \approx 8a$, see Appendix A. These results are in agreement with a prior VMC study [14] of the Hubbard model that utilized square clusters, suggesting that our choice of cluster geometry does not introduce a significant bias towards the stripe solution.

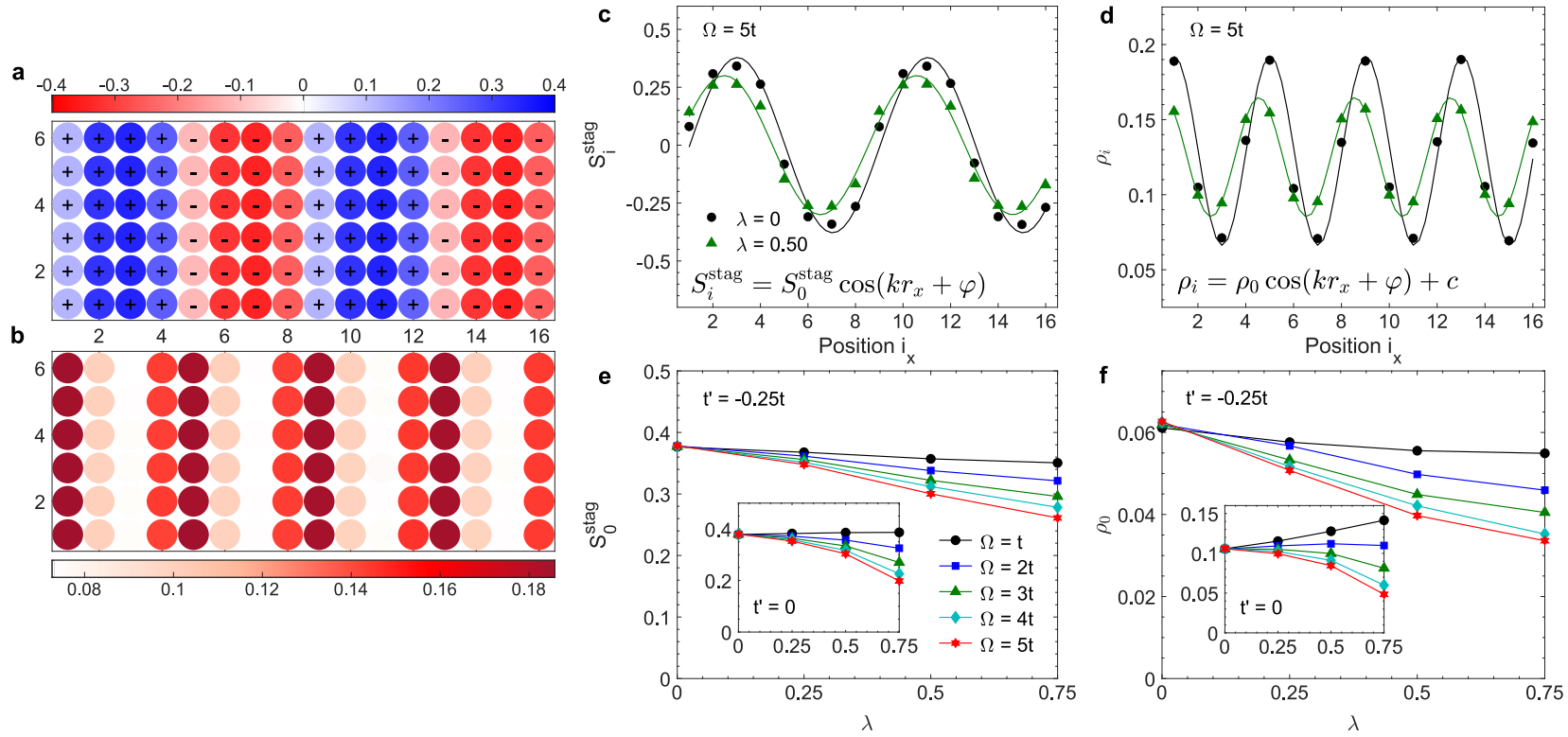

Figure 3.1: VMC results for static stripe order in the two-dimensional Hubbard-Holstein model. (a) The expectation value of the staggered local spin operator in real space $S_i^{\text{stag}} = (-1)^{i_x+i_y}\langle\hat{S}_i^z\rangle$, where $S_i^z = \frac{1}{2}(\hat{n}_{i,\uparrow} - \hat{n}_{i,\downarrow})$ is the z-component of the local spin operator. Results are shown here for $U = 8t$, $t' = -0.25t$, $\langle n\rangle = 0.875$, and $\lambda = 0$. (b) The expectation value of the local excess hole density $\rho_i = 1 - \langle\sum_\sigma \hat{n}_{i,\sigma}\rangle$ for the same case. Panels (c) and (e) show S_i^{stag} and ρ_i, respectively, along the line $(i_x, 0)$ for representative values of $\lambda = 0,\ 0.5$ and $\Omega = 5t$. The data points are the VMC values of the local quantity and the solid lines are sinusoidal fits to the VMC data. Panels (d) and (f) show the fitted amplitudes of the spin and charge modulations, respectively, as a function of λ for $t' = -0.25t$ and various Ω. The insets of these panels show corresponding data for $t' = 0$.

In the limit of $\Omega \to \infty$, the Holstein model can be mapped onto an effective, attractive Hubbard model with $U = -\lambda W$, reflecting the effective, attractive e-e interaction mediated by the lattice. Therefore, for large Ω, we can crudely estimate the effects of the e-ph coupling by replacing $U \to U_{\text{eff}} = U - \lambda W$. For smaller Ω, this picture still provides a valuable guide for qualitatively understanding the physics of the model; however, additional retardation effects can play a role [129, 130, 133]. Based on these considerations, we naively expect $\lambda \neq 0$ will suppress any correlation-driven phenomena for large Ω. Indeed, prior theoretical work at half-filling has shown that the line $\lambda W \approx U$ defines an approximate boundary between AFM and CDW phases [76, 128–130, 133, 134].

With this picture in mind, we now examine the influence of the e-ph coupling on the static stripes. Figs. 3.1c and 3.1d plot S_i^{stag} and ρ_i along the $\mathbf{R}_i = a(i_x, 0)$ direction for representative values of $\lambda = 0,\ 0.5$ and $\Omega = 5t$. (The data for the other values of Ω are similar and provided in Appendix A.) A non-zero coupling $\lambda \neq 0$ reduces the magnitude of both modulations as is evident in the raw VMC data, plotted here as the data points. To quantify this observation across our entire set of simulations, we fit the VMC data with sinusoidal functions, as exemplified by the solid lines. The fitted amplitudes for S_i^{stag} and ρ_i are plotted in Figs. 3.1e and 3.1f, respectively, where results for $t' = -0.25t$ are shown in the main panel and results for $t' = 0$ are shown in the insets.

For both values of t', we find that the Holstein interaction does not change the underlying period of the stripes. It can, however, shift the stripes from being site-centered to bond-centered for some model parameters. For example, when $t' = -0.25t$ we obtain a site-centered stripe when $\lambda = 0$, which shifts to being bond-centered when $\lambda \neq 0$, as shown in Figs. 3.1c and 3.1d. This shift occurs for almost all of the non-zero values of the e-ph coupling that we have checked (see Appendix A). Conversely, when $t' = 0$, we mostly obtain a bond-centered stripe, independent of the values of λ and Ω.

The e-ph coupling also affects the amplitudes of the spin and charge modulations. Increasing λ for $t' = -0.25t$ suppresses both the spin and charge modulations, and the rate of suppression increases as the phonon frequency Ω increases. We find qualitatively similar behavior for large Ω when $t' = 0$, as shown in the insets. However, for lower energy phonons ($\Omega \lesssim 2t$), the spin modulations are weakly suppressed when $\lambda \leq 0.75$ while the amplitude of the density modulations increases. These results indicate that a Holstein coupling to high-energy phonons suppresses static stripe order while coupling to lower-energy optical modes can stabilize them by enhancing their charge modulations, depending on the value of t'.

Having assessed the effects of the e-ph coupling on stripe correlations, we now turn to the relative energies of the stripe and superconducting states. Figs. 3.2 and 3.3 compare the variational energies of the stripe and uniform solutions for $t' = 0$ and $-0.25t$, respectively. Focusing first on the $t' = 0$ case, Fig. 3.2a plots the expectation value of the system's total energy as a function of λ for the optimized variational stripe states, like those shown in Fig. 3.1. The stripe state's energy decreases approximately linearly with λ for all Ω, but the rate of decrease is higher for larger phonon energies. The inset of Fig. 3.2a shows the corresponding data for a uniform state, where we observe similar behavior.

The dominant contribution to change in energy can be attributed to the shift in the lattice's equilibrium position when $\lambda \neq 0$ [130], which lowers the energies of the uniform and stripe states by a comparable amount. More subtle differences are observed when we examine the energy differences between the two states, as shown in Fig. 3.2b. When $\lambda = 0$, we find that the stripe state is $0.01437t$/site lower in energy than the uniform state, such that the stripe solution is a better approximation for the ground state at this doping, consistent with Refs. [14] and [111]. For $\Omega > 2t$, increasing λ reduces the energy difference between these states, signaling that the stripe state is suppressed relative to the uniform superconducting state. Conversely, for $\Omega = t$, increasing λ stabilizes the stripe order. For intermediate $\Omega = 2t$, we

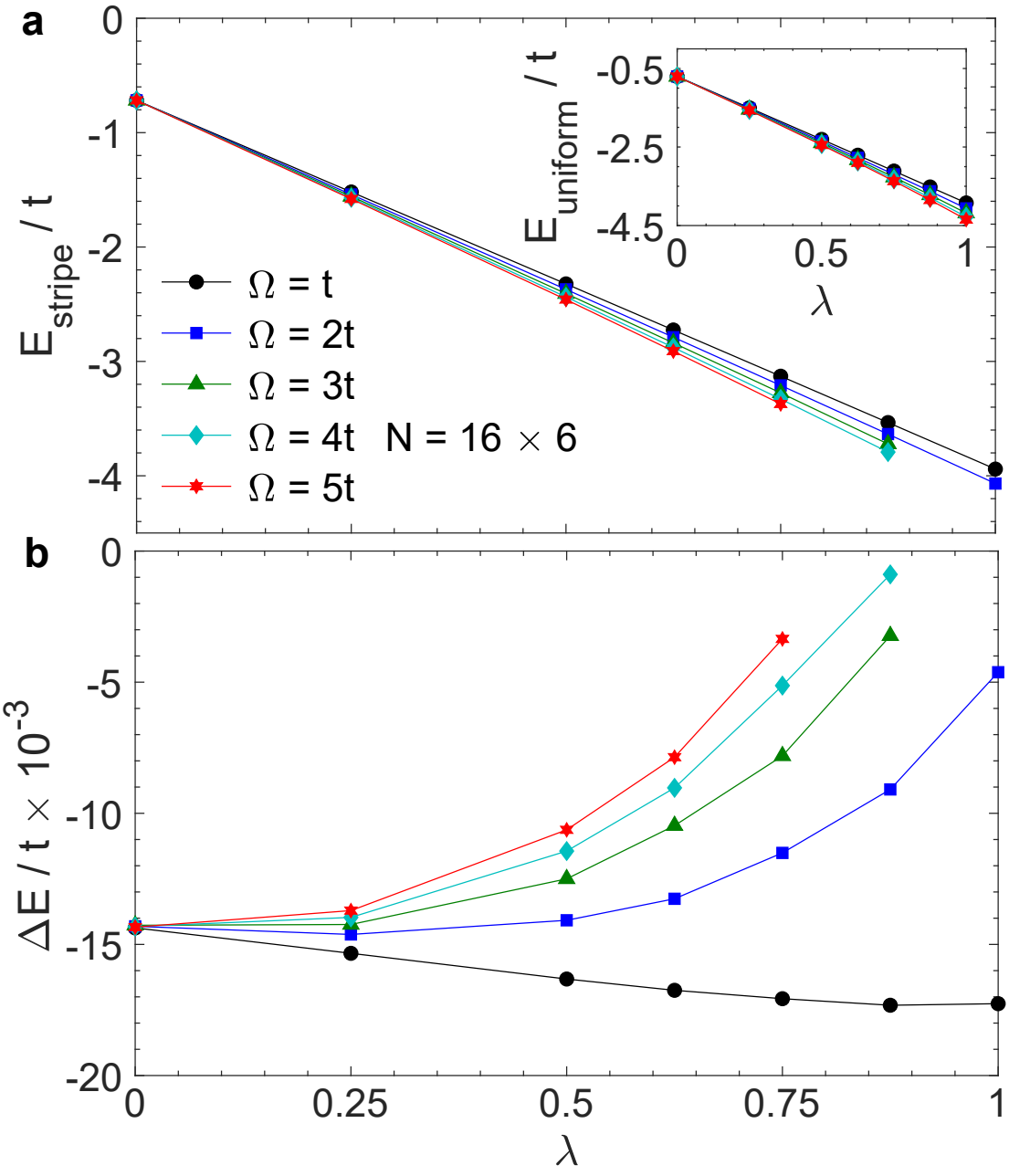

Figure 3.2: Variational Monte Carlo estimates for the energies of the two-dimensional Hubbard-Holstein model with $t' = 0$ and various phonon energies Ω as a function of λ. Panel (a) shows the expectation value of the Hamiltonian E_{stripe} for a state with static spin and stripe correlations. The inset shows the expectation value of the Hamiltonian E_{uniform} for a state with uniform d-wave pairing and AFM correlations. Panel (b) plots the difference $E_{\text{stripe}} - E_{\text{uniform}}$ as a function of λ. All energies are reported in units of t.

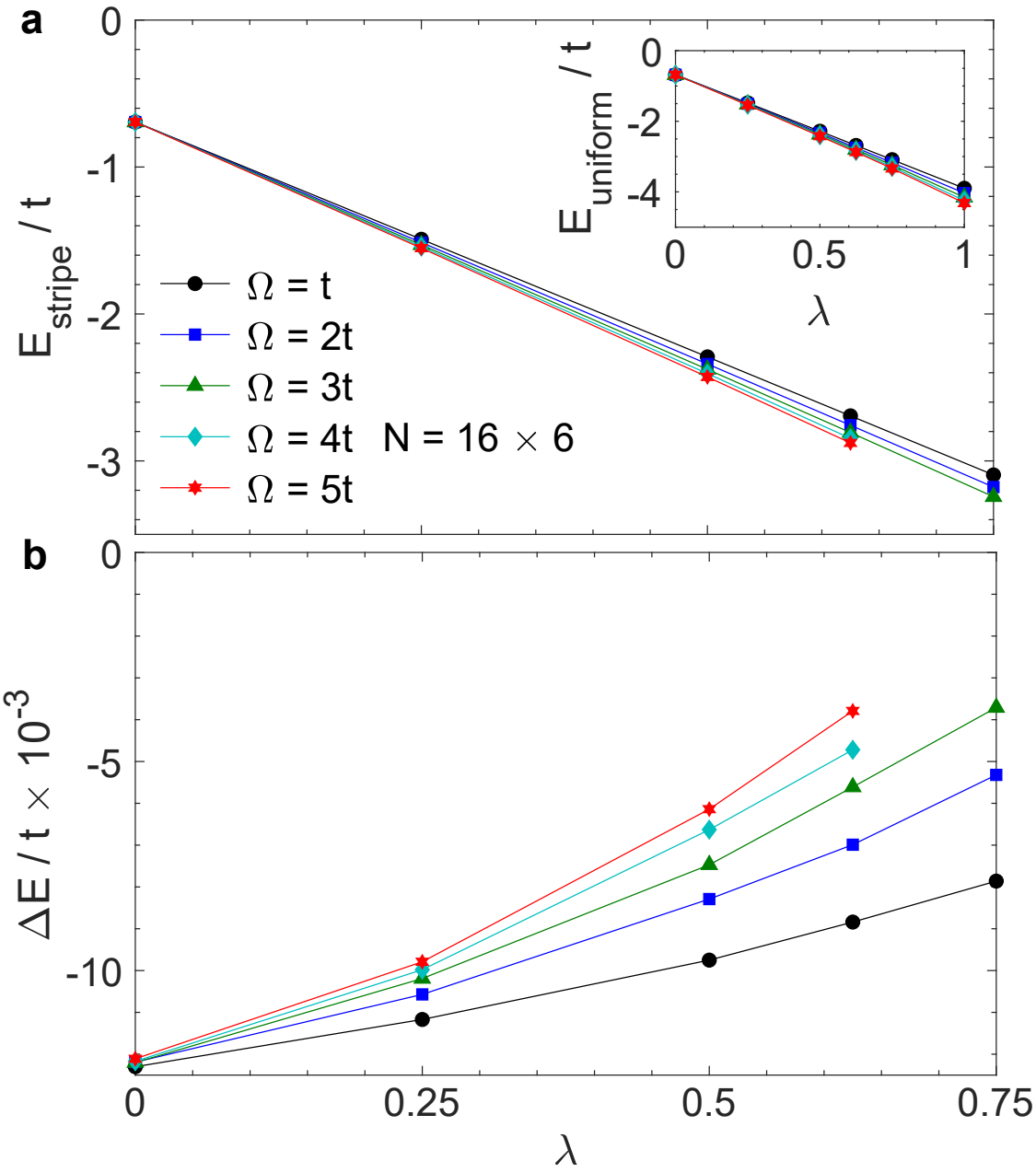

Figure 3.3: Variational Monte Carlo estimates for the energies of the two-dimensional Hubbard-Holstein model with $t' = -0.25t$ and various phonon energies Ω as a function of λ. Panel (a) shows the expectation value of the Hamiltonian E_{stripe} for a state with static spin and stripe correlations. The inset shows the expectation value of the Hamiltonian E_{uniform} for a state with uniform d-wave pairing correlations and AFM order. Panel (b) plots the difference $E_{\text{stripe}} - E_{\text{uniform}}$ as a function of λ. All energies are reported in units of t.

observe nonmonotonic behavior, where the stripe correlations are enhanced at small $\lambda < 0.5$ but suppressed for larger values.

The results for $t' = -0.25t$, shown in Fig. 3.3, show that the e-ph coupling lowers the energy difference between the stripe and uniform solutions at all Ω. However, the effect is reduced as the phonon energy decreases.

The results in Figs. 3.1-3.3 suggest that anti-adiabatic phonons destabilize static stripe order relative to the uniform state by suppressing both the spin and charge modulations. However, lower-energy phonons can have the opposite effect, increasing the strength of charge modulations while leaving the spin modulations relatively unchanged when $t' = 0$. While we can understand the large Ω behavior in terms of a reduced U_{eff}, the small Ω behavior, which is more relevant for the high-T_c cuprates, highlights the critical role of retardation. For example, studies examining the competition between AFM and CDW in the half-filled Hubbard-Holstein model generally find that the AFM correlations can persist beyond the line defined by $U = \lambda W$ when $\Omega \leq t$. In this regime, the lattice cannot respond quickly enough to the double occupations created in the AFM exchange process and is less effective in suppressing the AFM correlations. A similar effect appears to be at play here, as the AFM spin stripe correlations are less affected by the e-ph interaction as Ω decreases. At the same time, smaller values of Ω correspond to softer springs, which means that the hole-rich regions can lower their energy more readily by forming large local lattice distortions for a fixed value of λ. These combined effects provide a plausible explanation for our VMC results.

If the system is in a stable phase, then the ground state energy as a function of filling is convex, i.e. $\partial^2 E(n)/\partial n^2 > 0$. One can determine when this condition is violated by calculating the energy per hole [137]

$$\varepsilon(\delta) = \frac{E(\delta) - E(0)}{\delta}, \tag{3.1}$$

where $\delta = 1 - \langle \hat{n} \rangle$ is the excess hole density. If $\epsilon(\delta)$ has a local minimum at some hole doping δ_c, then the system will phase separate for any $\delta < \delta_c$. Using this approach, several VMC studies have observed a tendency towards phase separation in the lightly hole doped Hubbard model [14, 137, 138]. For example, Ido *et al*. [Ref. [14]] concluded that phase separation occurs for doping levels $\delta < 0.125$ in the singleband model when $U = 10t$ and $t' = 0$. But VMC tends to over predict the value of δ_c; this occurs because the division by δ in Eq. 3.1 magnifies small errors in the variational energies $E(\delta)$ at low doping levels. Indeed, in Ref. [138] systematic improvements of the variational energies via Greens function Monte Carlo with the Fixed Node approximation drove critical doping level δ_c very close to zero. Notably, the nature of the correlations in the ground state did not change as the wave function was improved.

With these caveats in mind, Fig. 3.4 examines $\varepsilon(\delta)$ for our model parameters for completeness. For $\lambda = 0$ [Fig. 3.4a], we find that $\varepsilon(\delta)$ reaches a local minima at $\delta_c = 0.125$ for both $t' = 0$ and $-0.25t$, in agreement with Ref. [14]. Once the *e*-ph interaction is included, the local minima develop at $\delta_c = 0.125$ and 0.167 for $t' = -0.25t$ and all values of Ω, with the latter being the global minimum. The predicted tendency towards phase separation is more severe for the case of $t' = 0$ with the region extending to $\delta_c = 0.229$, as shown in the inset of Fig 3.4b.

These results suggest that the Holstein coupling increases the tendency toward phase separation commonly found in the Hubbard and *t*-*J* models [14, 137, 138]. The doping level of our simulations, indicated by the red arrows, fall below δ_c when $\lambda \neq 0$. However, the local minima are largely determined by the rapid growth in $\varepsilon(\delta)$ at low doping, which can be dramatically impacted by small errors in $E(\delta)$. Indeed, Ref. [138] found that this rapid rise all but disappears in the $\lambda = 0$ case as the variational wave functions are improved. We expect a similar change to occur here for $\lambda \neq 0$; however, more detailed simulations will be needed to verify this conjecture. Nevertheless, we believe that we are overestimating δ_c here, and the

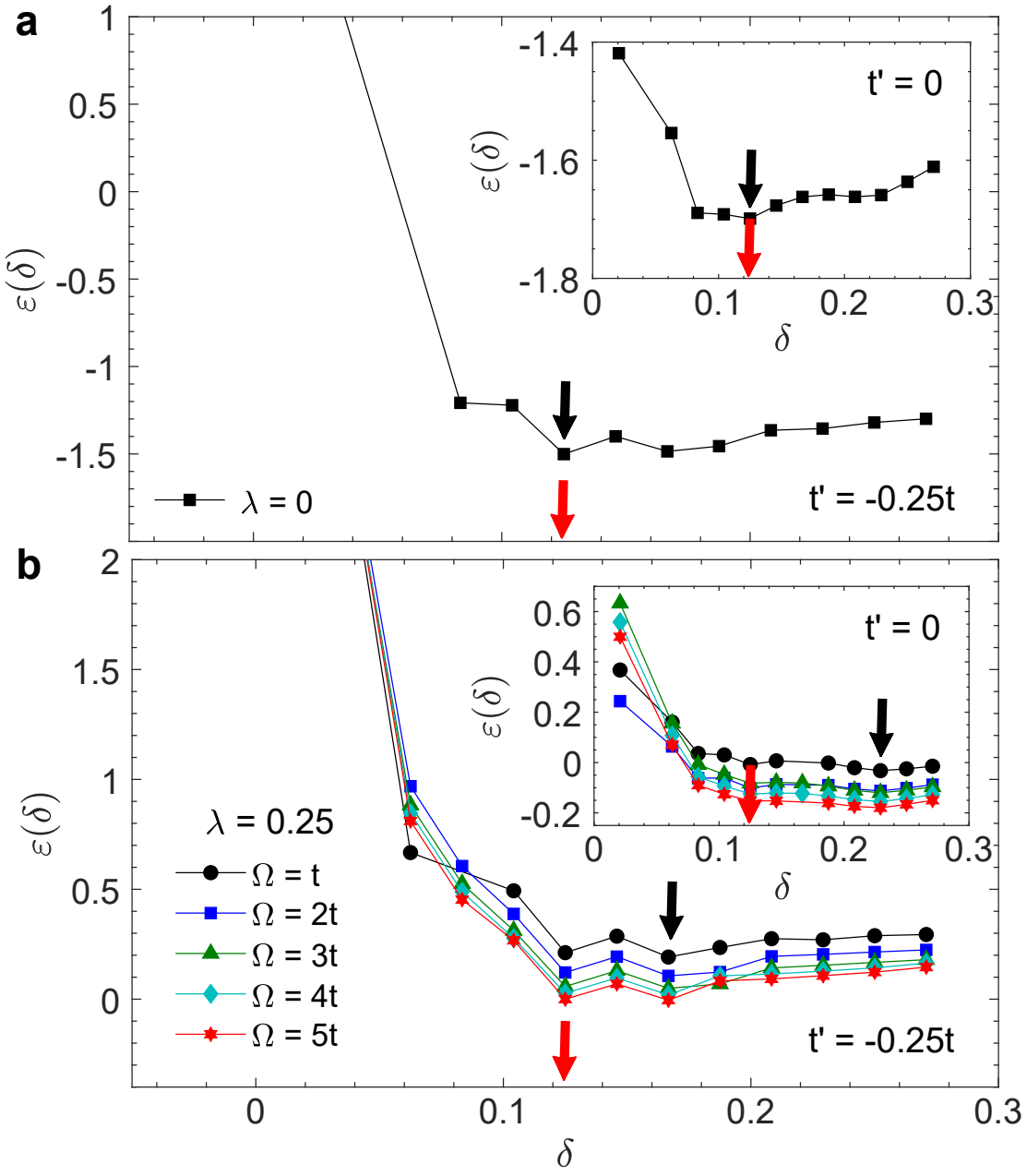

Figure 3.4: The energy per hole $\varepsilon(\delta)$ for $t' = -0.25t$ and $t' = 0$ (insets) at different phonon energies. The red arrows indicate the doping level of the VMC calculations shown in Figs. 3.1-3.3. The black arrows indicate the global minimum of $\varepsilon(\delta)$. Panels (a) and (b) show the energy per hole for $\lambda = 0$ and $\lambda = 0.25$, respectively.

actual value is smaller. This conjecture is also supported by the fact that we find no indications for phase separation in our finite temperature DQMC results discussed next.

We now turn to the influence of the Holstein coupling on the fluctuating stripe correlations observed by DQMC at finite temperatures. Fluctuating stripes are challenging to resolve in the Hubbard model at high-temperatures. For this reason, we focused on $N = 16 \times 4$ clusters with $\langle \hat{n} \rangle = 0.8$ with $t' = -0.25t$, $U = 6t$, and $\beta = 4/t$, where the fluctuating spin stripe correlations are particularly strong [109]. Fig. 3.5a plots real-space staggered static spin-spin correlation function

$$C_{\text{spin}}^{\text{stag}}(\mathbf{r}_i) = \frac{1}{N} \int_0^\beta (-1)^{i_x+i_y} \langle \sum_j \hat{S}_{i+j}^z(\tau) \hat{S}_j^z(0) \rangle d\tau,$$

measured in DQMC simulations for several values of λ and $\Omega = t/2$. (Results for $\Omega = t$ and $\Omega = 2t$ are provided in Appendix A.) Fig. 3.5b shows the corresponding static density-density correlation function

$$C_{\text{den}}(\mathbf{r}_i) = \frac{1}{N} \int_0^\beta \sum_j \left[\langle \hat{n}_{i+j}(\tau) \hat{n}_j(0) \rangle - \langle \hat{n}_{i+j}(\tau) \rangle \langle \hat{n}_j(0) \rangle \right] d\tau.$$

For $\lambda = 0$ [top row, Figs. 3.5a, b], we observe fluctuating spin and charge stripe correlations consistent with prior work [108, 109, 113]. The spin correlations are evident from the short-range AFM correlations (blue) surrounded by other AFM domains where the magnetic correlations are flipped (red). At this temperature, the charge stripes are weak but still present.

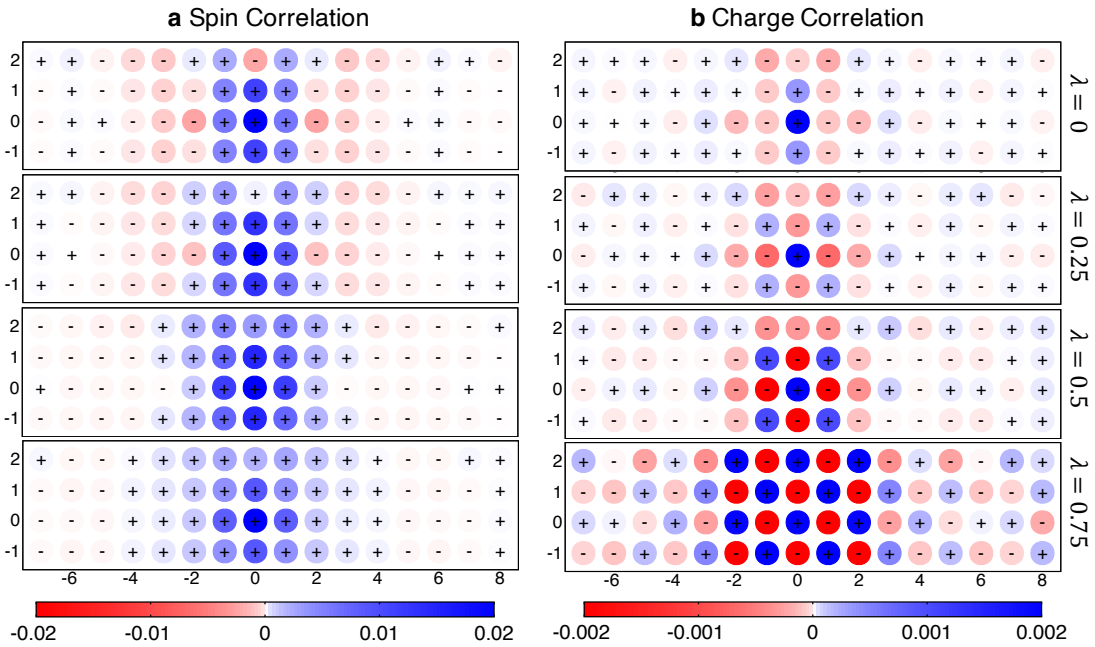

Figure 3.5: Determinant quantum Monte Carlo results for the fluctuating (a) spin and (b) charge stripes in the Hubbard-Holstein model at a filling of $\langle \hat{n} \rangle = 0.8$ and an inverse temperature of $\beta = 4/t$, obtained on $N = 16 \times 4$ clusters with $t' = -0.25t$, $U = 6t$, and $\Omega = t/2$. Each row in (a) shows the real-space static staggered spin-spin correlation function at different values of λ. The panels in (b) show the corresponding density-density correlation functions.

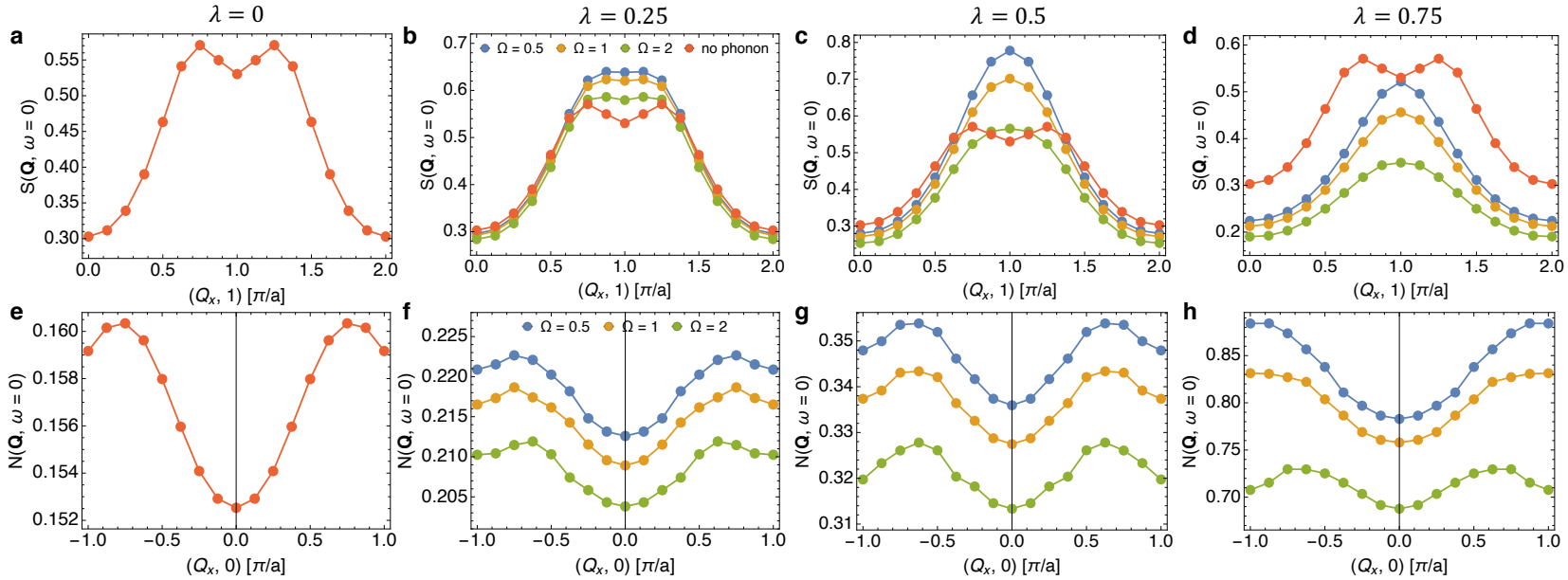

Figure 3.6: Determinant quantum Monte Carlo results for the fluctuating spin and charge stripes of the Hubbard-Holstein model in momentum space. All results were obtained at a filling of $\langle \hat{n} \rangle = 0.8$ and an inverse temperature of $\beta = 4/t$ using $N = 16 \times 4$ clusters with $t' = -0.25t$ and $U = 6t$. The top row shows the static spin susceptibility for different values of λ. The bottom row shows the corresponding charge susceptibility. Results are shown for $\Omega = t/2$, t, and $2t$, as indicated in the legends provided in the second column.

As with the VMC results for this value of t', we find that the spin correlations are reduced when we introduce the e-ph coupling. This suppression occurs gradually for weak coupling, but it accelerates as λ increases. For example, for $\lambda = 0.5$, we already see that the red domains in $C^{\text{stag}}_{\text{spin}}(\mathbf{r}_i)$ are nearly absent while the AFM correlations persist over longer length scales. As λ increases further, the AFM correlations extend over a larger distance. This behavior is presumably due to the attractive interaction mediated by the phonons, which counteracts the correlations generated by the Hubbard U. In contrast to the spin correlations, the charge correlations remain more robust for $\lambda \leq 0.5$ but begin to develop an additional short-range $\mathbf{Q} = (\pi, \pi)$ modulation. These new modulations signal the formation of local bipolarons [38], which tend to arrange themselves in local checkerboard-like order. Finally, the (π, π) modulation dominates over the entire cluster for the largest value of λ studied here.

So far, we have focused on results for $\Omega = t/2$; however, we have obtained similar results for $\Omega = t$ and $2t$ (see also Appendix A). The trends across the data set are more easily summarized by examining the momentum-dependent static spin $S(\mathbf{Q}, \mathrm{i}\omega_n = 0)$ and charge $N(\mathbf{Q}, \mathrm{i}\omega_n = 0)$ susceptibilities, shown in Fig. 3.6. These quantities are obtained by Fourier transforming the unequal time spin-spin and density-density correlation functions and integrating over imaginary time.

The spin stripe correlations manifest in $S(\mathbf{Q}, \mathrm{i}\omega_n = 0)$ as incommensurate peaks at $\mathbf{Q} = (\pi \pm \delta_s, \pi)$. As with the real-space picture, we find that δ_s is reduced for small λ, causing the double peaks to merge into a single broad peak centered at (π, π). However, in most cases, we can still discern two components by fitting a set of Lorentzian functions to the data (see Appendix A). For large λ, $S(\mathbf{Q}, 0)$ approaches a single AFM peak, which is suppressed as Ω increases due to the reduction of U_{eff} and increasing competition with the competing CDW phase.

The charge stripes manifest in $N(\mathbf{Q}, i\omega_n = 0)$ as incommensurate peaks centered at $\mathbf{Q} = (\delta_c, 0)$ [113]. In the absence of e-ph coupling, we clearly observe this structure with $\delta_s/\delta_c \approx 0.45$ at $\beta = 4/t$, consistent with Ref. [113]. These peaks remain

well defined for $\lambda \leq 0.5$ for all values of Ω, while the overall magnitude of the charge correlations increases uniformly with decreasing Ω. It is only for stronger e-ph coupling ($\lambda = 0.75$) that δ_c is shifted towards π as the phonon frequency is decreased, signalling a suppression of the charge stripes. We also note that increasing λ enhances the $\mathbf{Q} = (\pi, \pi)$ charge correlations (see Appendix A) due an increased tendency towards bipolaron formation. In fact, the (π, π) correlations become significantly larger than the $(\delta_c, 0)$ ones if λ is too large, consistent with the real space picture shown in Fig 3.5.

The overall picture obtained from our DQMC results ($t' = -0.25t$) is that the Holstein interaction tends to suppress the fluctuating stripe correlations but that the effect is more pronounced for the spin correlations at small Ω and weak to intermediate coupling. For strong coupling and/or large Ω, the e-ph interaction suppresses both channels due to the competition with (π, π) charge correlations, bipolaron tendencies, or an overall reduction in U_{eff}. These results are in agreement with our zero-temperature VMC results for $t' = -0.25t$. These results demonstrate that the e-ph interaction can have a non-trivial effect on static and fluctuating stripe correlations.

3.3 Discussion

Several numerical methods have found evidence that a Holstein interaction can enhance d-wave pairing correlations in the doped singleband Hubbard-Holstein model [131, 135, 136]. Some researchers have linked this enhancement to a non-trivial screening of the e-ph interaction, which reduces large-$\mathbf{q}$ scattering relative to small $\mathbf{q}$ [27, 34, 135]. Our results suggest that the lattice can affect superconductivity in another way by altering the competing stripe phases. Different optical phonon branches can play different roles in this context: high-energy phonons generally suppress both spin and charge stripes. In contrast, low-energy phonons can enhance

them by increasing the charge modulations. Since cuprate optical oxygen phonons have $\Omega \leqslant t/3$, we expect that the latter regime is more relevant to these materials. Our results, therefore, provide a natural framework for understanding anomalous oxygen isotope effects observed in materials like $La_{2-x}Sr_xCuO_4$ [139]. They also suggest an explanation for why charge modulations tend to develop before spin modulations in the cuprates, even though fluctuating spin stripes appear to be stronger in the doped Hubbard model.

Why does the e-ph interaction primarily couple to the charge modulations? To some extent, this might be expected since the phonons couple directly to the local charge density. There are other factors to consider, however. For one, stripe formation is a form of phase separation that emerges as a compromise in balancing the doped carriers' kinetic and potential energies. Several QMC studies of the Holstein model have found evidence that it is prone to phase separation when doped away from half-filling [76, 140, 141], which is stronger for low-energy phonons at high temperatures [76, 141]. An enhancement of the e-ph coupling at small-$\mathbf{q}$ can further exacerbate this tendency [142, 143]. In the case of the doped Hubbard-Holstein model, these factors then cooperate in collecting the doped carriers into particular spatial regions of the system, which would explain our observations.

Many models and experimental measurements on the cuprates estimate the dimensionless e-ph coupling to the oxygen-derived phonon modes to be in the range $\lambda \sim 0.3 - 1$ [26, 27, 116–118, 120]. Combined with our results, these estimates suggest that the e-ph coupling could play a role in shaping the stripe correlations. The relevant phonon frequencies in the real materials ($\Omega \approx t/3$) are smaller than the values considered here. With this in mind, our results for $t' = -0.25t$ suggest that a Holstein interaction will be insufficient for stabilizing the superconducting state. However, more sophisticated e-ph models must also be examined before we can draw definitive conclusions about the real materials. For example, coupling to the bond-buckling modes occurs via the oxygen on-site (potential) energy and has a significant momentum dependence [34, 116], unlike the Holstein model studied here. Similarly,

coupling to the bond-stretching modes occurs via a Su-Schrieffer-Heeger (SSH) type interaction [34, 116], which modulates the carrier's kinetic energy [46, 144]. (The latter case is particularly interesting since the largest phonon softening in the cuprates typically occurs for the high-energy bond-stretching modes in proximity to CDW order [32, 122].) To fully understand the role of these interactions on cuprate stripes, it will be necessary to study generalizations of the three-band model, which can capture these aspects of the relevant phonon modes. Nevertheless, our results demonstrate that *e*-ph coupling cannot be neglected in any complete picture of stripe physics.

CHAPTER 4:
COMPARATIVE STUDY OF THE SUPERCONDUCTIVITY IN THE HOLSTEIN AND OPTICAL SU-SCHRIEFFER-HEEGER MODELS

You can use logic to justify almost anything.
That's its power. And its flaw.

— Capt. Kathryn Janeway, *Star Trek: Voyager*

This Chapter contains text from published first author work by the author [145] *with minor modifications where appropriate for this format. The author's contribution was doing all simulations with input from Benjamin Cohen-Stead, including collecting the data, performing the analysis, and producing the figures. The author wrote most of the manuscript with input from the coauthors.*

4.1 Introduction

Identifying the highest superconducting transition temperature T_c that can be realized for a given pairing interaction persists as a significant unsolved problem [146–156]. In particular, there is a long-standing discussion over whether the T_c arising from the electron-phonon (e-ph) interaction is bounded [146–149, 155]. While Eliashberg theory predicts that T_c increases indefinitely with the dimensionless e-ph coupling λ [148], lattice instabilities or competing phases like CDW order are expected to ultimately cut off this growth [147, 151]. For example, even if one could avoid a lattice instability, the formation of heavy (bi)polarons should suppress superconductivity in the strong coupling limit [157]. These expectations have been recently confirmed by numerical calculations for the Holstein model [154, 155, 158], suggesting polaron formation sets an intrinsic limit on phonon-mediated superconductivity.

In this context, SSH-like (e-ph) interactions, where the atomic motion modulates the electronic hopping integrals [39, 159], have attracted substantial interest [46, 47, 144, 160–168]. Recent theoretical studies in the dilute limit suggest that this interaction can produce strongly bound yet light bipolarons less prone to localization [46], in contrast to the Holstein model. It has also been proposed [47] that a dilute gas of such bipolarons will have an instability toward a superconducting state with T_c's much larger than those estimated for the Holstein model [155]. Importantly, pairing mediated by the SSH interaction is also believed to be robust against the inclusion of repulsive e-e interactions [47, 164], thus providing a means to bypass the proposed limits of conventional superconductivity.

The T_c estimates obtained in Ref. [47] are based on simulations of the 2D bSSH model, where the properties of an isolated bipolaron on a lattice are computed with numerically exact QMC methods [169]. The authors then argue that the system in the dilute limit can be regarded as a gas of bipolarons and mapped onto the problem of a gas of hard-core bosons, where T_c was identified with the superfluid transition temperature [170]. This approach should be accurate in the dilute limit, where the bipolarons do not overlap significantly [47]. While these results suggest that SSH interactions may be able to mediate high-T_c superconductivity, many materials hosting these types of interactions are far from the dilute limit. As the carrier concentration increases, one naturally expects other ordering tendencies to appear that will compete with superconductivity, e.g., a CDW phase for the Holstein model [36, 141, 171–175]. For the 2D bond SSH model, studies have identified insulating CDW order [144, 165], a BOW [161] phase, and even weak antiferromagnetism [163, 176] near half-filling. It is thus desirable to assess the strength of the relevant pairing correlations in the SSH model and any competing instabilities across a wide range of carrier concentrations and model parameters.

Here we present a comparative study of the 2D Holstein [35], bond [62], and optical [48] SSH models using numerically exact and sign-problem free DQMC simulations. Focusing on the weak coupling limit, where the linear approximation

for the SSH interaction is valid [166, 177], we find that the models have strong CDW (Holstein) or BOW (bSSH/oSSH) correlations near half-filling. These phases are suppressed upon doping and give way to strong superconducting correlations in the antiadiabatic limit, where the phonon energy is much larger than the electronic hopping ($\Omega/t \gg 1$, $\hbar = 1$). In this case, we further find that the Holstein and oSSH models produce comparable pairing correlations over a wide range of carrier concentrations. In contrast, correlations in the bSSH model are notably weaker. For smaller phonon energies ($\Omega/t = 0.5$), we find that the SSH models can support robust pairing in proximity to their competing bond order at half-filling, while the Holstein model is prone to the formation of heavy bipolarons in the same window. Further doping into the dilute limit shows that all three models have weak but comparable superconducting correlations. Finally, we find that including a modest Hubbard $U = t/2$ suppresses the pairing correlations of the doped SSH models.

These results provide new insight into the search for bipolaronic superconductors and suggest that one should look toward weakly correlated materials with carrier concentrations close to their relevant competing order.

4.2 Results

We adopt the Brillouin zone average definition of the dimensionless coupling such that $\lambda_{\mathrm{h}} = \frac{\alpha_{\mathrm{h}}^2}{M_{\mathrm{h}}\Omega^2 W}$, $\lambda_{\mathrm{b}} = \frac{4\alpha_{\mathrm{b}}^2}{M_{\mathrm{b}}\Omega^2 W}$, and $\lambda_{\mathrm{o}} = \frac{8\alpha_{\mathrm{o}}^2}{M_{\mathrm{o}}\Omega^2 W}$ as discussed in Chapter 2, Section 2.2.3. To ensure that the value of the dimensionless coupling remains the same among the three models, we fix the ratios of the microscopic couplings to $\alpha_{\mathrm{o}}^2 = \alpha_{\mathrm{H}}^2/8$ and $\alpha_{\mathrm{b}}^2 = \alpha_{\mathrm{H}}^2/4$. Note that our definition for λ_{b} differs from Ref. [47] by a factor of two. Therefore, the momentum dependence of $g_\nu^{\mathrm{b}}(k, q)$ was neglected and the ratio $\alpha_{\mathrm{b}}^2 = \alpha_{\mathrm{H}}^2/2$ was adopted. For this reason, the strength of the coupling to the bond model is stronger in their analysis.

Figure 4.1 compares the s-wave pair-field $\chi_{\mathrm{p}}(\mathbf{q})$, charge $\chi_{\mathrm{c}}(\mathbf{q})$, and bond-order $\chi_{\mathrm{b}}(\mathbf{q})$ susceptibilities for the three models as a function of filling $\langle n \rangle$. Results are

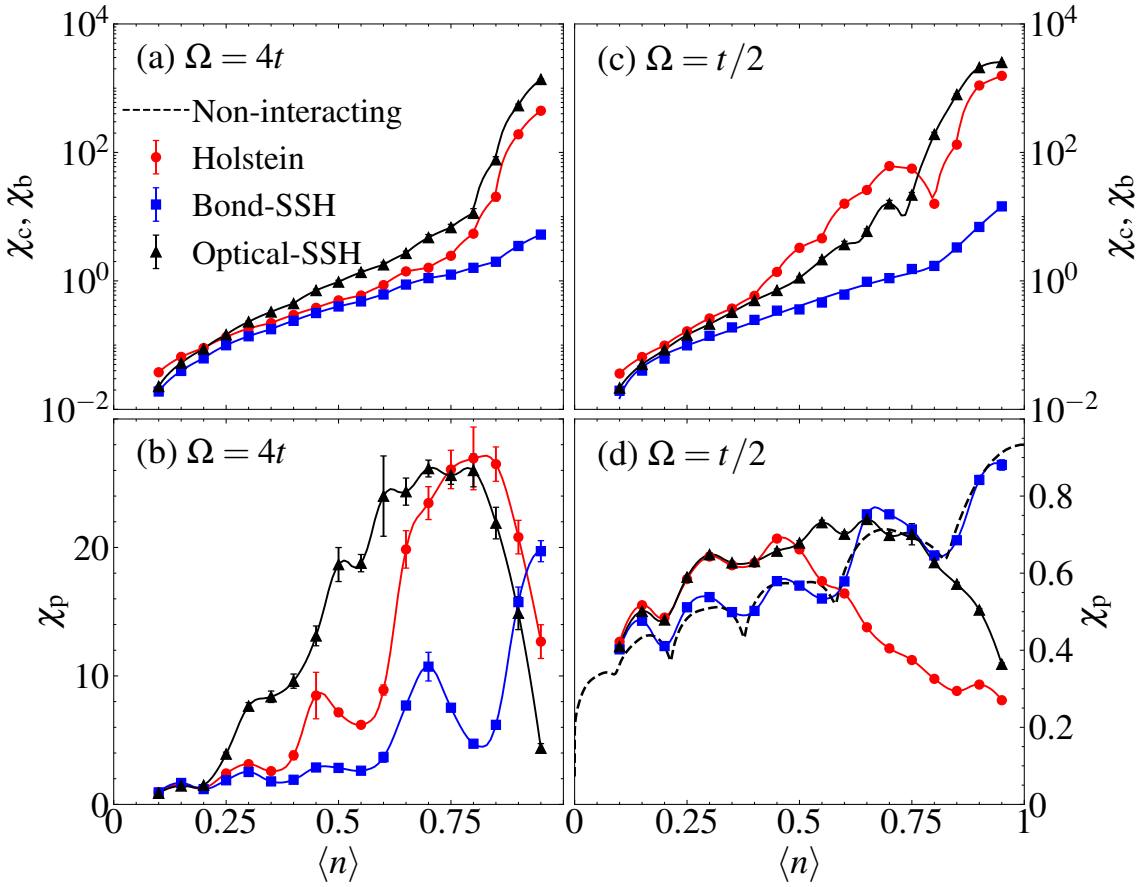

Figure 4.1: DQMC results for pairing and dominant charge/bond correlations obtained on 14×14 lattices at $\beta = 16/t$ and $\lambda = 0.3$. Panels (a) & (c) show results for the CDW $[\chi_c(\pi, \pi)]$ and BOW $[\chi_b(\pi, \pi)]$ susceptibilities. Panels (b) and (d) show singlet s-wave pair-field $[\chi_p(q = 0)]$ susceptibilities for the Holstein (red ○), and bond- (blue □), and oSSH (black △) models. Results for $\Omega = 4t$ ($t/2$) are shown in the left (right) column. The dashed black line in panel (d) is the pair-field susceptibility for the non-interacting model. Note that the charge and bond susceptibilities are plotted on a logarithmic scale, while the pair-field susceptibility is plotted on a linear scale.

shown for $\Omega = 4t$ [panels (a),(b)] and $t/2$ [panels (c),(d)] and were obtained on an $N = 14 \times 14$ cluster with fixed $\beta = 16/t$, and $\lambda = 0.3$. We have found that the uniform s-wave pairing correlations $q = 0$ are the dominant pairing signal for all parameters examined here. In contrast, the dominant CDW and BOW correlations appear at the $\mathbf{q} = (\pi, \pi)$ ordering vector near half-filling. Therefore, we focus on these ordering vectors throughout this work.

Focusing first on the charge and bond correlations, we find that the Holstein and oSSH models are dominated by CDW and BOW correlations for $0.75 \lesssim \langle n \rangle \leq 1$, consistent with prior work [38, 141]. These orders compete directly with superconductivity in each case and become stronger as the phonon energy decreases. Conversely, the bSSH model is characterized by nearly degenerate antiferromagnetic (not shown), superconducting, and CDW correlations near half-filling in the $\Omega = 4t$ case, consistent with prior results for our chosen parameters [161, 163, 176, 178].

The CDW/BOW correlations in all three models are suppressed upon doping away from $\langle n \rangle = 1$ and eventually overtaken by the superconducting correlations. The strongest pairing correlations for the Holstein and oSSH models in the antiadiabatic limit ($\Omega = 4t$, Fig. 4.1b) occur around $\langle n \rangle \approx 0.7 - 0.75$, and have broad dome-like dependence on the carrier concentration. In this case, the suppression of pairing near half-filling is due to competition with the BOW/CDW correlations, while the suppression for small $\langle n \rangle$ is due to the decreased density of carriers. This dome-like behavior is reminiscent of the bismuthates [179] and other quantum materials, where superconductivity is found near a competing order. Notably, the pairing correlations for the oSSH model are comparable to the Holstein model at intermediate doping but decay slower as the band is depleted.

The pairing correlations in the bSSH model are notably smaller and exhibit slightly different dependence on the filling. The largest pairing correlations for this model occur at $\langle n \rangle = 1$. There is also a second narrow peak in $\chi_{\mathrm{p}}(q = 0)$ centered at $\langle n \rangle \approx 0.7$, where the pairing correlations are larger than the BOW correlations. (The exact position of this peak depends on the cluster size, see Appendix D.)

The superconducting correlations decrease dramatically when the phonon energy is lowered to $\Omega = t/2$ (Fig. 4.1d), which is naturally expected for a phonon-mediated pairing mechanism where $T_c \propto \Omega$. At this temperature ($\beta = 16/t$), the pairing correlations of the bSSH model are nearly identical to the non-interacting pair-field susceptibility (indicated by the dashed black line) for all $\langle n \rangle$. Conversely, the correlations in the Holstein and oSSH models are slightly enhanced over the non-interacting values at lower carrier concentrations $\langle n \rangle \lesssim 0.5$; however, $\chi_p(q = 0)$ in both models is similar, suggesting that these models will have comparable T_c's at these carrier concentrations. Moving towards half-filling, χ_p is suppressed below the non-interacting values for both the Holstein and optical-SSH models, but the optical model's pairing correlations persist to comparatively higher carrier concentrations.

To assess polaronic properties, we compute the effective mass $m^*(k)$ using the relationship [180]

$$\frac{m^*(k)}{m} \approx 1 - \frac{\beta \Sigma''(k, \omega_n)}{\pi},$$

where m is the electron's bare mass in the non-interacting limit and $\Sigma(k, \omega_n) = \Sigma'(k, \omega_n) + i\Sigma''(k, \omega_n)$ is the complex-valued self-energy on the Matsubara frequency axis. (m also depends on k for our tight-binding model, so $\frac{m^*(k)}{m}$ should be understood including the k-dependence of both m^* and m.) To obtain the self-energy, we measure the unequal imaginary time Green's function $G_\sigma(k, \tau)$ which is then Fourier transformed to the Matsubara frequency axis $G_\sigma(k, \omega_m)$ using the discrete Lehmann representation [181]. To accomplish this task in practice, we use the `Lehmann.jl` package of the `libdlr` library [182]. The self-energy is then obtained by inverting Dyson's equation $G^{-1}(k, \omega_n) = i\omega_n - \xi_k - \Sigma(k, \omega_n)$.

We extract the value of the effective mass on the Fermi surface by linearly interpolating our DQMC data, as described in Chapter 2, Section 2.3.4 and illustrated in Fig. 4.2. First, we determine the location of the Fermi surface using the condition $\langle n_{k_F,\sigma} \rangle = 1 - G_\sigma(k_F, 0) = 0.5$, where $G_\sigma(k, 0)$ is the equal-time Green's function

(Fig 4.2a). We then interpolate the $\frac{m^*(k)}{m}$ data to obtain its value on the Fermi surface (Fig 4.2b).

Figure 4.3a explores how the superconducting correlations depend on λ. Here we fix $\beta = 16/t$, $\Omega = 4t$, and $\langle n \rangle = 0.7$, where we observed strong pairing tendencies across all three models without a corresponding competing order. The growth of the pairing correlations in the Holstein model is non-monotonic, with a maximum value occurring at $\lambda \approx 0.4$ before being rapidly suppressed at large λ by the formation of heavy bipolarons [38, 141]. This interpretation is supported by the behavior of the effective mass shown in Fig. 4.3b. Here, we plot the effective mass at the Fermi momentum along the $(0,0) - (0,\pi)$ cut through the first Brillouin zone, where we observe the strongest band renormalizations (see Fig. 4.2). In this case, the sharp drop in the pairing correlations coincides with a rapid increase in $m^*(k_\mathrm{F})/m$.

Turning to the SSH models, we find that the pairing correlations exhibit a milder dependence on λ in the strong coupling limit; in both the bond and optical models, $\chi_\mathrm{p}(\mathbf{q} = 0)$ initially grows rapidly at $\lambda \leq 0.2 - 0.3$ before leveling off to a constant value at larger couplings. At the same time, the effective mass for both models increases at a much slower rate in comparison to the Holstein model. This behavior demonstrates that the SSH (bi)polarons remain much lighter to stronger values of λ [46], even for the finite carrier concentration considered here.

Figs. 4.3(c),(d) shows analogous results for $\Omega = t/2$. In this case, the pairing correlations at weak λ for all three models are comparable to the non-interacting values. As λ increases, $\chi_\mathrm{p}(\mathbf{q} = 0)$ for the Holstein and optical-SSH models increase slightly before being rapidly suppressed with a concomitant rise in the effective mass, as in the antiadiabatic case. In contrast, the pairing correlations in the bSSH model are not suppressed at larger values of the *e*-ph coupling but are only slightly enhanced around $\lambda \approx 0.5$. The effective mass of the bond model remains small at all coupling values.

The strength of the pairing correlations at fixed temperature can be a poor proxy for the superconducting T_c that is ultimately realized in a system [183]. For example,

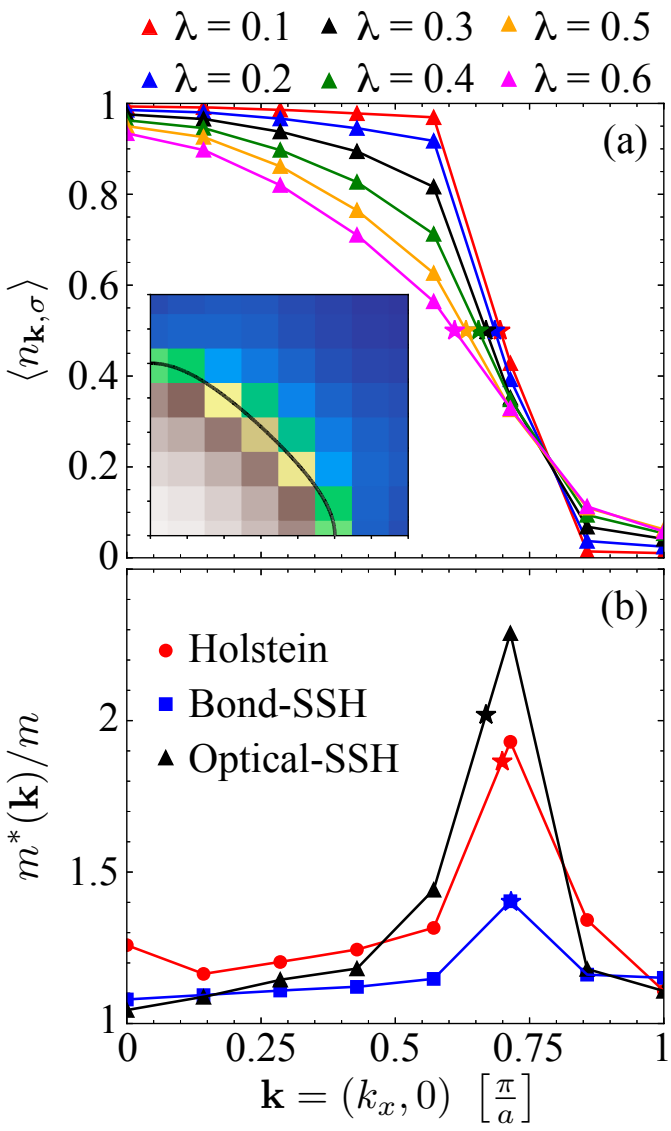

Figure 4.2: (a) The expectation value of the number operator $\langle n_{k,\sigma} \rangle$ for the optical-SSH model as a function of λ, plotted along the $k = (k_x, 0)$ direction of the first Brillouin zone (FBZ). The allowed momentum points in the cluster are indicated by the triangles. The Fermi momentum, indicated by the stars, is determined by $\langle n_{k,\sigma} \rangle = 1/2$ and estimated by linearly interpolating the DQMC data. The inset shows $\langle n_{k,\sigma} \rangle$ in the upper quadrant of the FBZ for $\lambda = 0.3$, where the solid black line indicates the location of the non-interacting Fermi surface. (b) The effective mass $m^*(k)/m$ along $(k_x, 0)$ for the Holstein (red ○), optical- (blue □), and bond-SSH (black △) models for $\lambda = 0.3$. The value of $m^*(k_F)/m$ (indicated by the stars) is estimated using linear interpolation. All data were obtained on $N = 14 \times 14$ clusters with $\beta = 16/t$ and $\Omega = 4t$.

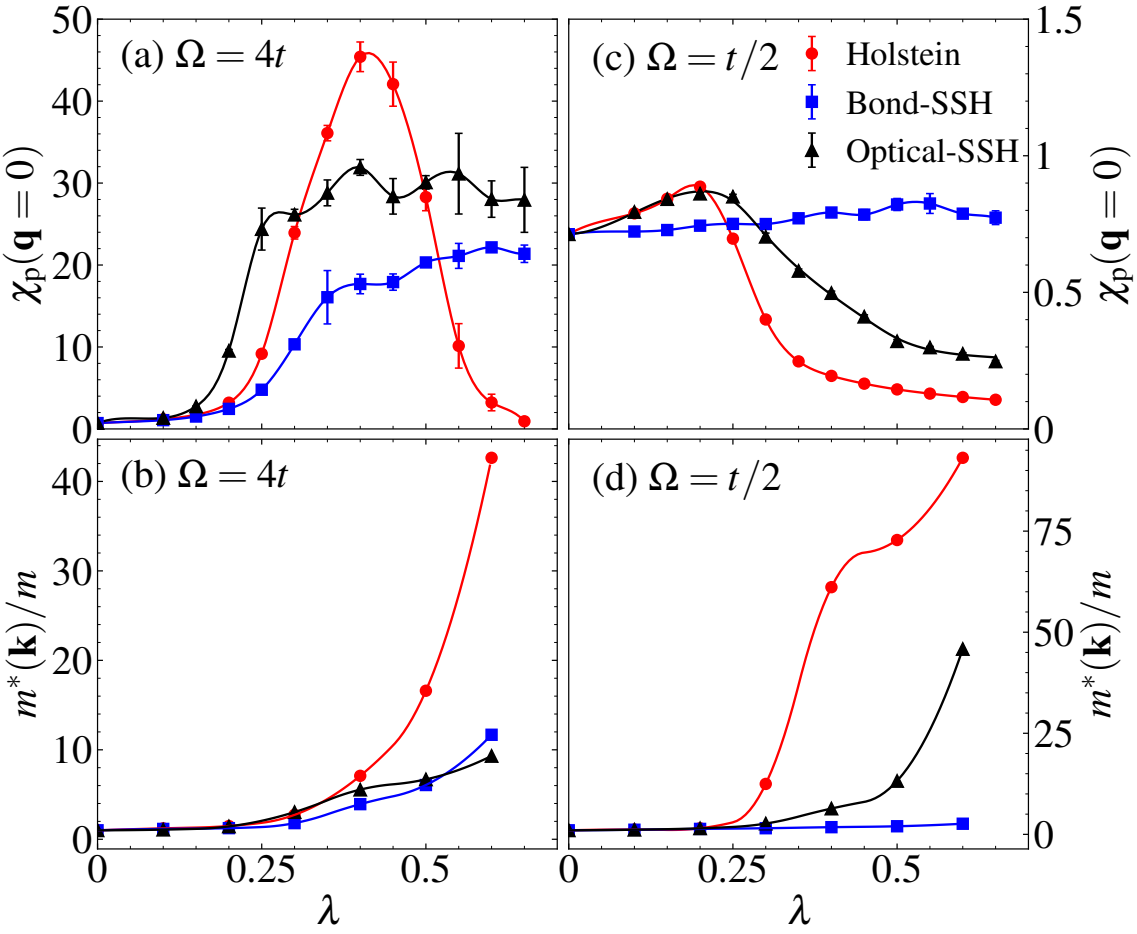

Figure 4.3: DQMC results for the Holstein (red ○), and bond-, (blue □), and optical- (black △) SSH models. The top row plots the s-wave pair-field susceptibility $\chi_p(q = 0)$ as a function of λ for (a) $\Omega = 4t$ and (c) $\Omega = t/2$. Panels (b) and (d) plot estimates of the effective mass $m^*(k)/m$ measured on the Fermi surface at $k = (k_F, 0)$. All results were obtained from $N = 14 \times 14$ lattices with $\beta = 16/t$ and $\langle n \rangle = 0.7$.

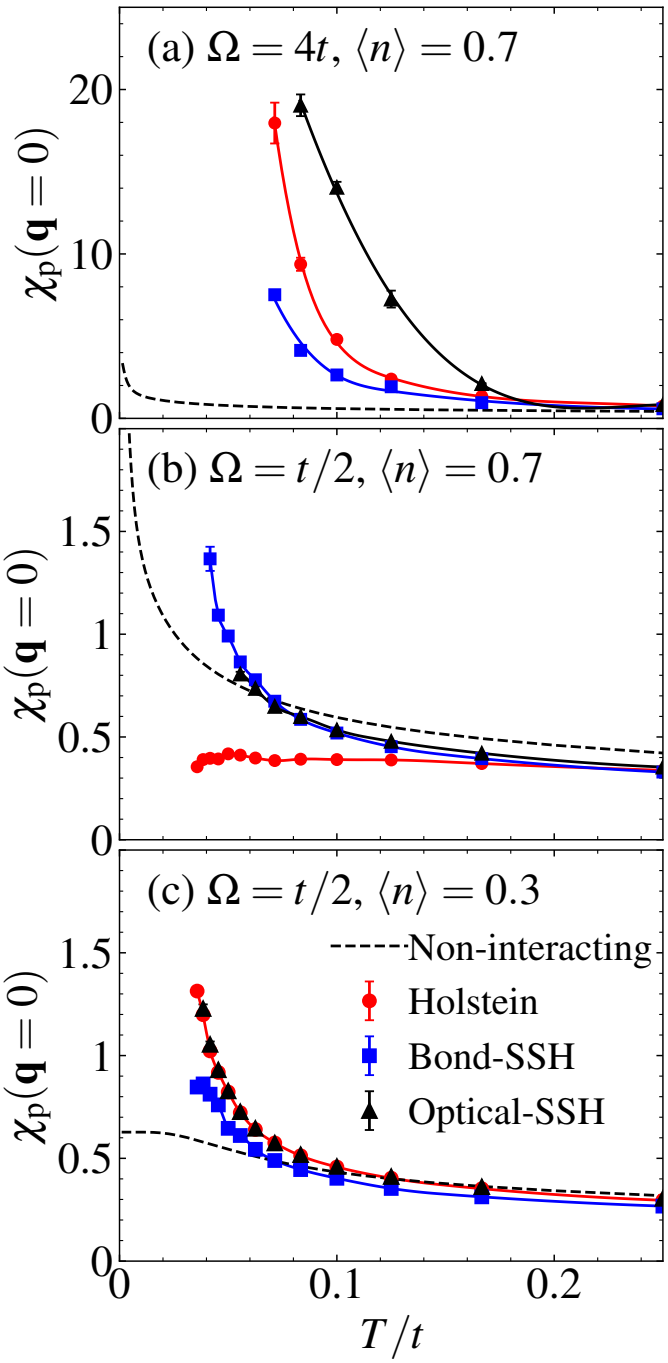

Figure 4.4: A comparison of the temperature dependence of the s-wave pair-field susceptibilities for the Holstein (red ○), and bond- (blue □), and oSSH (black △) models at fixed $\lambda = 0.3$ and $\langle n \rangle = 0.7$. Results are shown for (a) $\Omega = 4t$, $\langle n \rangle = 0.7$, (b) $\Omega = t/2$, $\langle n \rangle = 0.7$, and (c) $\Omega = t/2$, $\langle n \rangle = 0.3$. All results were obtained on an $N = 14 \times 14$ cluster. The solid lines are spline fits to the data and act as a guide to the eye. The dashed black lines are the pair-field susceptibility for the non-interacting model.

the growth of an initially subdominant pairing channel can sometimes overtake a dominant one as the system is cooled. For this reason, Fig. 4.4 compares $\chi_p(\mathbf{q} = 0)$ as a function of T for the three models, again at a fixed $\lambda = 0.3$. For $\Omega = 4t$ and $\langle n \rangle = 0.7$ (Fig. 4.4a), the oSSH model has the largest pairing correlations while the bSSH model has the smallest. However, the growth of $\chi_p(\mathbf{q} = 0)$ for the Holstein model appears to be outpacing the oSSH model. Taken at face value, this would suggest that the Holstein model has the highest T_c at this filling. However, finite size effects may slow the growth of the superconducting correlations in the optical model if the correlation length has become comparable to the cluster size. Regardless, the results in Fig. 4.4a indicate that the oSSH and Holstein models have comparable values of T_c for these parameters.

Fig. 4.4b shows results for $\Omega = t/2$ and $\langle n \rangle = 0.7$. Here, the pairing correlations for the Holstein model are significantly reduced as a function of temperature by the competing CDW correlations and local bipolaron formation [38, 141, 158]. Conversely, the pairing correlations in the optical- and bSSH models continue to grow as the temperature is lowered and ultimately become larger than the non-interacting values. Both SSH models have comparable $\chi_p(T)$ values as a function of temperature, implying they will have a similar T_c.

The behavior reported in Fig. 4.4b demonstrates that the SSH interactions are less prone to forming heavy bipolarons and can mediate superconductivity more effectively than the Holstein model in proximity to its competing CDW/BOW order. However, it is unclear if the transition temperature ultimately realized by the SSH models is larger than what could be achieved in the Holstein model if one could somehow suppress the competing CDW correlations. To address this question, Fig. 4.4c now examines $\chi_p(q = 0)$ versus T for the three models, this time focusing on $\Omega = t/2$ and $\langle n \rangle = 0.3$, far from any competing CDW correlations. In this case, the pairing correlations in all three models grow above the non-interacting value as the temperature is lowered. However, the strength of the pairing correlations for the Holstein and oSSH models are identical (within error bars), while the

correlations in the bSSH model are smaller. We can thus reasonably conclude that the superconducting T_c for the oSSH and Holstein models are comparable for these parameters, while T_c for the bSSH model is smaller.

Finally, we turn to the question of how robust the pairing correlations are against the inclusion of the *e*-*e* interaction. To this end, Fig. 4.5 plots the superconducting correlations in the bond- and optical-Hubbard-SSH models, where we have added a slight on-site Hubbard repulsion of $U = t/2$. Since the non-zero value of U induces a Fermion sign problem (see Appendix D), here we focus on results obtained on a smaller $N = 8 \times 8$ lattice with $\Omega = 4t$, $\lambda = 0.3$, and $\langle n \rangle = 0.5$, which corresponds to the filling with the strongest pairing correlations on this size lattice. For both the bond (Fig. 4.5a) and oSSH (Fig. 4.5b) models, we find that both onsite and extended *s*-wave pairing correlations decrease rapidly once a small Hubbard repulsion is included in the model.

4.3 Discussion

We have used DQMC to study and contrast the ordering tendencies of the 2D Holstein and bond-/oSSH models over a wide range of carrier concentrations. Our results reveal that these models produce different qualitative behaviors depending on the filling of the underlying band. Close to half-filling, the Holstein and optical SSH models are dominated by CDW and BOW order, respectively. The superconducting correlations were generally suppressed near these competing orders; however, the suppression was more severe for the Holstein model. Conversely, the bSSH model supported superconducting correlations up to half-filling, especially in the anti-adiabatic limit ($\Omega = 4t$). Variational calculations in the two-particle limit [46] have shown that the SSH (bi)polarons are lighter and more mobile than the Holstein bipolarons for a larger range of couplings. Our results demonstrate that this property persists to finite carrier concentrations and allows the SSH models to support superconductivity in regions of phase space where the polaronic effects prevent

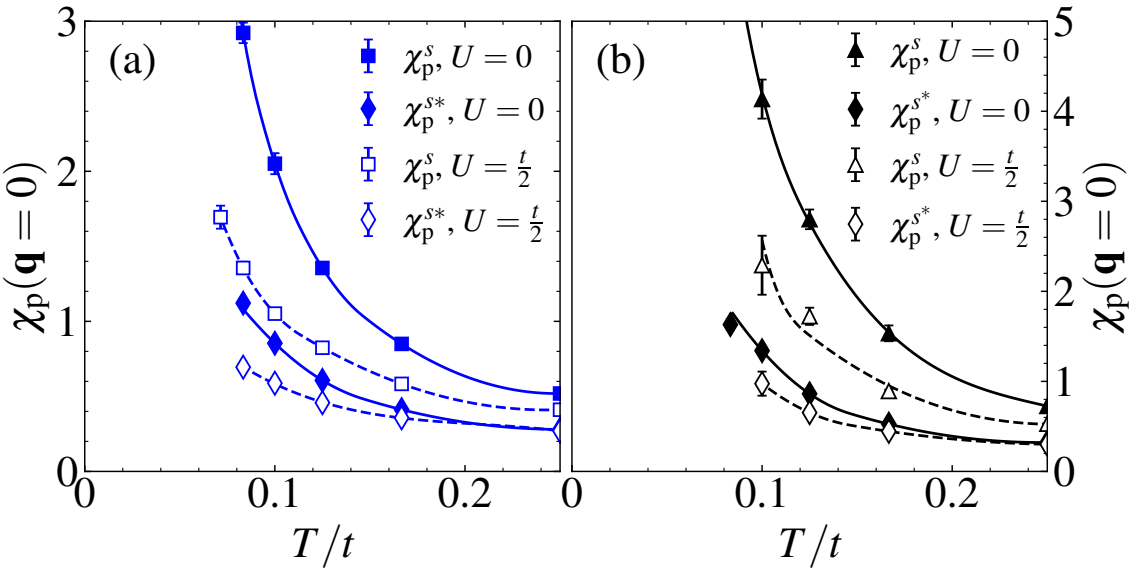

Figure 4.5: The temperature dependence of the uniform s-wave [$\chi_p^s(q=0)$, $\square$ points] and extended s-wave [$\chi_p^{s^*}(q=0)$, $\diamond$ points] pair-field susceptibilities for the (a) bond- and (b) oSSH models with a Hubbard $U=0$ and $t/2$. All results were obtained on an $N=8\times 8$ cluster due to the Fermion sign problem (see Appendix **??**) and fixed $\langle n\rangle = 0.5$, $\Omega = 4t$, and $\lambda = 0.3$.

pairing for the Holstein model. This result lends support to the hypothesis that SSH interactions can circumvent some factors that limit pairing in the conventional Holstein and Fröhlich models, at least in proximity to the competing BOW order.

At more dilute concentrations, where competition with CDW or BOW correlations is absent, we find that the pairing correlations for the optical and bSSH models are comparable to that of the Holstein model. This result suggests that the bond- and optical-SSH models will not produce significantly larger superconducting transition temperatures than that of the Holstein model, at least for carrier concentrations larger than $\langle n \rangle \geq 0.3$.

Another critical issue in studying SSH-like interactions is the potential role of the sign changes in the effective hopping integrals. The models considered here and elsewhere treat the nonlinear dependence of the hopping integrals on the bond distance using the linear approximation. This treatment allows the sign of the effective hopping integral to change as the atoms vibrate about their equilibrium positions, which can dramatically affect the ground and excited states of the model [162, 166]. Indeed, we have found that these sign changes frequently occur in our DQMC simulations when the dimensionless coupling λ or phonon energy Ω is large (see Appendix C). We have allowed these changes to occur in the current work since we were interested in studying the ordering tendencies in the linear SSH models as they are commonly formulated. However, future studies should explore how additional nonlinear e-ph interactions or anharmonic lattice potentials might alter the BOW and superconducting correlations observed here. Such terms have already been shown to substantially alter the physics of the Holstein model [140, 184–187].

CHAPTER 5:
ANTIFERROMAGNETIC AND BOND-ORDER-WAVE PHASES IN THE HALF-FILLED TWO-DIMENSIONAL OPTICAL SU-SCHRIEFFER-HEEGER-HUBBARD MODEL

Human intuition and instinct are not always right,
but they do make life interesting.

— Guinan, *Star Trek: The Next Generation*

This Chapter contains text from published first author work by the author [188] *with minor modifications where appropriate for this format. The author's contribution was doing all simulations with input from Benjamin Cohen-Stead, including collecting the data, performing the analysis, and producing the figures. The author wrote most of the manuscript with input from the coauthors.*

5.1 Introduction

Strongly correlated quantum materials are often governed by the interplay between two or more degrees of freedom, which compete or cooperate with one another to produce novel states of matter and complex phase diagrams [7, 189–191]. For example, many interesting phases can be derived from combining *e*-ph and electron-electron (*e*-*e*) interactions. A canonical model for this physics is the half-filled Hubbard-Holstein model, which hosts charge-density-wave, AFM, and intermediate metallic phases, with the latter depending on the dimensionality of the system [76, 130, 134, 171, 192–195]. There is also evidence suggesting that *e*-ph interactions can enhance *d*-wave pairing [135, 194, 196] and affect spin and charge correlations [92, 197] in doped Hubbard-Holstein models as seen in Chapter 3.

Recently, interest in *e*-ph interactions has shifted toward SSH models, where the atomic motion modulates the electronic hopping integrals [39, 159]. While

different variants of the SSH model have been introduced over the years, a widely studied one is the so-called bSSH model [62], which places independent harmonic oscillators on the bonds between atomic sites. QMC studies of the bSSH model have yielded interesting results regarding superconductivity [47, 198] and magnetism, including the presence of antiferromagnetism absent a Coulomb interaction [178, 199]. Subsequent work reported on the robustness of this anomalous antiferromagnetism and its competition with a BOW* phase, both with and without a Hubbard interaction [163, 176, 200]. A lesser studied variant is the oSSH model [60], which instead places dispersionless Einstein phonons on the atomic sites that simultaneously modulate all of the surrounding nearest-neighbor hopping integrals. As seen in Chapter 4, the two models produce quite different physical results [66, 145], which motivates studies into correlated oSSH models. This class of interactions has also been implicated in a wide range of quantum materials [33, 34, 41, 43, 45, 201].

This Chapter presents a detailed study of the low temperature phases of the oSSH-Hubbard model on a square lattice using numerically exact DQMC. Both the oSSH and bSSH couplings preserve particle-hole symmetry at half-filling such that the simulations remain sign-problem-free, unlike in the Hubbard-Holstein model [130]. Focusing on the adiabatic regime ($\Omega/E_{\mathrm{F}} \sim 1/8$) relevant to most materials, we obtain a low-temperature phase diagram with $Q = (\pi/a, \pi/a)$ AFM and BOW phases, depending on the relative strengths of the *e*-*e* and *e*-ph interactions. We also find evidence for a narrow region of coexistence between these phases. At $T = 0$, the AFM and BOW phases are insulating; however, we find a small region of metallically for small values of (λ, U) at finite temperatures but no indications of enhanced superconductivity in this region. Importantly, we also find no evidence for an AFM phase in the pure oSSH model ($U = 0$), in contrast to the bSSH model [178, 199]. Instead, we find only a weak enhancement of short-range AFM correlations in this

*We use BOW to denote the formation of dimers with a lattice deformation. This differs from a Valence Bond State (VBS) in which dimers form absent a lattice deformation.

region of parameter space. Our results highlight crucial differences between the two variants of the SSH model and how it competes with Mott correlations.

5.2 Results

Figure 5.1 plots the low-temperature phase diagram of the half-filled oSSH-Hubbard model in the λ-U plane. For small e-ph coupling, the system is dominated by AFM Mott/Slater correlations depending on the value of U/t. Increasing the e-ph coupling for fixed U/t drives the system into a non-magnetic insulating BOW phase, with a narrow intermediate regime of AFM/BOW coexistence, as indicated by the hatched shading. Additionally, in the $U/t = 0$ limit, the BOW ground state disappears below a critical coupling $\lambda_c^{\mathrm{BOW}} = 0.103 \pm 0.010$. Below this coupling, we observe a weak enhancement of the short-range AFM correlations in the pure oSSH model but no long-range AFM order. This result is in direct contrast with the bSSH model, where long-range magnetic order was reported [178, 199]. We can understand this result by considering the difference in the effective e-e interactions that arise in the anti-adiabatic limits of the two models, see Appendix E. We also estimate that for $\lambda < \lambda_c^{\mathrm{BOW}}$ and $U/t \lesssim 2$, the system is an AFM metal at elevated temperatures ($\beta \geq 16/t$, see Appendix F) before transitioning to an insulator at higher U/t or lower temperatures. In the following sections, we will discuss the various measurements that lead to this phase diagram.

The phase boundaries in Fig. 5.2 were obtained from the crossing point of the BOW and AFM correlation ratios, as illustrated in Fig. 5.2. Here we show the correlation ratio for BOW and AFM order in Figs 5.2a and 5.2b, respectively, for a representative value of $U/t = 3$. This analysis is based on a finite-size scaling analysis [89–91], where the quantum critical point (QCP) λ_c corresponds to the crossing point of the $R_\gamma(L)$ curves for different cluster sizes L while fixing $\beta t = L$;

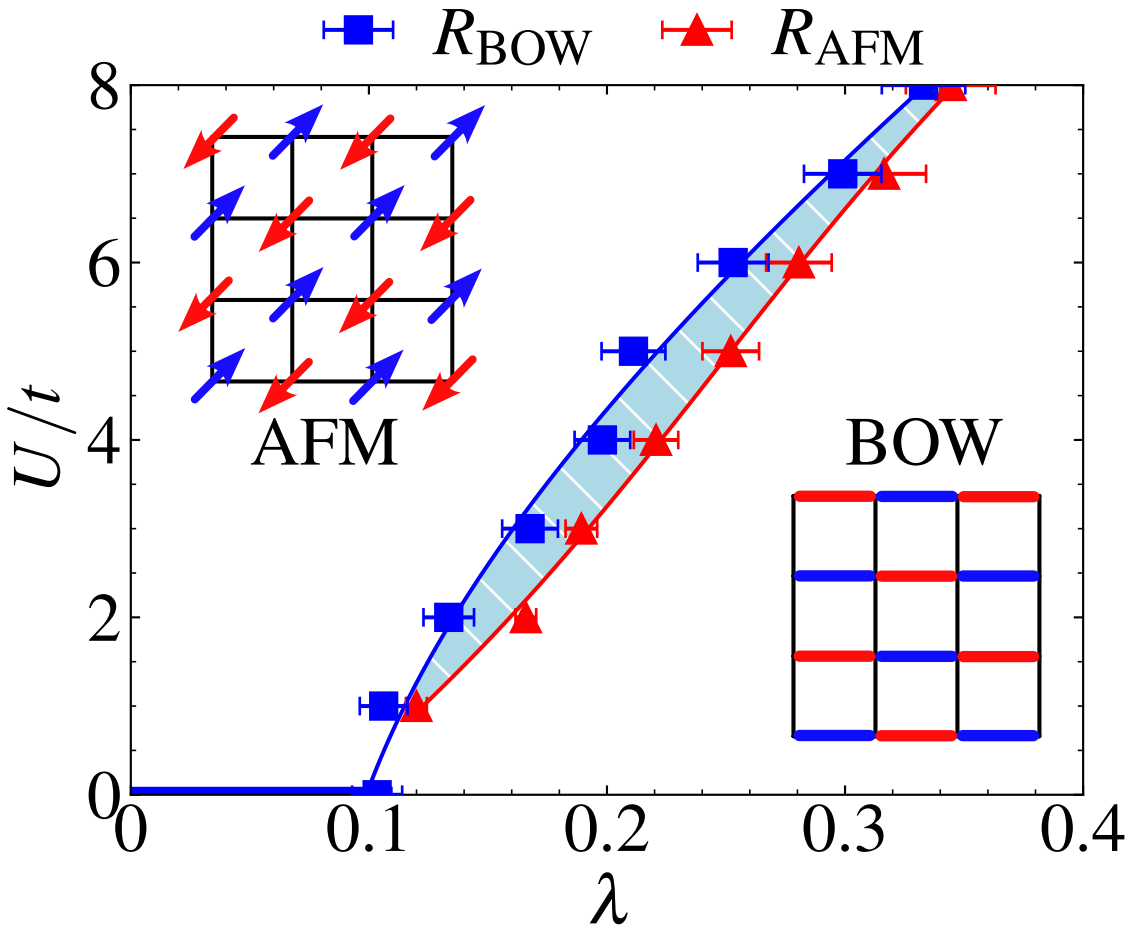

Figure 5.1: Phase diagram of the optical SSH-Hubbard model at half-filling $\langle n \rangle = 1$ with a fixed phonon frequency $\Omega/t = 0.5$. The red triangles and blue squares denote the transition points obtained from AFM and BOW correlation ratios, respectively, with solid lines providing a guide for the eye. The blue hatched area represents the region of AFM/BOW coexistence. The thick blue line from $\lambda = 0$ to λ_c along the $U = 0$ line denotes a region where the pure optical SSH model has no long-range AFM or BOW order. The insets sketch the relevant phases. In the BOW phase, the blue, red, and black lines indicate long, short, and undistorted bonds.

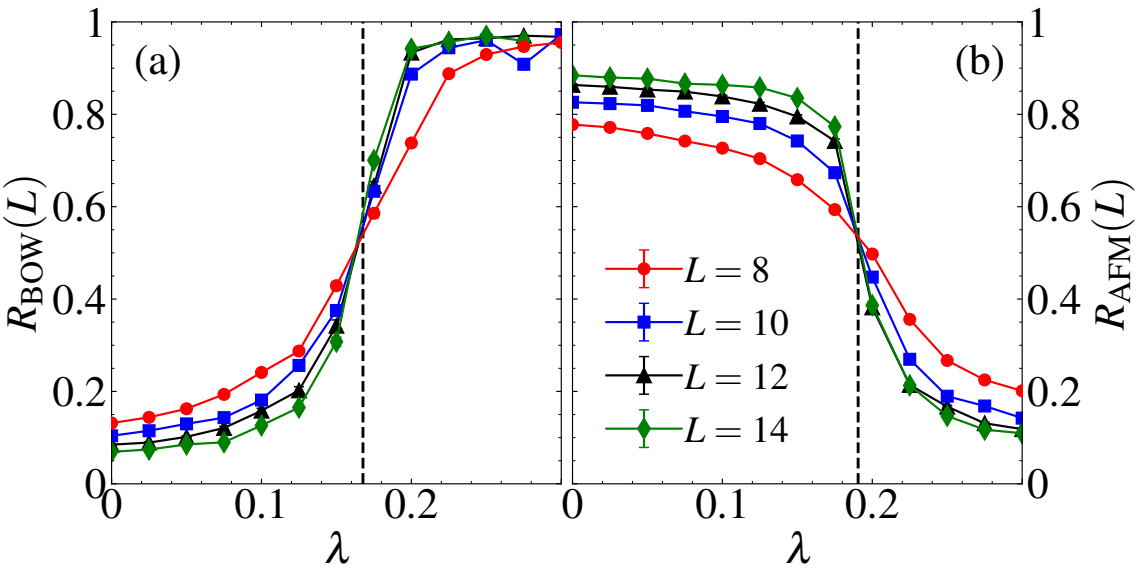

Figure 5.2: Correlation ratios for the (a) bond-ordered-wave and (b) antiferromagnetic phases as a function of λ for fixed $U/t = 3$. The location of the quantum critical point λ_c is obtained from the crossing of the correlation ratio for different lattice sizes L and is indicated by the dashed lines. All calculations were performed for fixed phonon frequency $\Omega/t = 0.5$ and at an inverse temperature $\beta t = L$. The definition of the correlation ratio is provided in the Methods section.

further details can be found in Chapter 2, Section 2.3.4. This approach assumes that the dynamical critical exponent for the AFM and BOW transitions is $z = 1$ [134, 202]. In this case, we obtain $\lambda_c^{\mathrm{BOW}} = 0.16 \pm 0.01$ (see Fig. 5.2a) and $\lambda_c^{\mathrm{AFM}} = 0.189 \pm 0.007$ (see Fig. 5.2b). The difference in these values suggests a narrow region of coexistence between the two states, where BOW order has begun to set in while AFM order has not yet disappeared. This result is distinct from that of the bSSH and bSSH-Hubbard models, in which a direct transition from a BOW to AFM ground state occurs, with no reported region of coexistence [163, 176, 178, 199]. The remaining points in Fig. 5.1 were obtained from a similar analysis, as shown in Appendix F.

Another key difference between our phase diagram and results obtained for the bSSH model pertains to the behavior along the $U/t = 0$ line. In the pure bSSH model, AFM order is stabilized without a Hubbard interaction [199]. Here, however, we observe no such order along the $U/t = 0$ line but instead only a weak enhancement of short-range AFM correlations, see Appednix F. This behavior is illustrated in Figs. 5.3a and 5.3b, which plot the BOW and AFM correlation ratios in this limit, respectively. While we obtain a finite critical coupling for the BOW phase from the corresponding correlation ratio crossing, we observe no similar crossing in AFM correlation ratio. Taking a larger $\Omega/t = 2$ produces similar results, as shown in Figs. 5.3c and 5.3d, with $\lambda_c = 0.130 \pm 0.004$ for the BOW transition and no crossing for the AFM correlation ratio. The similarity of the results in Figs. 5.3b and 5.3d suggest that the absence of AFM order is due to the nature of the oSSH coupling rather than the phonon energy.

The lack of AFM order in the oSSH model can be understood by considering the effective *e-e* interaction that arises in the anti-adiabatic limit. Previous studies showed that in this limit, the bSSH model gives rise to a Heisenberg-like nearest-neighbor coupling between the electron spins that favors AFM correlations [178, 199]. In Appendix F, we show that while the anti-adiabatic oSSH model retains this nearest-neighbor *e-e* interaction, it also introduces longer-range interactions of similar strength between electrons on the same sublattice F. These longer-range interactions

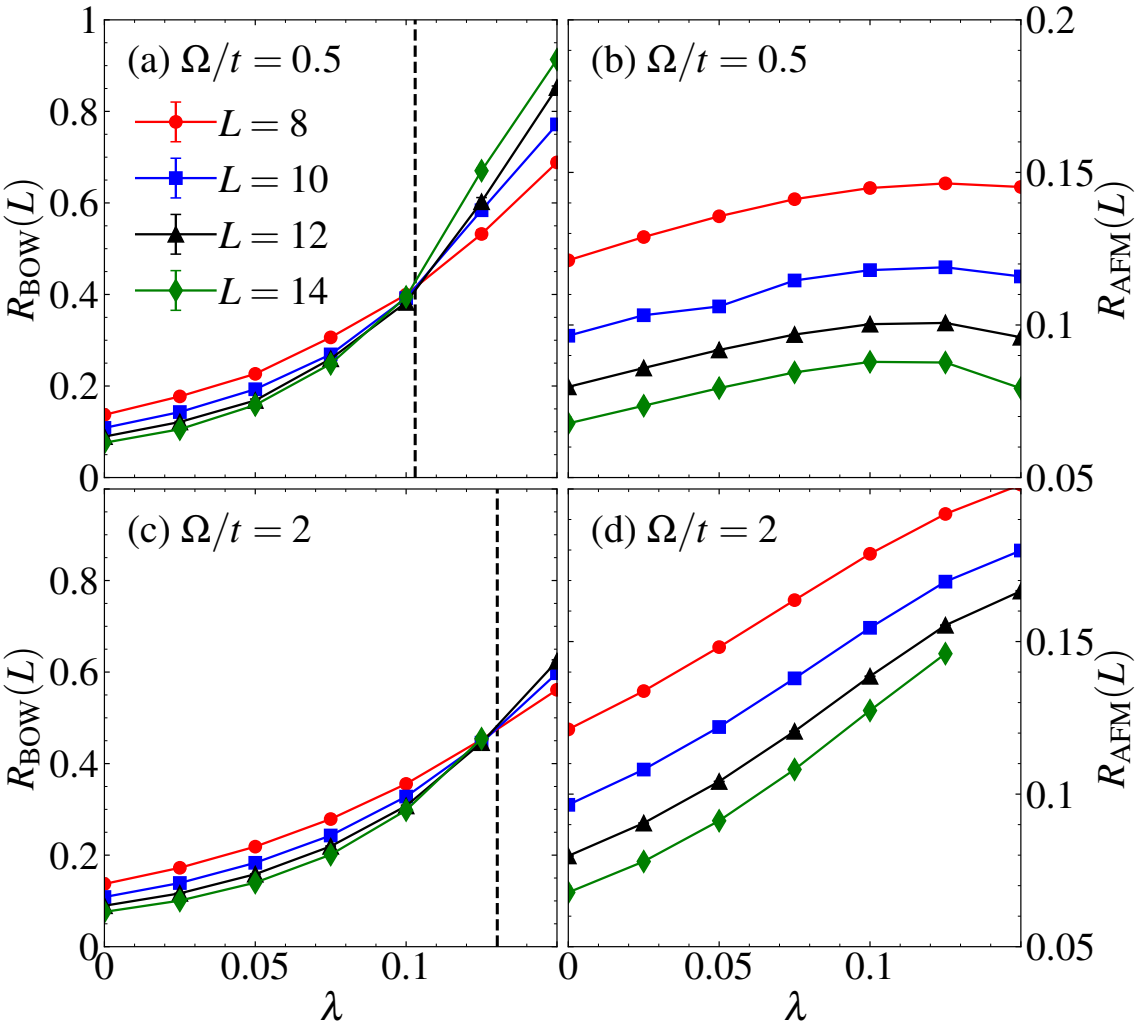

Figure 5.3: Correlation ratios for the bond-ordered-wave and antiferromagnetic orders as a function of λ for the pure oSSH model ($U/t = 0$) at $\Omega/t = 0.5$ [panels (a) and (b)] and $\Omega/t = 2$ [panels (c) and (d)]. The BOW data indicates there is a finite critical coupling $\lambda_c(\Omega/t = 0.5) = 0.103 \pm 0.010$ and $\lambda_c(\Omega/t = 2) = 0.130 \pm 0.004$, while no crossing point is observed for the AFM correlations. All calculations were performed at an inverse temperature $\beta t = L$.

frustrate any AFM correlations from occurring. Intuitively, this difference in the effective *e*-*e* interaction arises from the fact that each phonon mode in the oSSH model modulates two hopping integrals as opposed to just one, as in the bSSH model.

Our scaling analysis of the crossing ratio fixed $\beta = L$ to access low-temperature (ground state) properties. It is possible that our simulations are not reaching low enough temperatures to access the true ground state and that AFM does ultimately appear at lower temperatures. However, our results clearly show that if this is the case, the transition temperature is much lower in the oSSH model than in the bSSH model. This result is consistent with the presence of frustrating next-nearest neighbor interactions, as discussed in Appendix E. Ground state calculations would be valuable in this context.

To further examine the relevant transitions between AFM and BOW order and the possible coexistence region, we measured several local observables on $L = 8$ clusters at low temperature ($\beta t = 16$). Local observables are often sensitive to changes in the dominant correlations in the system while being less prone to finite size effects [77, 130, 134].

Figure 5.4a shows the average double occupancy $D = \langle n_{i,\uparrow} n_{i,\downarrow} \rangle$ as a function of λ for selected values of U/t. Mott correlations for weak couplings initially suppress the double occupancy, but it grows as the strength of the *e*-ph coupling increases. Notably, the D vs. λ curves have a kink at λ values that coincide with the transition from the AFM to BOW state, as indicated by the red line in Fig. 5.1. For larger values of λ, the values of the double occupancies begin growing toward their uncorrelated values, which reflects the increased hybridization between pairs of sites in the BOW phase.

The average values of the electron kinetic energy $\langle \hat{K}_\nu \rangle$ and the root mean square phonon displacement $(\langle \hat{X}_\nu^2 \rangle)^{1/2}$ are shown in Figs. 5.4b and 5.4c, respectively. Because the SSH interaction modulates the nearest-neighbor hopping integrals,

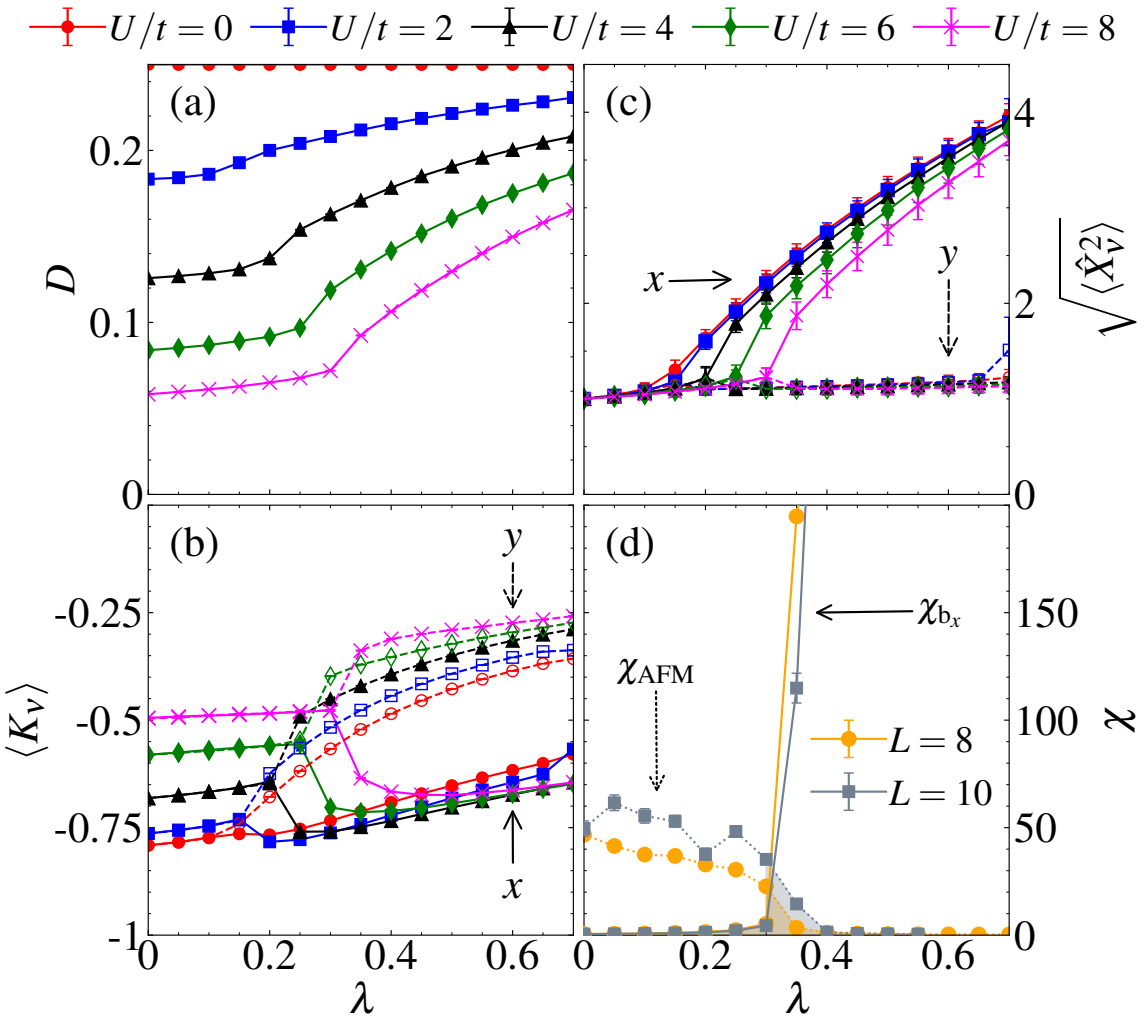

Figure 5.4: A summary of several local observables for the optical SSH-Hubbard model. (a) the average double occupancy D. (b) the average kinetic energy $\langle K_\nu \rangle$ in the $\hat{x}$ (solid lines) and $\hat{y}$ (dashed lines) directions. (c) the root mean square of the average displacement $(\langle \hat{X}_\nu^2 \rangle)^{1/2}$ in the $\hat{x}$ and $\hat{y}$- directions. (d) a comparison of the AFM (dotted lines) and x-direction BOW (solid lines) susceptibilities for fixed $U/t = 8$ at $L = 8$ (orange circles) and $L = 10$ (gray squares). The shaded area indicates the region of AFM/BOW coexistence. All results were obtained for $\Omega/t = 0.5$, $\beta t = 16$, and $\langle n \rangle = 1$. The results in panels a-c were obtained on $L = 8$ clusters.

both quantities indicate how strongly the lattice distorts across parameter space. We observe a bifurcation in both quantities at coupling values that approximately coincide with BOW transition line shown in Fig. 5.1. The average electron kinetic energy and root mean square phonon displacement measured along each crystallographic direction are equal in the AFM phase but split in the BOW phase. This bifurcation is also observed in bSSH models [145, 199, 203] and reflects the broken C_4 symmetry of the BOW phase, sketched in the right inset of Fig. 5.1.

Finally, Fig. 5.4d examines the AFM and BOW susceptibilities for $U/t = 8$ and $L = 8$ and 10 clusters. Here, we observe a small region where both susceptibilities have large non-zero values, as indicated by the shaded area. This behavior is consistent with coexistence between the AFM and BOW phases.

Next, we examine the temperature dependence of the AFM, BOW, and pairing susceptibilities χ_γ in different regions of the phase diagram. Fig. 5.5 plots the results on a log scale for $\lambda = 0.16, 0.22$, and 0.28 as a function of βt and fixed $U/t = 4.5$. These results were obtained on a larger $L = 14$ cluster. For $\lambda = 0.16$, we expect the system to be antiferromagnetic, which is corroborated by the dominant $\chi_{\mathrm{s}}(\pi, \pi)$ at low-temperatures shown in Fig. 5.5a. Similarly, for $\lambda = 0.28$, we expect the system to be in a BOW phase, which is consistent with the dominant $\chi_{\mathrm{b}}(\pi, \pi)$ shown in Fig. 5.5c. More interesting is the $\lambda = 0.22$ case, which lies within the coexistence region. In this case, the AFM and BOW susceptibilities are of the same order of magnitude and grow concomitantly with decreasing temperature.

It has recently been shown that bSSH-like interactions can mediate strong binding between carriers in the dilute limit [46] and potential high-temperature superconductivity, provided that it is not preempted by the formation of any competing order [47, 198]. The black triangles in Figs. 5.5a-c plot the on-site s-wave pairing susceptibility as a function of temperature and give no indication of a superconducting instability. Fig 5.5d also plots the temperature dependence of the extended s-wave and d-wave susceptibilities for the three regions identified in the

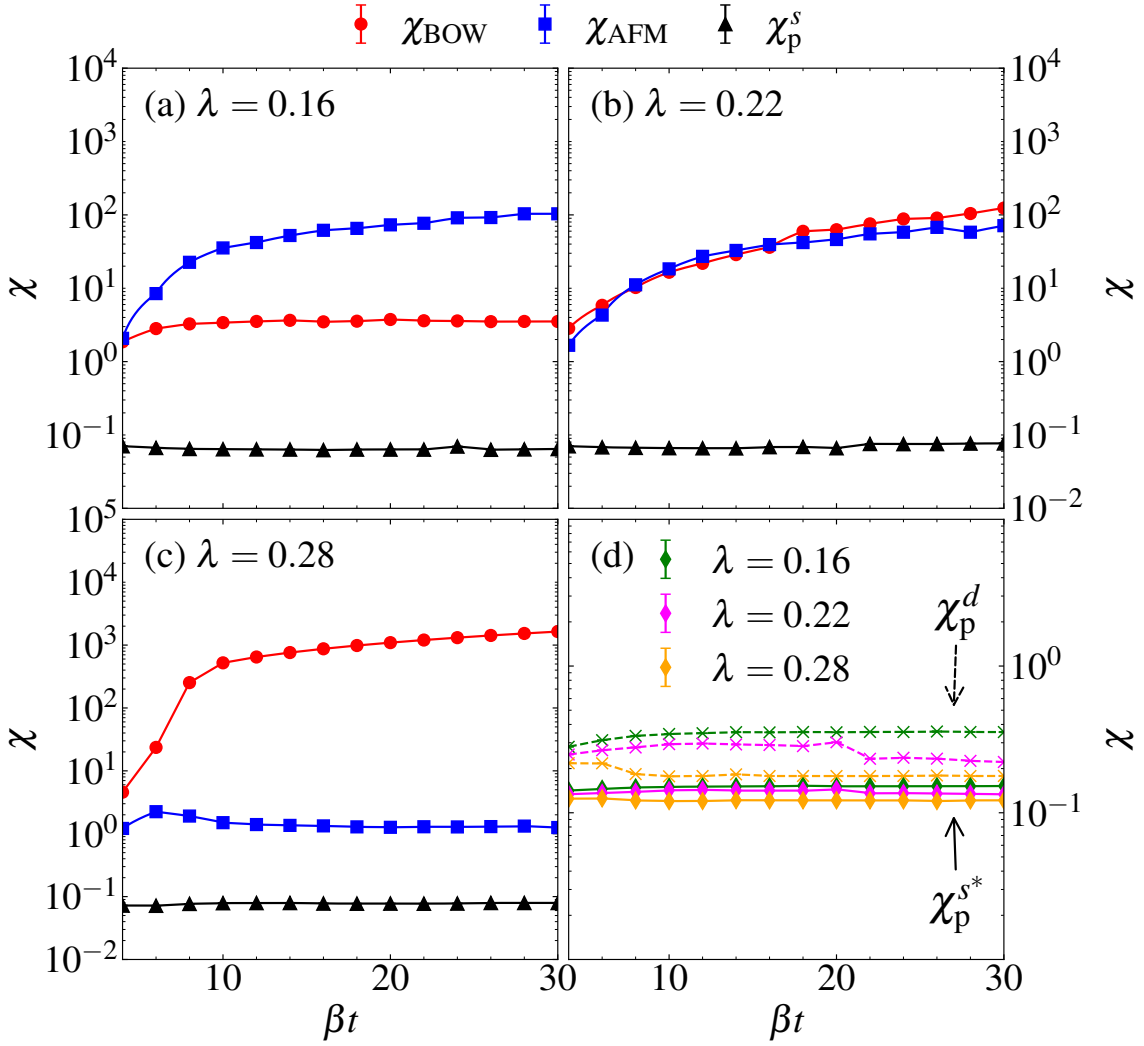

Figure 5.5: Finite temperature susceptibilities in different regions of the phase diagram. Panels (a), (b), and (c) show AFM (blue squares), BOW (red circles), and on-site s-wave pairing (black triangles) susceptibilities at $\lambda = 0.16$, 0.22, and 0.28, respectively. Panel (d) plots the corresponding extended s- (χ_{p}^{s*}, solid lines) and d-wave (χ_{p}^{d}, dashed lines) susceptibilities. Lines are a guide to the eye. All results were obtained from $L = 14$ lattices with fixed $U/t = 4.5$, $\Omega = t/2$, and $\langle n \rangle = 1$.

phase diagram. Here we find no indications of robust s-wave, extended s-wave, or d-wave pairing. While the d-wave susceptibility is the dominant pairing channel for all values of λ we have checked, its magnitude is several orders of magnitude smaller than either the AFM or BOW susceptibilities at low temperatures.

The AFM phase found at small U/t and λ is metallic at $\beta = 16/t$. We have found that insulating behavior sets in upon further cooling, and we have observed no indications of low-temperature superconducting correlations in this region of the phase diagram either. These results provide strong numerical evidence that the AFM or BOW phases are dominant at half-filling across the entire (λ, U)-plane as might be expected for such a commensurate filling. It remains to be seen whether doping the system, which will introduce a sign problem, will induce superconductivity; however, we also note that a recent study of the pure doped oSSH model, which does not have a sign problem, found no indication of high-temperature superconductivity for these parameters [145].

5.3 Discussion

We have conducted a detailed DQMC study of the magnetic and bond-ordered phases of the half-filled oSSH-Hubbard model in the (λ, U)-plane, focusing on the challenging adiabatic regime relevant to most materials. For weak e-ph coupling, the system is dominated by AFM Mott correlations similar to those observed in the single-band Hubbard model. Increasing the e-ph coupling strength above a non-zero U-dependent critical value λ_c^{BOW} induces a BOW phase. Additionally, while there is no sign of enhanced superconducting correlations anywhere in the phase diagram, we did find evidence for a narrow region of coexistence between the AFM and BOW phases. Finally, in the $U = 0$ limit, we did not detect any long-range AFM phase in the pure oSSH model. We did, however, observe a weak enhancement of AFM correlations in this regime, indicating that such correlations are short-ranged

at the temperatures we accessed (see Appendix F). In this context, we note that any sign-problem-free-model is expect to have a low-temperature instability away from a Fermi-liquid ground state [204]. Thus we expect either superconductivity, antiferromagnetism, or non-Fermi-liquid behavior at zero temperature. However, which instability ultimately occurs currently cannot be assessed from our results.

Previous DQMC studies of the bSSH-Hubbard model have also observed a transition between AFM and BOW phases [163, 176]. These studies focused on higher energy phonon modes ($\Omega = 3t/2$ in Ref. [176] and $\Omega = t$ in Ref. [163]) and considered a model where each hopping integral is modulated independently, unlike in our model. Neither study reported any evidence for a region of coexistence between the two orders. We believe this difference stems from the nature of the microscopic coupling [66, 145]. For example, in the anti-adiabatic limit, the bSSH model can generate AFM order through an effective nearest-neighbor Heisenberg-like interaction [199]. In contrast, the oSSH model introduces additional longer-range interaction terms which frustrate the AFM order (see Appendix F). The combination of both an effective nearest-neighbor Heisenberg-like interaction and longer-range frustrating interactions would also explain the presence of enhanced short-range AFM correlations but the absence of long-range AFM order. The bSSH model also has a non-zero coupling to the $q = 0$ modes, which is forbidden in the case of the oSSH model [66]. The mobility of the oSSH polarons also appears to be much smaller than those of the bSSH model [145].

Understanding the interplay of e-ph and Coulomb interactions has implications for the study of many strongly correlated materials. While both the Hubbard-Holstein and the bSSH-Hubbard models have been explored numerically, the oSSH model has received comparatively less attention. With newer state-of-the-art numerical methods, we have successfully mapped out the principal phases of the half-filled oSSH-Hubbard model. In the future, it would be interesting to dope the system and study the differences in the superconducting correlations obtained from either the parent AFM or BOW phases. Finally, we note that both the

BOW and AFM phases can be detected experimentally using conventional scattering probes like inelastic neutron [205] or resonant inelastic x-ray scattering (RIXS) [206]; however, RIXS could be uniquely suited to probe the predicted coexistence region due coupling of spin and lattice degrees of freedom expected in this regime [207].

CHAPTER 6:
CONCLUSIONS

It's the unknown that defines our existence. We are constantly searching, not just for answers to our questions, but for new questions.

— Capt. Benjamin Sisko, *Star Trek: Deep Space Nine*

In this dissertation, we explored the effect of electron-phonon interactions on strongly correlated systems. Although the Hubbard model is considered to be the "standard model" of strong correlations, there has been a search for ingredient/ingredients that move it towards being a more complete description of microscopic behavior of materials like the high-T_c cuprates. To address this gap in knowledge, we employed two complimentary approaches to aid in our explorations:

1. **Variational Monte Carlo**, allowing for probes of the ground state, namely the ground state energy and order parameters.

2. **Determinant quantum Monte Carlo**, allowing for probes of finite temperature behavior, namely susceptibilities, phase transitions, and (bi)polaronic properties.

In Chapter 3, we used the combined efforts of VMC and DQMC to obtain a picture of what happens when charge and spin stripe correlations are subject to a Holstein-type electron-phonon interaction. Leveraging both of these methods simultaneously allowed us to probe both static and fluctuating stripe correlations.

We found numerical evidence that a Holstein interaction affect d-wave correlations when added to the Hubbard model; namely, through modification of the competing stripe phases. High energy phonons will tend to suppress both charge and spin stripes, whereas low-energy phonons can enhance them by increasing charge modulations. Our findings provide a possible explanation for anomalous oxygen isotope effects and provide a potential solution as to why charge modulations

tend to develop before spin modulations. Our overall conclusion is that e-ph coupling cannot be neglected for any complete picture of stripe physics.

Motivated by our findings involving the Holstein model, Chapter 4 completed the first broad comparison of pairing correlations in the Holstein, bond-, and optical-SSH models. In contrast to the Holstein bond-buckling modes, the SSH models' phonon modes provide a more realistic model in the context of the cuprate oxygen breathing modes.

While half-filling is dominated by CDW and BOW order in the oSSH and Holstein models, the bSSH supported superconductivity up to half-filling. Our calculations support the theory that SSH (bi)polarons are lighter than the Holstein (bi)polaron, leading to superconductivity existing in regions of phase space that would be otherwise suppressed in the Holstein model. In the dilute limit however, bSSH and oSSH pairing correlations were not significantly higher than those of Holstein. Crucially, we investigated the effect sign changes of the effective hopping integral. Unlike previous works, our studies allowed for this to occur in the linear approximation and we observed the sign changed frequently in our simulations as the dimensionless coupling λ or phonon energy Ω became large.

Equipped with these calculations, we then proceeded to map out the ground state phase diagram of the Hubbard-(optical) SSH model at half-filling in Chapter 5. We focused on the challenging adiabatic regime and observed AFM Mott correlations for weak e-ph coupling. Above a critical value of the dimensionless e-ph coupling and non-zero U, a BOW phase was induced. We did not observe any enhanced superconducting correlations anywhere in the phase diagram; instead, a narrow region of AFM/BOW coexistence was found. Most interestingly for the limit of $U = 0$ (a pure oSSH model), no long range AFM phase was detected in our calculations. It should be noted that other work by Cai et al. [176, 199] suggests that there is indeed AFM order in the pure bSSH model that we were unable to detect in our studies of the oSSH model.

6.1 Open Problems and Future Work

This section provides ideas for future explorations, extending some of the ideas presented in this dissertation. Specifically, we focus on further advancing our understanding of SSH models from various perspectives.

6.1.1 Stripes in the Hubbard-SSH model

Recent developments in parameterizing the variational wavefunctions for SSH interactions [208, 209] has paved the way for further work on the SSH model. These studies provide important insight into successful implementations of the wavefunction. The intuitive route is to use a Jastrow-Slater ansatz with backflow correlations [69]; that is, the orbitals are dependent on the position of the electrons. An improvement upon this method is by constructing an auxiliary Hamiltonian that explicitly depends on phonon coordinates, which itself is a form of "backflow"; however, the number of variational parameters is significantly reduced. This a promising route, as VMC nominally scales as $O(N^3)$ (for system size N), and a reduction of optimized parameters while maintaining physical properties is advantageous.

Additionally, Piccioni et al. [209] found that the exclusion of the *e*-ph Jastrow factor for an SSH model did not significantly reduce the accuracy of captured correlations. Motivated by these breakthroughs, an interesting calculation would be similar to our work on stripe correlations in the Hubbard-Holstein model. We already know to what extent that the two variants of the SSH model differ from the Holstein model. Therefore, it would be worthwhile to investigate stripe correlations in the Hubbard-SSH model, specifically the optical SSH model. While we have seen that the Holstein interaction can enhance charge correlations, what the SSH model does to these correlations is unexplored.

Another relatively unexplored aspect is the nature of the superconductivity that is competing with the stripe. The pairing symmetry in the cuprates is known to be

d-wave; however, there has been recent evidence [210] for pair-density-wave (PDW) order with local *d*-wave symmetry. How these finite momentum pairing states affect the stripe is an additional interesting problem.

The `VariationalMC.jl` package

Our previous DQMC calculations were possible due to the flexible nature of the `SmoQyDQMC` package [86]; namely, its ability to simulate various tight-binding models and interactions. To achieve the same level of generality but for VMC, we introduce the `VariationalMC` package [211]. It is a Julia implementation of the variational Monte Carlo algorithm capable of running a wide variety of tight-binding Hamiltonians with on-site and extended Hubbard interactions and/or electron-phonon interactions (full support for the Holstein and (optical) SSH models will be active in `v.1.1.0`). Similar to `SmoQyDQMC`, these Hamiltonians can be defined on arbitrary lattice geometries.

Crucially, `VariationalMC` is flexible in terms of the Jastrow-Slater wavefunction that can be defined. The definition of the Jastrow factor has been generically implemented to treat generic particle pairs that are subject to the pseudopotentials. Further, the Slater wavefunction supports the addition of a number of order parameters, including momentum-dependent pairing. Because of the modular nature of the simulation setup, the input wavefunction could also use a neural network (with the proper interface), or we could swap the standard Stochastic Reconfiguration derivatives with Automatic Differentiation.

6.1.2 The relative importance of anharmonic terms

The hopping integrals in the SSH model can have a nonlinear component

$$t(\hat{X}) \sim t_0 + \alpha_1 \hat{X} + \alpha_2 \hat{X}^2 + \cdots, \tag{6.1}$$

which we only treated to linear approximation in our calculations. This is a common method in the exploration of these types of interactions, but at a cost. As previously mentioned, the sign of the hopping integral would change frequently in our DQMC calculations with increasing λ and/or Ω. This does indeed have implications on the ground and excited states observed [162, 163]. The effects of re-addition of anharmonic terms have already seen in the Holstein model [140, 184–187]. Therefore, it would be of best interest that SSH calculations going forward should include anharmonic terms. This could include a re-examination of the BOW and superconducting correlations in the bond and optical models.

6.2 Final Remarks

We hope that the explorations in this dissertation provide further context in the landscape of quantum materials through models of strong correlations. We have demonstrated that the addition of electron-phonon interactions to the Hubbard model can have appreciable effects on the ground state. Stripe correlations, superconductivity, and other magnetic states are modified by interactions with the lattice, which allows one or the others to prevail as the leading order. Perhaps the central message of this dissertation is that there are always possibilities for renewal; that is, the revisiting of a prior problem with a new perspective. The Hubbard model has so far, stood the test of time as the standard model for strong correlations; however, as demonstrated by the over sixty years of work after its inception, it is far from the complete picture. The high-T_c cuprates are but a single problem, there are plenty of other materials which will have ongoing explorations in other forms, systems with multi-orbitals, for instance. Nickelates and Pnictides are more recent arrivals to the scene, and have already shown us that there are still many sectors to explore before we can consider this frontier to be fully mapped. It is up to us physicists to continue the charge of exploration.

BIBLIOGRAPHY

[1] Dirk van Delft and Peter Kes. The discovery of superconductivity. *Physics Today*, pages 38–43, 09 2010.

[2] Michael Tinkham. *Introduction to Superconductivity*. Dover Publications, 2004.

[3] J. Bardeen, L. N. Cooper, and J. R. Schrieffer. Microscopic Theory of Superconductivity. *Phys. Rev.*, 106:162–164, Apr 1957.

[4] Lev Gor'kov. Microscopic derivation of the Ginzburg-Landau equations in the theory of superconductivity. *Soviet Physics JETP*, 36(9):1364–1367, Dec 1959.

[5] J. G. Bednorz and K. A. Müller. Possible high t_c superconductivity in the ba−la−cu−o system. *Zeitschrift für Physik B Condensed Matter*, 64(2):189–193, 1986.

[6] M. K. Wu, J. R. Ashburn, C. J. Torng, P. H. Hor, R. L. Meng, L. Gao, Z. J. Huang, Y. Q. Wang, and C. W. Chu. Superconductivity at 93 k in a new mixed-phase y-ba-cu-o compound system at ambient pressure. *Phys. Rev. Lett.*, 58:908–910, Mar 1987.

[7] Eduardo Fradkin, Steven A. Kivelson, and John M. Tranquada. Colloquium: Theory of intertwined orders in high temperature superconductors. *Rev. Mod. Phys.*, 87:457–482, May 2015.

[8] J. M. Tranquada, B. J. Sternlieb, J. D. Axe, Y. Nakamura, and S. Uchida. Evidence for stripe correlations of spins and holes in copper oxide superconductors. *Nature*, 375(6532):561–563, 1995.

[9] M. Fujita, H. Goka, K. Yamada, J. M. Tranquada, and L. P. Regnault. Stripe order, depinning, and fluctuations in $la_{1.875}ba_{0.125}cuo_4$ and $la_{1.875}ba_{0.075}sr_{0.050}cuo_4$. *Phys. Rev. B*, 70:104517, Sep 2004.

[10] P. Abbamonte, A. Rusydi, S. Smadici, G. D. Gu, G. A. Sawatzky, and D. L. Feng. Spatially modulated 'mottness' in $La_{2-x}Ba_xCuO_4$. *Nature Physics*, 1(3):155–158, 2005.

[11] H.-H. Klauss, W. Wagener, M. Hillberg, W. Kopmann, H. Walf, F. J. Litterst, M. Hücker, and B. Büchner. From antiferromagnetic order to static magnetic stripes: The phase diagram of $(La, Eu)_{2-x}sr_xcuo_4$. *Phys. Rev. Lett.*, 85:4590–4593, Nov 2000.

[12] J. Hubbard. Electron Correlations in Narrow Energy Bands. *Proceedings of the Royal Society of London Series A*, 276(1365):238–257, November 1963.

[13] Bo-Xiao Zheng, Chia-Min Chung, Philippe Corboz, Georg Ehlers, Ming-Pu Qin, Reinhard M. Noack, Hao Shi, Steven R. White, Shiwei Zhang, and Garnet Kin-Lic Chan. Stripe order in the underdoped region of the two-dimensional Hubbard model. *Science*, 358(6367):1155–1160, 2017.

[14] Kota Ido, Takahiro Ohgoe, and Masatoshi Imada. Competition among various charge-inhomogeneous states and *d*-wave superconducting state in Hubbard models on square lattices. *Phys. Rev. B*, 97:045138, Jan 2018.

[15] Hong-Chen Jiang and Thomas P. Devereaux. Superconductivity in the doped Hubbard model and its interplay with next-nearest hopping t'. *Science*, 365(6460):1424–1428, 2019.

[16] Sandro Sorella. The phase diagram of the hubbard model by variational auxiliary field quantum monte carlo, 2022.

[17] Hao Xu, Hao Shi, Ettore Vitali, Mingpu Qin, and Shiwei Zhang. Stripes and spin-density waves in the doped two-dimensional Hubbard model: Ground state phase diagram. *Phys. Rev. Research*, 4:013239, Mar 2022.

[18] J. M. Tranquada. Cuprate superconductors as viewed through a striped lens. *Advances in Physics*, 69(4):437–509, 2020.

[19] Yi-Fan Jiang, Jan Zaanen, Thomas P. Devereaux, and Hong-Chen Jiang. Ground state phase diagram of the doped hubbard model on the four-leg cylinder. *Phys. Rev. Res.*, 2:033073, Jul 2020.

[20] D. J. Scalapino. A common thread: The pairing interaction for unconventional superconductors. *Rev. Mod. Phys.*, 84:1383–1417, Oct 2012.

[21] Daniel P. Arovas, Erez Berg, Steven A. Kivelson, and Srinivas Raghu. The hubbard model. *Annual Review of Condensed Matter Physics*, 13(1):239–274, 2022.

[22] Mingpu Qin, Thomas Schäfer, Sabine Andergassen, Philippe Corboz, and Emanuel Gull. The hubbard model: A computational perspective. *Annual Review of Condensed Matter Physics*, 13(1):275–302, 2022.

[23] Chia-Min Chung, Mingpu Qin, Shiwei Zhang, Ulrich Schollwöck, and Steven R. White. Plaquette versus ordinary d-wave pairing in the $t^{'}$-hubbard model on a width-4 cylinder. *Phys. Rev. B*, 102:041106, Jul 2020.

[24] C. C. Tsuei and J. R. Kirtley. Pairing symmetry in cuprate superconductors. *Rev. Mod. Phys.*, 72:969–1016, Oct 2000.

[25] Shengtao Jiang, Douglas J. Scalapino, and Steven R. White. Ground-state phase diagram of the $t - t' - J$ model. *Proceedings of the National Academy of Sciences*, 118(44):e2109978118, 2021.

[26] A. Lanzara, P. V. Bogdanov, X. J. Zhou, S. A. Kellar, D. L. Feng, E. D. Lu, T. Yoshida, H. Eisaki, A. Fujimori, K. Kishio, J. I. Shimoyama, T. Noda, S. Uchida, Z. Hussain, and Z. X. Shen. Evidence for ubiquitous strong electron–phonon coupling in high-temperature superconductors. *Nature*, 412(6846):510–514, 2001.

[27] S. Johnston, I. M. Vishik, W. S. Lee, F. Schmitt, S. Uchida, K. Fujita, S. Ishida, N. Nagaosa, Z. X. Shen, and T. P. Devereaux. Evidence for the

importance of extended coulomb interactions and forward scattering in cuprate superconductors. *Phys. Rev. Lett.*, 108:166404, Apr 2012.

[28] Lucio Braicovich, Matteo Rossi, Roberto Fumagalli, Yingying Peng, Yan Wang, Riccardo Arpaia, Davide Betto, Gabriella M. De Luca, Daniele Di Castro, Kurt Kummer, Marco Moretti Sala, Mattia Pagetti, Giuseppe Balestrino, Nicholas B. Brookes, Marco Salluzzo, Steven Johnston, Jeroen van den Brink, and Giacomo Ghiringhelli. Determining the electron-phonon coupling in superconducting cuprates by resonant inelastic x-ray scattering: Methods and results on $nd_{1+x}ba_{2-x}cu_3o_{7-\delta}$. *Phys. Rev. Res.*, 2:023231, May 2020.

[29] Yingying Peng, Leonardo Martinelli, Qizhi Li, Matteo Rossi, Matteo Mitrano, Riccardo Arpaia, Marco Moretti Sala, Qiang Gao, Xuefei Guo, Gabriella Maria De Luca, Andrew Walters, Abhishek Nag, Andi Barbour, Genda Gu, Jonathan Pelliciari, Nicholas B. Brookes, Peter Abbamonte, Marco Salluzzo, Xingjiang Zhou, Ke-Jin Zhou, Valentina Bisogni, Lucio Braicovich, Steven Johnston, and Giacomo Ghiringhelli. Doping dependence of the electron-phonon coupling in two families of bilayer superconducting cuprates. *Phys. Rev. B*, 105:115105, Mar 2022.

[30] Jinho Lee, K. Fujita, K. McElroy, J. A. Slezak, M. Wang, Y. Aiura, H. Bando, M. Ishikado, T. Masui, J. X. Zhu, A. V. Balatsky, H. Eisaki, S. Uchida, and J. C. Davis. Interplay of electron–lattice interactions and superconductivity in $Bi_2Sr_2CaCu_2O_{8+\delta}$. *Nature*, 442(7102):546–550, 2006.

[31] Guo-meng Zhao. Strong coupling to multiple phonon modes in high-temperature superconductors. *Phys. Rev. B*, 75:214507, Jun 2007.

[32] Jiemin Li, Abhishek Nag, Jonathan Pelliciari, Hannah Robarts, Andrew Walters, Mirian Garcia-Fernandez, Hiroshi Eisaki, Dongjoon Song, Hong Ding, Steven Johnston, Riccardo Comin, and Ke-Jin Zhou. Multiorbital charge-density wave excitations and concomitant phonon anomalies

in $Bi_2Sr_2LaCuO_{6+\delta}$. *Proceedings of the National Academy of Sciences*, 117(28):16219–16225, 2020.

[33] T. P. Devereaux, T. Cuk, Z.-X. Shen, and N. Nagaosa. Anisotropic electron-phonon interaction in the cuprates. *Phys. Rev. Lett.*, 93:117004, Sep 2004.

[34] S. Johnston, F. Vernay, B. Moritz, Z.-X. Shen, N. Nagaosa, J. Zaanen, and T. P. Devereaux. Systematic study of electron-phonon coupling to oxygen modes across the cuprates. *Phys. Rev. B*, 82:064513, Aug 2010.

[35] T. Holstein. Studies of polaron motion: Part I. The molecular-crystal model. *Annals of Physics*, 8(3):325–342, 1959.

[36] F. Marsiglio. Pairing and charge-density-wave correlations in the Holstein model at half-filling. *Phys. Rev. B*, 42:2416–2424, Aug 1990.

[37] P. M. Dee, K. Nakatsukasa, Y. Wang, and S. Johnston. Temperature-filling phase diagram of the two-dimensional holstein model in the thermodynamic limit by self-consistent migdal approximation. *Phys. Rev. B*, 99:024514, Jan 2019.

[38] B. Nosarzewski, E. W. Huang, Philip M. Dee, I. Esterlis, B. Moritz, S. A. Kivelson, S. Johnston, and T. P. Devereaux. Superconductivity, charge density waves, and bipolarons in the Holstein model. *Phys. Rev. B*, 103:235156, Jun 2021.

[39] W. P. Su, J. R. Schrieffer, and A. J. Heeger. Solitons in polyacetylene. *Phys. Rev. Lett.*, 42:1698–1701, Jun 1979.

[40] F. C. Zhang and T. M. Rice. Effective hamiltonian for the superconducting cu oxides. *Phys. Rev. B*, 37:3759–3761, Mar 1988.

[41] Benjamin Cohen-Stead, Owen Bradley, Cole Miles, George Batrouni, Richard Scalettar, and Kipton Barros. Fast and scalable quantum Monte Carlo simulations of electron-phonon models. *Phys. Rev. E*, 105:065302, Jun 2022.

[42] S. Gerber, S.-L. Yang, D. Zhu, H. Soifer, J. A. Sobota, S. Rebec, J. J. Lee, T. Jia, B. Moritz, C. Jia, A. Gauthier, Y. Li, D. Leuenberger, Y. Zhang, L. Chaix, W. Li, H. Jang, J.-S. Lee, M. Yi, G. L. Dakovski, S. Song, J. M. Glownia, S. Nelson, K. W. Kim, Y.-D. Chuang, Z. Hussain, R. G. Moore, T. P. Devereaux, W.-S. Lee, P. S. Kirchmann, and Z.-X. Shen. Femtosecond electron-phonon lock-in by photoemission and x-ray free-electron laser. *Science*, 357(6346):71–75, 2017.

[43] Chenglin Zhang, Leland W. Harriger, Zhiping Yin, Weicheng Lv, Miaoyin Wang, Guotai Tan, Yu Song, D. L. Abernathy, Wei Tian, Takeshi Egami, Kristjan Haule, Gabriel Kotliar, and Pengcheng Dai. Effect of pnictogen height on spin waves in iron pnictides. *Phys. Rev. Lett.*, 112:217202, May 2014.

[44] J. J. Lee, F. T. Schmitt, R. G. Moore, S. Johnston, Y. T. Cui, W. Li, M. Yi, Z. K. Liu, M. Hashimoto, Y. Zhang, D. H. Lu, T. P. Devereaux, D. H. Lee, and Z. X. Shen. Interfacial mode coupling as the origin of the enhancement of tc in fese films on srtio3. *Nature*, 515(7526):245–248, 2014.

[45] Guo-meng Zhao, K. Conder, M. Angst, S. M. Kazakov, J. Karpinski, M. Maciejewski, C. Bougerol, J. S. Pshirkov, and E. V. Antipov. Large oxygen-isotope effect in $Sr_{0.4}K_{0.6}BiO_3$: Evidence for phonon-mediated superconductivity. *Phys. Rev. B*, 62:R11977–R11980, Nov 2000.

[46] John Sous, Monodeep Chakraborty, Roman V. Krems, and Mona Berciu. Light Bipolarons Stabilized by Peierls Electron-Phonon Coupling. *Phys. Rev. Lett.*, 121:247001, Dec 2018.

[47] C. Zhang, J. Sous, D. R. Reichman, M. Berciu, A. J. Millis, N. V. Prokof'ev, and B. V. Svistunov. Bipolaronic high-temperature superconductivity. *Phys. Rev. X*, 13:011010, Jan 2023.

[48] M. Capone, W. Stephan, and M. Grilli. Small-polaron formation and optical absorption in Su-Schrieffer-Heeger and Holstein models. *Phys. Rev. B*, 56:4484–4493, Aug 1997.

[49] Manuel Weber, Fakher F. Assaad, and Martin Hohenadler. Excitation spectra and correlation functions of quantum Su-Schrieffer-Heeger models. *Phys. Rev. B*, 91:245147, Jun 2015.

[50] Martin C. Gutzwiller. Effect of correlation on the ferromagnetism of transition metals. *Phys. Rev. Lett.*, 10:159–162, Mar 1963.

[51] Junjiro Kanamori. Electron correlation and ferromagnetism of transition metals. *Progress of Theoretical Physics*, 30(3):275–289, 09 1963.

[52] J. Hubbard. Electron Correlations in Narrow Energy Bands. III. An Improved Solution. *Proceedings of the Royal Society of London Series A*, 281(1386):401–419, 1964.

[53] J. Hubbard. Electron correlations in narrow energy bands. iii. an improved solution. *Proceedings of the Royal Society of London. Series A, Mathematical and Physical Sciences*, 281(1386):401–419, 1964.

[54] Elliott H. Lieb and F. Y. Wu. Absence of mott transition in an exact solution of the short-range, one-band model in one dimension. *Phys. Rev. Lett.*, 20:1445–1448, Jun 1968.

[55] Margaret Ghiron. John Hubbard: The Hubbard model 50 years on. In *Hubbard Theory Consortium Special Event - 50th Anniversary of the Hubbard Model*, London, England, June 2013. Presentation.

[56] David Emin, Myron P. Garfunkel, Moises Levy, Bernard M. K. Nefkens, and Harvey Scher. Theodore David Holstein. *Physics Today*, 39, Sep 1986.

[57] Lev Davidovich Landau. Electron Motion in Crystal Lattices. *Phys. Z. Sowjetunion*, 3, 1933.

[58] H. Fröhlich. Electrons in lattice fields. *Advances in Physics*, 3(11):325–361, 1954.

[59] T. Holstein. Studies of polaron motion: Part II. The "small" polaron. *Annals of Physics*, 8(3):343–389, 1959.

[60] M. Capone, W. Stephan, and M. Grilli. Small-polaron formation and optical absorption in Su-Schrieffer-Heeger and Holstein models. *Phys. Rev. B*, 56:4484–4493, Aug 1997.

[61] J. Labbé, S. Barišić, and J. Friedel. Strong-coupling superconductivity in V_3X type of compounds. *Phys. Rev. Lett.*, 19:1039–1041, Oct 1967.

[62] Pinaki Sengupta, Anders W. Sandvik, and David K. Campbell. Peierls transition in the presence of finite-frequency phonons in the one-dimensional extended Peierls-Hubbard model at half-filling. *Phys. Rev. B*, 67:245103, Jun 2003.

[63] Philip B. Allen and Božidar Mitrović. Theory of superconducting T_c. volume 37 of *Solid State Physics*, pages 1–92. Academic Press, 1983.

[64] Zhou Li, Carl J. Chandler, and F. Marsiglio. Perturbation theory of the mass enhancement for a polaron coupled to acoustic phonons. *Phys. Rev. B*, 83:045104, Jan 2011.

[65] Chao Zhang, Nikolay V. Prokof'ev, and Boris V. Svistunov. Peierls/Su-Schrieffer-Heeger polarons in two dimensions. *Phys. Rev. B*, 104:035143, Jul 2021.

[66] Sohan Malkaruge Costa, Benjamin Cohen-Stead, Andy Tanjaroon Ly, James Neuhaus, and Steven Johnston. Comparative determinant quantum Monte Carlo study of the acoustic and optical variants of the Su-Schrieffer-Heeger model. *Phys. Rev. B*, 108:165138, Oct 2023.

[67] Steven R. White. Density matrix formulation for quantum renormalization groups. *Phys. Rev. Lett.*, 69:2863–2866, Nov 1992.

[68] U. Schollwöck. The density-matrix renormalization group. *Rev. Mod. Phys.*, 77:259–315, Apr 2005.

[69] Federico Becca and Sandro Sorella. *Quantum Monte Carlo Approaches for Correlated Systems*. Cambridge University Press, 2017.

[70] R. Rüger. Implementation of the Variational Monte Carlo method for the Hubbard model, 2013. Master's Thesis.

[71] Nicholas Metropolis, Arianna W. Rosenbluth, Marshall N. Rosenbluth, Augusta H. Teller, and Edward Teller. Equation of state calculations by fast computing machines. *The Journal of Chemical Physics*, 21(6):1087–1092, 06 1953.

[72] Sandro Sorella. Green function monte carlo with stochastic reconfiguration. *Phys. Rev. Lett.*, 80:4558–4561, May 1998.

[73] Sandro Sorella. Generalized lanczos algorithm for variational quantum monte carlo. *Phys. Rev. B*, 64:024512, Jun 2001.

[74] Manuela Capello, Federico Becca, Michele Fabrizio, Sandro Sorella, and Erio Tosatti. Variational description of mott insulators. *Phys. Rev. Lett.*, 94:026406, Jan 2005.

[75] Manuela Capello, Federico Becca, Seiji Yunoki, and Sandro Sorella. Unconventional metal-insulator transition in two dimensions. *Phys. Rev. B*, 73:245116, Jun 2006.

[76] Seher Karakuzu, Luca F. Tocchio, Sandro Sorella, and Federico Becca. Superconductivity, charge-density waves, antiferromagnetism, and phase separation in the Hubbard-Holstein model. *Phys. Rev. B*, 96:205145, Nov 2017.

[77] S. R. White, D. J. Scalapino, R. L. Sugar, E. Y. Loh, J. E. Gubernatis, and R. T. Scalettar. Numerical study of the two-dimensional Hubbard model. *Phys. Rev. B*, 40:506–516, Jul 1989.

[78] R. M. Fye. New results on trotter-like approximations. *Phys. Rev. B*, 33:6271–6280, May 1986.

[79] R. M. Fye and R. T. Scalettar. Calculation of specific heat and susceptibilities with the use of the trotter approximation. *Phys. Rev. B*, 36:3833–3843, Sep 1987.

[80] J. E. Hirsch. Two-dimensional hubbard model: Numerical simulation study. *Phys. Rev. B*, 31:4403–4419, Apr 1985.

[81] R. Blankenbecler, D. J. Scalapino, and R. L. Sugar. Monte carlo calculations of coupled boson-fermion systems. i. *Phys. Rev. D*, 24:2278–2286, Oct 1981.

[82] Gaopei Pan and Zi Yang Meng. The sign problem in quantum monte carlo simulations. In Tapash Chakraborty, editor, *Encyclopedia of Condensed Matter Physics (Second Edition)*, pages 879–893. Academic Press, Oxford, second edition edition, 2024.

[83] E. Y. Loh, J. E. Gubernatis, R. T. Scalettar, S. R. White, D. J. Scalapino, and R. L. Sugar. Sign problem in the numerical simulation of many-electron systems. *Phys. Rev. B*, 41:9301–9307, May 1990.

[84] V. I. Iglovikov, E. Khatami, and R. T. Scalettar. Geometry dependence of the sign problem in quantum monte carlo simulations. *Phys. Rev. B*, 92:045110, Jul 2015.

[85] Simon Duane, A.D. Kennedy, Brian J. Pendleton, and Duncan Roweth. Hybrid monte carlo. *Physics Letters B*, 195(2):216–222, 1987.

[86] Benjamin Cohen-Stead, Sohan Malkaruge Costa, James Neuhaus, Andy Tanjaroon Ly, Yutan Zhang, Richard Scalettar, Kipton Barros, and Steven Johnston. SmoQyDQMC.jl: A flexible implementation of determinant quantum Monte Carlo for Hubbard and electron-phonon interactions. *SciPost Phys. Codebases*, page 29, 2024.

[87] Cole Miles, Benjamin Cohen-Stead, Owen Bradley, Steven Johnston, Richard Scalettar, and Kipton Barros. Dynamical tuning of the chemical potential to achieve a target particle number in grand canonical monte carlo simulations. *Phys. Rev. E*, 105:045311, Apr 2022.

[88] Ribhu K. Kaul. Spin nematics, valence-bond solids, and spin liquids in SO(N) quantum spin models on the triangular lattice. *Phys. Rev. Lett.*, 115:157202, Oct 2015.

[89] Toshihiro Sato, Fakher F. Assaad, and Tarun Grover. Quantum Monte Carlo simulation of frustrated Kondo lattice models. *Phys. Rev. Lett.*, 120:107201, Mar 2018.

[90] Zi Hong Liu, Xiao Yan Xu, Yang Qi, Kai Sun, and Zi Yang Meng. Itinerant quantum critical point with frustration and a non-fermi liquid. *Phys. Rev. B*, 98:045116, Jul 2018.

[91] Andrew S. Darmawan, Yusuke Nomura, Youhei Yamaji, and Masatoshi Imada. Stripe and superconducting order competing in the Hubbard model on a

square lattice studied by a combined variational Monte Carlo and tensor network method. *Phys. Rev. B*, 98:205132, Nov 2018.

[92] Seher Karakuzu, Andy Tanjaroon Ly, Peizhi Mai, James Neuhaus, Thomas A. Maier, and Steven Johnston. Stripe correlations in the two-dimensional hubbard-holstein model. *Communications Physics*, 5(1):311, 2022.

[93] Eduardo Fradkin, Steven A. Kivelson, and John M. Tranquada. Colloquium: Theory of intertwined orders in high temperature superconductors. *Rev. Mod. Phys.*, 87:457–482, May 2015.

[94] B. Keimer, S. A. Kivelson, M. R. Norman, S. Uchida, and J. Zaanen. From quantum matter to high-temperature superconductivity in copper oxides. *Nature*, 518(7538):179–186, 2015.

[95] J. M. Tranquada, B. J. Sternlieb, J. D. Axe, Y. Nakamura, and S. Uchida. Evidence for stripe correlations of spins and holes in copper oxide superconductors. *Nature*, 375(6532):561–563, 1995.

[96] H.-H. Klauss, W. Wagener, M. Hillberg, W. Kopmann, H. Walf, F. J. Litterst, M. Hücker, and B. Büchner. From antiferromagnetic order to static magnetic stripes: The phase diagram of $(La,Eu)_{2-x}Sr_xCuO_4$. *Phys. Rev. Lett.*, 85:4590–4593, Nov 2000.

[97] M. Fujita, H. Goka, K. Yamada, J. M. Tranquada, and L. P. Regnault. Stripe order, depinning, and fluctuations in $La_{1.875}Ba_{0.125}CuO_4$ and $La_{1.875}Ba_{0.075}Sr_{0.050}CuO_4$. *Phys. Rev. B*, 70:104517, Sep 2004.

[98] J. M. Tranquada, G. D. Gu, M. Hücker, Q. Jie, H.-J. Kang, R. Klingeler, Q. Li, N. Tristan, J. S. Wen, G. Y. Xu, Z. J. Xu, J. Zhou, and M. v. Zimmermann. Evidence for unusual superconducting correlations coexisting with stripe order in $La_{1.875}Ba_{0.125}CuO_4$. *Phys. Rev. B*, 78:174529, Nov 2008.

[99] Jan Zaanen and Olle Gunnarsson. Charged magnetic domain lines and the magnetism of high-T_c oxides. *Phys. Rev. B*, 40:7391–7394, Oct 1989.

[100] Kazushige Machida. Magnetism in La_2CuO_4 based compounds. *Physica C: Superconductivity*, 158(1):192–196, 1989.

[101] Steven R. White and D. J. Scalapino. Density matrix renormalization group study of the striped phase in the 2D $t-J$ model. *Phys. Rev. Lett.*, 80:1272–1275, Feb 1998.

[102] Steven R. White and D. J. Scalapino. Energetics of domain walls in the 2D $t-J$ model. *Phys. Rev. Lett.*, 81:3227–3230, Oct 1998.

[103] D. Poilblanc and T. M. Rice. Charged solitons in the Hartree-Fock approximation to the large-U Hubbard model. *Phys. Rev. B*, 39:9749–9752, May 1989.

[104] Mostafa Sherif Derbala Aly Hussein, Elbio Dagotto, and Adriana Moreo. Half-filled stripes in a hole-doped three-orbital spin-fermion model for cuprates. *Phys. Rev. B*, 99:115108, Mar 2019.

[105] Mingpu Qin, Chia-Min Chung, Hao Shi, Ettore Vitali, Claudius Hubig, Ulrich Schollwöck, Steven R. White, and Shiwei Zhang. Absence of superconductivity in the pure two-dimensional Hubbard model. *Phys. Rev. X*, 10:031016, Jul 2020.

[106] Mitake Miyazaki, Kunihiko Yamaji, and Takashi Yanagisawa. Stripes and d-wave superconductivity in the two-dimensional Hubbard model. *Physics Procedia*, 58:30–33, 2014. Proceedings of the 26th International Symposium on Superconductivity (ISS 2013).

[107] Philippe Corboz, T. M. Rice, and Matthias Troyer. Competing States in the *t-J* Model: Uniform d-Wave State versus Stripe State. *Phys. Rev. Lett.*, 113:046402, Jul 2014.

[108] Edwin W. Huang, Christian B. Mendl, Shenxiu Liu, Steve Johnston, Hong-Chen Jiang, Brian Moritz, and Thomas P. Devereaux. Numerical evidence of fluctuating stripes in the normal state of high-T_c cuprate superconductors. *Science*, 358(6367):1161–1164, 2017.

[109] Edwin W. Huang, Christian B. Mendl, Hong-Chen Jiang, Brian Moritz, and Thomas P. Devereaux. Stripe order from the perspective of the Hubbard model. *npj Quantum Materials*, 3(1):22, 2018.

[110] Yi-Fan Jiang, Jan Zaanen, Thomas P. Devereaux, and Hong-Chen Jiang. Ground state phase diagram of the doped Hubbard model on the four-leg cylinder. *Phys. Rev. Research*, 2:033073, Jul 2020.

[111] Sandro Sorella. The phase diagram of the Hubbard model by variational auxiliary field quantum Monte Carlo. *arXiv:2101.07045*, 2021.

[112] Edwin W. Huang, Tianyi Liu, Wen O. Wang, Hong-Chen Jiang, Peizhi Mai, Thomas A. Maier, Steven Johnston, Brian Moritz, and Thomas P. Devereaux. Fluctuating intertwined stripes in the strange metal regime of the hubbard model. *Phys. Rev. B*, 107:085126, Feb 2023.

[113] Peizhi Mai, Seher Karakuzu, Giovanni Balduzzi, Steven Johnston, and Thomas A. Maier. Intertwined spin, charge, and pair correlations in the two-dimensional Hubbard model in the thermodynamic limit. *Proceedings of the National Academy of Sciences*, 119(7):e2112806119, 2022.

[114] Bo Xiao, Yuan-Yao He, Antoine Georges, and Shiwei Zhang. Temperature dependence of spin and charge orders in the doped two-dimensional hubbard model. *Phys. Rev. X*, 13:011007, Jan 2023.

[115] Fedor Šimkovic IV, Riccardo Rossi, and Michel Ferrero. Two-dimensional hubbard model at finite temperature: Weak, strong, and long correlation regimes. *Phys. Rev. Res.*, 4:043201, Dec 2022.

[116] T. P. Devereaux, T. Cuk, Z.-X. Shen, and N. Nagaosa. Anisotropic electron-phonon interaction in the cuprates. *Phys. Rev. Lett.*, 93:117004, Sep 2004.

[117] K. M. Shen, F. Ronning, D. H. Lu, W. S. Lee, N. J. C. Ingle, W. Meevasana, F. Baumberger, A. Damascelli, N. P. Armitage, L. L. Miller, Y. Kohsaka, M. Azuma, M. Takano, H. Takagi, and Z.-X. Shen. Missing quasiparticles and the chemical potential puzzle in the doping evolution of the cuprate superconductors. *Phys. Rev. Lett.*, 93:267002, Dec 2004.

[118] Jinho Lee, K. Fujita, K. McElroy, J. A. Slezak, M. Wang, Y. Aiura, H. Bando, M. Ishikado, T. Masui, J. X. Zhu, A. V. Balatsky, H. Eisaki, S. Uchida, and J. C. Davis. Interplay of electron–lattice interactions and superconductivity in $Bi_2Sr_2CaCu_2O_{8+\delta}$. *Nature*, 442(7102):546–550, 2006.

[119] W. S. Lee, S. Johnston, T. P. Devereaux, and Z.-X. Shen. Aspects of electron-phonon self-energy revealed from angle-resolved photoemission spectroscopy. *Phys. Rev. B*, 75:195116, May 2007.

[120] Matteo Rossi, Riccardo Arpaia, Roberto Fumagalli, Marco Moretti Sala, Davide Betto, Kurt Kummer, Gabriella M. De Luca, Jeroen van den Brink, Marco Salluzzo, Nicholas B. Brookes, Lucio Braicovich, and Giacomo Ghiringhelli. Experimental determination of momentum-resolved electron-phonon coupling. *Phys. Rev. Lett.*, 123:027001, Jul 2019.

[121] Zhuoyu Chen, Yao Wang, Slavko N. Rebec, Tao Jia, Makoto Hashimoto, Donghui Lu, Brian Moritz, Robert G. Moore, Thomas P. Devereaux, and Zhi-Xun Shen. Anomalously strong near-neighbor attraction in doped 1D cuprate chains. *Science*, 373(6560):1235–1239, 2021.

[122] L. Chaix, G. Ghiringhelli, Y. Y. Peng, M. Hashimoto, B. Moritz, K. Kummer, N. B. Brookes, Y. He, S. Chen, S. Ishida, Y. Yoshida, H. Eisaki, M. Salluzzo, L. Braicovich, Z. X. Shen, T. P. Devereaux, and W. S. Lee. Dispersive charge

density wave excitations in $Bi_2Sr_2CaCu_2O_{8+\delta}$. *Nature Physics*, 13(10):952–956, 2017.

[123] Qisi Wang, Karin von Arx, Masafumi Horio, Deepak John Mukkattukavil, Julia Küspert, Yasmine Sassa, Thorsten Schmitt, Abhishek Nag, Sunseng Pyon, Tomohiro Takayama, Hidenori Takagi, Mirian Garcia-Fernandez, Ke-Jin Zhou, and Johan Chang. Charge order lock-in by electron-phonon coupling in $La_{1.675}Eu_{0.2}Sr_{0.125}CuO_4$. *Science Advances*, 7(27):eabg7394, 2021.

[124] Yingying Peng, Leonardo Martinelli, Qizhi Li, Matteo Rossi, Matteo Mitrano, Riccardo Arpaia, Marco Moretti Sala, Qiang Gao, Xuefei Guo, Gabriella Maria De Luca, Andrew Walters, Abhishek Nag, Andi Barbour, Genda Gu, Jonathan Pelliciari, Nicholas B. Brookes, Peter Abbamonte, Marco Salluzzo, Xingjiang Zhou, Ke-Jin Zhou, Valentina Bisogni, Lucio Braicovich, Steven Johnston, and Giacomo Ghiringhelli. Doping dependence of the electron-phonon coupling in two families of bilayer superconducting cuprates. *Phys. Rev. B*, 105:115105, Mar 2022.

[125] S. Banerjee, W. A. Atkinson, and A. P. Kampf. Emergent charge order from correlated electron-phonon physics in cuprates. *Communications Physics*, 3(1):161, 2020.

[126] Riccardo Comin and Andrea Damascelli. Resonant x-ray scattering studies of charge order in cuprates. *Annual Review of Condensed Matter Physics*, 7(1):369–405, 2016.

[127] Riccardo Arpaia and Giacomo Ghiringhelli. Charge order at high temperature in cuprate superconductors. *Journal of the Physical Society of Japan*, 90(11):111005, 2021.

[128] Johannes Bauer and Alex C. Hewson. Competition between antiferromagnetic and charge order in the Hubbard-Holstein model. *Phys. Rev. B*, 81:235113, Jun 2010.

[129] E. A. Nowadnick, S. Johnston, B. Moritz, R. T. Scalettar, and T. P. Devereaux. Competition between antiferromagnetic and charge-density-wave order in the half-filled Hubbard-Holstein model. *Phys. Rev. Lett.*, 109:246404, Dec 2012.

[130] S. Johnston, E. A. Nowadnick, Y. F. Kung, B. Moritz, R. T. Scalettar, and T. P. Devereaux. Determinant quantum Monte Carlo study of the two-dimensional single-band Hubbard-Holstein model. *Phys. Rev. B*, 87:235133, Jun 2013.

[131] C. B. Mendl, E. A. Nowadnick, E. W. Huang, S. Johnston, B. Moritz, and T. P. Devereaux. Doping dependence of ordered phases and emergent quasiparticles in the doped Hubbard-Holstein model. *Phys. Rev. B*, 96:205141, Nov 2017.

[132] Takahiro Ohgoe and Masatoshi Imada. Competition among superconducting, antiferromagnetic, and charge orders with intervention by phase separation in the 2D Holstein-Hubbard model. *Phys. Rev. Lett.*, 119:197001, Nov 2017.

[133] Manuel Weber and Martin Hohenadler. Two-dimensional Holstein-Hubbard model: Critical temperature, ising universality, and bipolaron liquid. *Phys. Rev. B*, 98:085405, Aug 2018.

[134] Natanael C. Costa, Kazuhiro Seki, Seiji Yunoki, and Sandro Sorella. Phase diagram of the two-dimensional Hubbard-Holstein model. *Communications Physics*, 3(1):80, 2020.

[135] Z. B. Huang, W. Hanke, E. Arrigoni, and D. J. Scalapino. Electron-phonon vertex in the two-dimensional one-band Hubbard model. *Phys. Rev. B*, 68:220507, Dec 2003.

[136] Carsten Honerkamp, Henry C. Fu, and Dung-Hai Lee. Phonons and *d*-wave pairing in the two-dimensional Hubbard model. *Phys. Rev. B*, 75:014503, Jan 2007.

[137] V. J. Emery, S. A. Kivelson, and H. Q. Lin. Phase separation in the *t-J* model. *Phys. Rev. Lett.*, 64:475–478, Jan 1990.

[138] Luca F. Tocchio, Federico Becca, and Sandro Sorella. Hidden Mott transition and large-*U* superconductivity in the two-dimensional Hubbard model. *Phys. Rev. B*, 94:195126, Nov 2016.

[139] M. K. Crawford, M. N. Kunchur, W. E. Farneth, E. M. McCarron III, and S. J. Poon. Anomalous oxygen isotope effect in $La_{2-x}Sr_xCuO_4$. *Phys. Rev. B*, 41:282–287, Jan 1990.

[140] G. Paleari, F. Hébert, B. Cohen-Stead, K. Barros, RT. Scalettar, and G. G. Batrouni. Quantum Monte Carlo study of an anharmonic Holstein model. *Phys. Rev. B*, 103:195117, May 2021.

[141] Owen Bradley, George G. Batrouni, and Richard T. Scalettar. Superconductivity and charge density wave order in the two-dimensional Holstein model. *Phys. Rev. B*, 103:235104, Jun 2021.

[142] Bo Xiao, F. Hébert, G. Batrouni, and R. T. Scalettar. Competition between phase separation and spin density wave or charge density wave order: Role of long-range interactions. *Phys. Rev. B*, 99:205145, May 2019.

[143] F. Hébert, Bo Xiao, V. G. Rousseau, R. T. Scalettar, and G. G. Batrouni. One-dimensional Hubbard-Holstein model with finite-range electron-phonon coupling. *Phys. Rev. B*, 99:075108, Feb 2019.

[144] Shaozhi Li and Steven Johnston. Quantum Monte Carlo study of lattice polarons in the two-dimensional three-orbital Su–Schrieffer–Heeger model. *npj Quantum Materials*, 5(1):40, 2020.

[145] Andy Tanjaroon Ly, Benjamin Cohen-Stead, Sohan Malkaruge Costa, and Steven Johnston. Comparative study of the superconductivity in the holstein and optical su-schrieffer-heeger models. *Phys. Rev. B*, 108:184501, Nov 2023.

[146] M. L. Cohen and P. W. Anderson. Comments on the maximum superconducting transition temperature. *AIP Conference Proceedings*, 4:17–27, 1972.

[147] C. R. Leavens. A least upper bound on the superconducting transition temperature. *Solid State Communications*, 17(12):1499–1504, 1975.

[148] P. B. Allen and R. C. Dynes. Transition temperature of strong-coupled superconductors reanalyzed. *Phys. Rev. B*, 12:905–922, Aug 1975.

[149] J. P. Carbotte. Properties of boson-exchange superconductors. *Rev. Mod. Phys.*, 62:1027–1157, Oct 1990.

[150] Thereza Paiva, Raimundo R. dos Santos, R. T. Scalettar, and P. J. H. Denteneer. Critical temperature for the two-dimensional attractive Hubbard model. *Phys. Rev. B*, 69:184501, May 2004.

[151] Jonathan E. Moussa and Marvin L. Cohen. Two bounds on the maximum phonon-mediated superconducting transition temperature. *Phys. Rev. B*, 74:094520, Sep 2006.

[152] Erez Berg, Dror Orgad, and Steven A. Kivelson. Route to high-temperature superconductivity in composite systems. *Phys. Rev. B*, 78:094509, Sep 2008.

[153] C. M. Varma. Considerations on the mechanisms and transition temperatures of superconductivity induced by electronic fluctuations. *Reports on Progress in Physics*, 75(5):052501, apr 2012.

[154] Chungwei Lin, Bingnan Wang, and Koon Hoo Teo. Optimal boson energy for superconductivity in the Holstein model. *Phys. Rev. B*, 93:224501, Jun 2016.

[155] I. Esterlis, S. A. Kivelson, and D. J. Scalapino. A bound on the superconducting transition temperature. *npj Quantum Materials*, 3(1):59, 2018.

[156] Tamaghna Hazra, Nishchhal Verma, and Mohit Randeria. Bounds on the superconducting transition temperature: Applications to twisted bilayer graphene and cold atoms. *Phys. Rev. X*, 9:031049, Sep 2019.

[157] A. S. Alexandrov. Breakdown of the Migdal-Eliashberg theory in the strong-coupling adiabatic regime. *Europhysics Letters*, 56(1):92, oct 2001.

[158] I. Esterlis, B. Nosarzewski, E. W. Huang, B. Moritz, T. P. Devereaux, D. J. Scalapino, and S. A. Kivelson. Breakdown of the Migdal-Eliashberg theory: A determinant quantum Monte Carlo study. *Phys. Rev. B*, 97:140501, Apr 2018.

[159] S. Barišić, J. Labbé, and J. Friedel. Tight binding and transition-metal superconductivity. *Phys. Rev. Lett.*, 25:919–922, Oct 1970.

[160] Yau-Chuen Yam, Mirko M. Moeller, George A. Sawatzky, and Mona Berciu. Peierls versus Holstein models for describing electron-phonon coupling in perovskites. *Phys. Rev. B*, 102:235145, Dec 2020.

[161] Bo Xing, Wei-Ting Chiu, Dario Poletti, R. T. Scalettar, and George Batrouni. Quantum Monte Carlo simulations of the 2D Su-Schrieffer-Heeger model. *Phys. Rev. Lett.*, 126:017601, Jan 2021.

[162] Alberto Nocera, John Sous, Adrian E. Feiguin, and Mona Berciu. Bipolaron liquids at strong Peierls electron-phonon couplings. *Phys. Rev. B*, 104:L201109, Nov 2021.

[163] Chunhan Feng, Bo Xing, Dario Poletti, Richard Scalettar, and George Batrouni. Phase diagram of the Su-Schrieffer-Heeger-Hubbard model on a square lattice. *Phys. Rev. B*, 106:L081114, Aug 2022.

[164] J. Sous, C. Zhang, M. Berciu, D. R. Reichman, B. V. Svistunov, N. V. Prokof'ev, and A. J. Millis. Bipolaronic superconductivity out of a coulomb gas. *Phys. Rev. B*, 108:L220502, Dec 2023.

[165] Benjamin Cohen-Stead, Kipton Barros, Richard Scalettar, and Steven Johnston. A hybrid Monte Carlo study of bond-stretching electron–phonon interactions and charge order in $BaBiO_3$. *npj Computational Materials*, 9(1):40, 2023.

[166] Debshikha Banerjee, Jinu Thomas, Alberto Nocera, and Steven Johnston. Ground-state and spectral properties of the doped one-dimensional optical Hubbard-Su-Schrieffer-Heeger model. *Phys. Rev. B*, 107:235113, Jun 2023.

[167] Anika Götz, Martin Hohenadler, and Fakher F. Assaad. Phases and exotic phase transitions of a two-dimensional su-schrieffer-heeger model. *Phys. Rev. B*, 109:195154, May 2024.

[168] Qing-Geng Yang, Da Wang, and Qiang-Hua Wang. Functional renormalization group study of the two-dimensional su-schrieffer-heeger-hubbard model. *Phys. Rev. B*, 106:245136, Dec 2022.

[169] Chao Zhang, Nikolay V. Prokof'ev, and Boris V. Svistunov. Bond bipolarons: Sign-free Monte Carlo approach. *Phys. Rev. B*, 105:L020501, Jan 2022.

[170] S. Pilati, S. Giorgini, and N. Prokof'ev. Critical temperature of interacting Bose gases in two and three dimensions. *Phys. Rev. Lett.*, 100:140405, Apr 2008.

[171] R. T. Scalettar, N. E. Bickers, and D. J. Scalapino. Competition of pairing and Peierls–charge-density-wave correlations in a two-dimensional electron-phonon model. *Phys. Rev. B*, 40:197–200, Jul 1989.

[172] R. M. Noack, D. J. Scalapino, and R. T. Scalettar. Charge-density-wave and pairing susceptibilities in a two-dimensional electron-phonon model. *Phys. Rev. Lett.*, 66:778–781, Feb 1991.

[173] Martin Hohenadler, Hans Gerd Evertz, and Wolfgang von der Linden. Quantum Monte Carlo and variational approaches to the Holstein model. *Phys. Rev. B*, 69:024301, Jan 2004.

[174] Philip M. Dee, Benjamin Cohen-Stead, Steven Johnston, and P. J. Hirschfeld. Charge correlations suppress unconventional pairing in the Holstein model. *Phys. Rev. B*, 107:104503, Mar 2023.

[175] B. Cohen-Stead, Kipton Barros, ZY Meng, Chuang Chen, R. T. Scalettar, and G. G. Batrouni. Langevin simulations of the half-filled cubic Holstein model. *Phys. Rev. B*, 102:161108, Oct 2020.

[176] Xun Cai, Zi-Xiang Li, and Hong Yao. Robustness of antiferromagnetism in the Su-Schrieffer-Heeger Hubbard model. *Phys. Rev. B*, 106:L081115, Aug 2022.

[177] Shaozhi Li and Steven Johnston. Suppressed superexchange interactions in the cuprates by bond-stretching oxygen phonons. *Phys. Rev. B*, 108:L201113, Nov 2023.

[178] A. Götz, S. Beyl, M. Hohenadler, and F. F. Assaad. Valence-bond solid to antiferromagnet transition in the two-dimensional su-schrieffer-heeger model by langevin dynamics. *Phys. Rev. B*, 105:085151, Feb 2022.

[179] Arthur W. Sleight. Bismuthates: $BaBiO_3$ and related superconducting phases. *Physica C: Superconductivity and its Applications*, 514:152–165, 2015.

[180] Louis-Fran çois Arsenault, Patrick Sémon, and A.-M. S. Tremblay. Benchmark of a modified iterated perturbation theory approach on the fcc lattice at strong coupling. *Phys. Rev. B*, 86:085133, Aug 2012.

[181] Jason Kaye, Kun Chen, and Olivier Parcollet. Discrete Lehmann representation of imaginary time Green's functions. *Phys. Rev. B*, 105:235115, Jun 2022.

[182] Jason Kaye, Kun Chen, and Hugo U.R. Strand. libdlr: Efficient imaginary time calculations using the discrete Lehmann representation. *Computer Physics Communications*, 280:108458, 2022.

[183] Peizhi Mai, Giovanni Balduzzi, Steven Johnston, and Thomas A. Maier. Pairing correlations in the cuprates: A numerical study of the three-band Hubbard model. *Phys. Rev. B*, 103:144514, Apr 2021.

[184] Shaozhi Li and S. Johnston. The effects of non-linear electron-phonon interactions on superconductivity and charge-density-wave correlations. *Europhysics Letters*, 109(2):27007, feb 2015.

[185] Philip M. Dee, Jennifer Coulter, Kevin G. Kleiner, and Steven Johnston. Relative importance of nonlinear electron-phonon coupling and vertex corrections in the Holstein model. *Communications Physics*, 3(1):145, 2020.

[186] John Sous, Benedikt Kloss, Dante M. Kennes, David R. Reichman, and Andrew J. Millis. Phonon-induced disorder in dynamics of optically pumped metals from nonlinear electron-phonon coupling. *Nature Communications*, 12(1):5803, 2021.

[187] K. Kovač, D. Golež, M. Mierzejewski, and J. Bonča. Optical manipulation of bipolarons in a system with nonlinear electron-phonon coupling. *Phys. Rev. Lett.*, 132:106001, Mar 2024.

[188] Andy Tanjaroon Ly, Benjamin Cohen-Stead, and Steven Johnston. Antiferromagnetic and bond-order-wave phases in the half-filled two-dimensional optical su-schrieffer-heeger-hubbard model. *Phys. Rev. B*, 111:245138, Jun 2025.

[189] Elbio Dagotto. Complexity in strongly correlated electronic systems. *Science*, 309(5732):257–262, 2005.

[190] Emilia Morosan, Douglas Natelson, Andriy H. Nevidomskyy, and Qimiao Si. Strongly correlated materials. *Advanced Materials*, 24(36):4896–4923, 2012.

[191] J. C. Séamus Davis and Dung-Hai Lee. Concepts relating magnetic interactions, intertwined electronic orders, and strongly correlated superconductivity. *Proceedings of the National Academy of Sciences*, 110(44):17623–17630, 2013.

[192] W. Koller, D. Meyer, Y. Ōno, and A. C. Hewson. First- and second-order phase transitions in the Holstein-Hubbard model. *Europhysics Letters*, 66(4):559, May 2004.

[193] Philipp Werner and Andrew J. Millis. Efficient dynamical mean field simulation of the Holstein-Hubbard model. *Phys. Rev. Lett.*, 99:146404, Oct 2007.

[194] E. A. Nowadnick, S. Johnston, B. Moritz, and T. P. Devereaux. Renormalization of spectra by phase competition in the half-filled Hubbard-Holstein model. *Phys. Rev. B*, 91:165127, Apr 2015.

[195] Yao Wang, Ilya Esterlis, Tao Shi, J. Ignacio Cirac, and Eugene Demler. Zero-temperature phases of the two-dimensional Hubbard-Holstein model: A non-Gaussian exact diagonalization study. *Phys. Rev. Res.*, 2:043258, Nov 2020.

[196] Roland Zeyher and Miodrag L. Kulić. Renormalization of the electron-phonon interaction by strong electronic correlations in high-T_c superconductors. *Phys. Rev. B*, 53:2850–2862, Feb 1996.

[197] Jiarui Liu, Shaozhi Li, Edwin W. Huang, and Yao Wang. Charge density wave state in extremely overdoped cuprates driven by phonons. *Phys. Rev. B*, 110:115133, Sep 2024.

[198] Xun Cai, Zi-Xiang Li, and Hong Yao. High-temperature superconductivity induced by the Su-Schrieffer-Heeger electron-phonon coupling. *arXiv:2308.06222*, 2023.

[199] Xun Cai, Zi-Xiang Li, and Hong Yao. Antiferromagnetism Induced by bond Su-Schrieffer-Heeger electron-phonon coupling: A quantum Monte Carlo study. *Phys. Rev. Lett.*, 127:247203, Dec 2021.

[200] Bo Xing, Chunhan Feng, Richard Scalettar, G. George Batrouni, and Dario Poletti. Attractive Su-Schrieffer-Heeger-Hubbard model on a square lattice away from half-filling. *Phys. Rev. B*, 108:L161103, Oct 2023.

[201] Steve Johnston, Anamitra Mukherjee, Ilya Elfimov, Mona Berciu, and George A. Sawatzky. Charge Disproportionation without Charge Transfer in the Rare-Earth-Element Nickelates as a Possible Mechanism for the Metal-Insulator Transition. *Phys. Rev. Lett.*, 112:106404, Mar 2014.

[202] Anika Götz, Martin Hohenadler, and Fakher F. Assaad. Phases and exotic phase transitions of a two-dimensional Su-Schrieffer-Heeger model. *Phys. Rev. B*, 109:195154, May 2024.

[203] Maxwell Casebolt, Chunhan Feng, Richard T. Scalettar, Steven Johnston, and G. G. Batrouni. Magnetic, charge, and bond order in the two-dimensional Su-Schrieffer-Heeger-Holstein model. *Phys. Rev. B*, 110:045112, Jul 2024.

[204] Ori Grossman and Erez Berg. Robust Fermi-Liquid Instabilities in Sign Problem-Free Models. *Phys. Rev. Lett.*, 131:056501, Aug 2023.

[205] Steven T. Bramwell and Bernhard Keimer. Neutron scattering from quantum condensed matter. *Nature Materials*, 13(8):763–767, 2014.

[206] M. Mitrano, S. Johnston, Young-June Kim, and M. P. M. Dean. Exploring quantum materials with resonant inelastic x-ray scattering. *Phys. Rev. X*, 14:040501, Dec 2024.

[207] Debshikha Banerjee, Jinu Thomas, Alberto Nocera, and Steven Johnston. Identifying and quantifying Su-Schrieffer-Heeger-like interactions with RIXS. *arXiv:2412.15981*, 2024.

[208] Francesco Ferrari, Roser Valentí, and Federico Becca. Variational wave functions for the spin-peierls transition in the su-schrieffer-heeger model with quantum phonons. *Phys. Rev. B*, 102:125149, Sep 2020.

[209] Davide Piccioni, Francesco Ferrari, Michele Fabrizio, and Federico Becca. Insulating and metallic phases in the one-dimensional hubbard-su-schrieffer-heeger model: Insights from a backflow-inspired variational wave function. *Phys. Rev. B*, 111:045125, Jan 2025.

[210] M. H. Hamidian, S. D. Edkins, Sang Hyun Joo, A. Kostin, H. Eisaki, S. Uchida, M. J. Lawler, E. A. Kim, A. P. Mackenzie, K. Fujita, Jinho Lee, and J. C. Séamus Davis. Detection of a cooper-pair density wave in bi2sr2cacu208+x. *Nature*, 532(7599):343–347, 2016.

[211] A. Tanjaroon Ly. VariationalMC.jl. `https://github.com/atanjaro/VariationalMC.jl`, 2025.

[212] C. P. J. Adolphs and M. Berciu. Going beyond the linear approximation in describing electron-phonon coupling: Relevance for the Holstein model. *Europhysics Letters*, 102(4):47003, jun 2013.

[213] Nandini Trivedi and Mohit Randeria. Deviations from Fermi-Liquid Behavior above T_c in 2D Short Coherence Length Superconductors. *Phys. Rev. Lett.*, 75:312–315, Jul 1995.

APPENDICES

APPENDIX 1:
SPIN AND CHARGE STRIPE EVOLUTION IN VMC AND DQMC SIMULATIONS

Figures A.1 and A.2 summarize our VMC results for the evolution of the stripe correlations as a function of λ and Ω. Results are shown for $t' = 0$ and $t' = -0.25t$ in Figures A.1 and A.2, respectively. The evolution of the antiferromagnetic and d-wave superconducting order parameters used to define the uniform variational wavefunctions shown in the main text and here are plotted in Figure A.3. Figures A.4-A.7 provide additional DQMC results.

Our VMC results indicated that the e-ph interaction can change the stripes from being site-centered to bond-centered for some model parameters. Table A.1 summarizes which kind of stripe we've observed for each of the parameter sets we've examined.

Table A.1: The type of stripe correlations found in our VMC calculations, distinguishing between bond- and site-centered. Entries listed as "-" were not explicitly checked.

λ	t'/t	$\Omega/t = 1$	$\Omega/t = 2$	$\Omega/t = 3$	$\Omega/t = 4$	$\Omega/t = 5$
0	0	bond	bond	bond	bond	bond
0.25	0	bond	bond	bond	bond	bond
0.5	0	bond	bond	bond	bond	bond
0.625	0	bond	bond	bond	bond	bond
0.75	0	bond	bond	bond	site	bond
1	0	bond	bond	-	-	-
0	-0.25	site	site	site	site	site
0.25	-0.25	bond	bond	bond	bond	bond
0.5	-0.25	bond	bond	bond	bond	bond
0.625	-0.25	bond	bond	bond	bond	site
0.75	-0.25	bond	bond	-	-	-

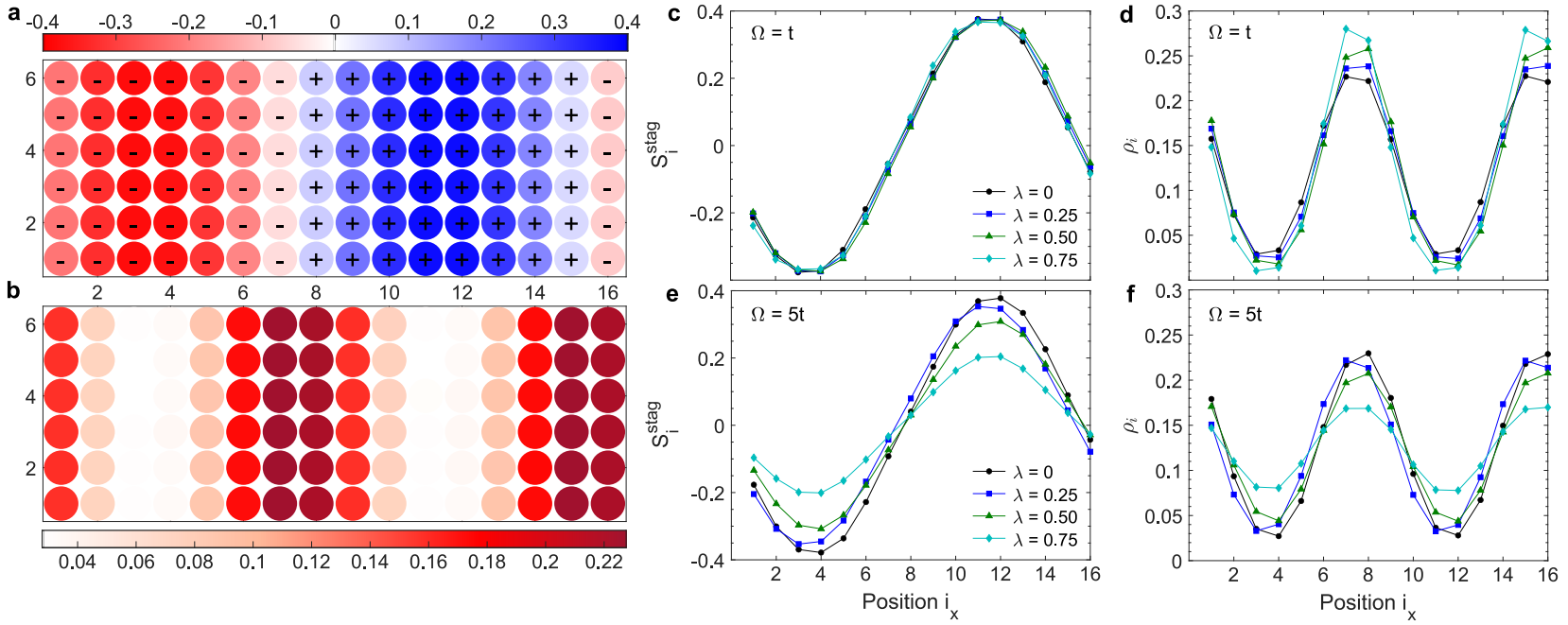

Figure A.1: Variational Monte Carlo results for static spin and charge stripes in the Hubbard-Holstein model with $U = 8t$ and $t' = 0$. (a) The expectation value of the staggered local spin operator in real space $S_i^{\text{stag}} = (-1)^{i_x+i_y}\langle \hat{S}_i^z \rangle$ and $\lambda = 0$, where $S_i^z = \frac{1}{2}(\hat{n}_{i,\uparrow} - \hat{n}_{i,\downarrow})$ is the z-component of the local spin operator. (b) The expectation value of the excess hole density $\rho_i = 1 - \sum_\sigma \langle \hat{n}_{i,\sigma} \rangle$ for the same case. Panels (c) and (d) show S_i^{stag} and ρ_i, respectively, along the line $(i_x, 0)$ for several values of λ when $\Omega = t$, while panels (e) and (f) show analogous results for a large $\Omega = 5t$. The statistical error bars in this figure are smaller than the data points.

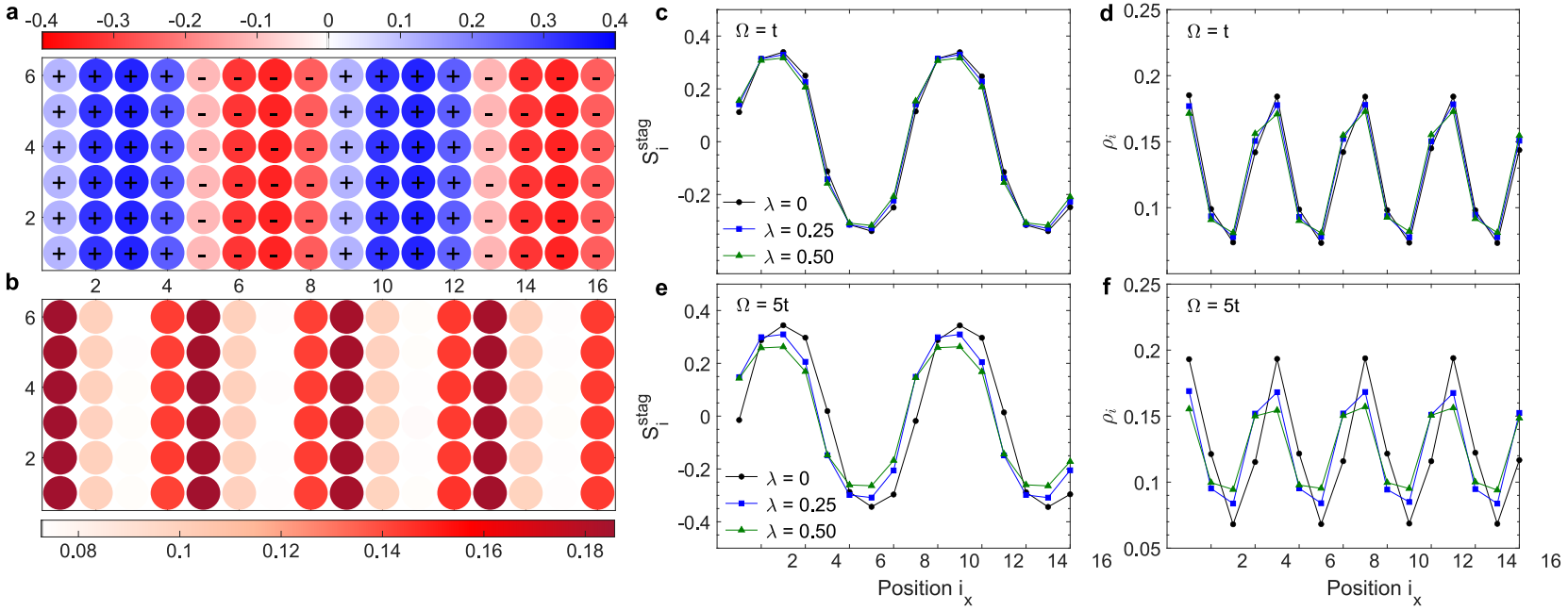

Figure A.2: Variational Monte Carlo results for static spin and charge stripes in the Hubbard-Holstein model with $U = 8t$ and $t' = -0.25t$. (a) The expectation value of the staggered local spin operator in real space $S_i^{\text{stag}} = (-1)^{i_x+i_y}\langle \hat{S}_i^z \rangle$ and $\lambda = 0$, where $S_i^z = \frac{1}{2}(\hat{n}_{i,\uparrow} - \hat{n}_{i,\downarrow})$ is the z-component of the local spin operator. (b) The expectation value of the excess hole density $\rho_i = 1 - \sum_\sigma \langle \hat{n}_{i,\sigma} \rangle$ for the same case. Panels (c) and (d) show S_i^{stag} and ρ_i, respectively, along the line $(i_x, 0)$ for several values of λ when $\Omega = t$, while panels (e) and (f) show analogous results for a large $\Omega = 5t$. The statistical error bars in this figure are smaller than the data points.

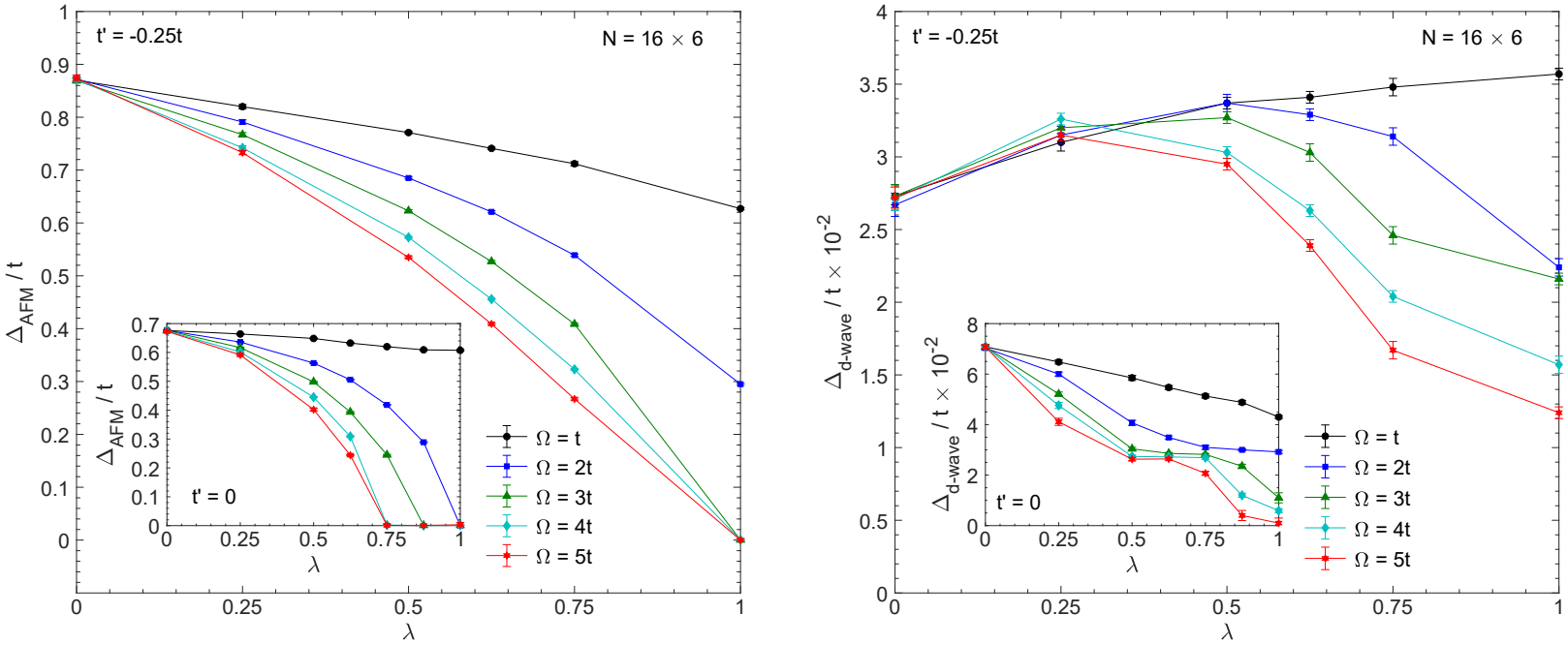

Figure A.3: The evolution of the antiferromagnetic (left) and d-wave superconducting order parameters used to define the variational wavefunctions shown in the main text as a function of λ. The error bars represent 1σ statistical error bars.

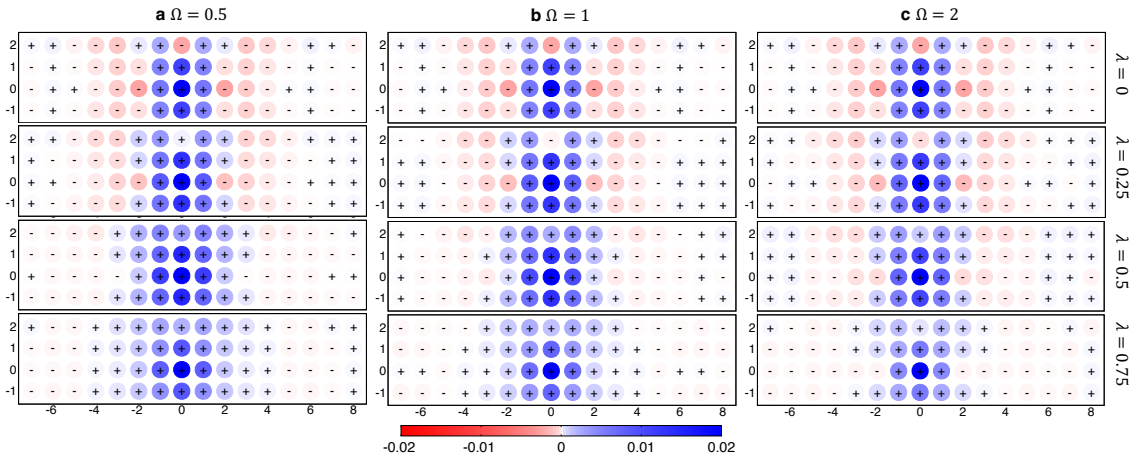

Figure A.4: DQMC results for the fluctuating spin stripes in the Hubbard-Holstein model at a filling of $\langle \hat{n} \rangle = 0.8$ and an inverse temperature of $\beta = 4/t$ and obtained on $N = 16 \times 4$ clusters with $t' = -0.25t$ and $U = 6t$. Each row and column shows the real-space static staggered spin-spin correlation function at different values of λ and Ω, respectively.

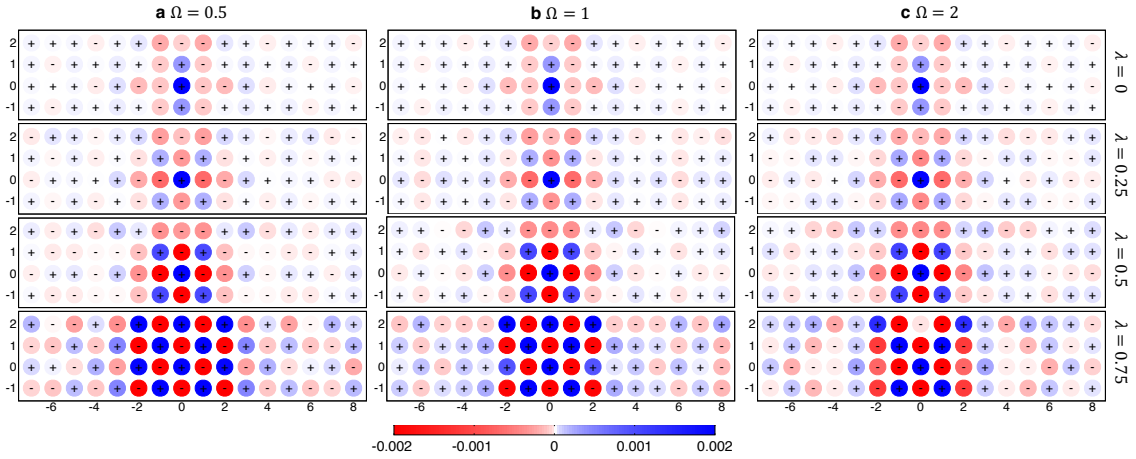

Figure A.5: DQMC results for the fluctuating charge stripes in the Hubbard-Holstein model at a filling of $\langle \hat{n} \rangle = 0.8$ and an inverse temperature of $\beta = 4/t$ and obtained on $N = 16 \times 4$ clusters with $t' = -0.25t$ and $U = 6t$. Each row and column show the real-space static staggered density-density correlation function at different values of λ and Ω, respectively.

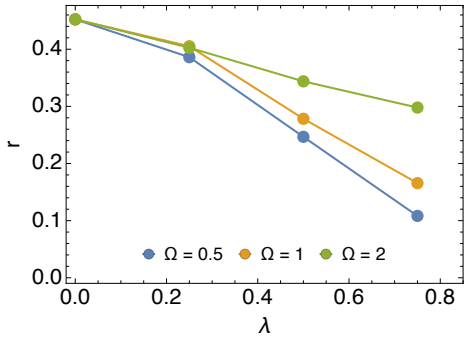

Figure A.6: DQMC results of the ratio between spin and charge incommensurability $r = \delta_s/\delta_c$ in the Hubbard-Holstein model at a filling of $\langle \hat{n} \rangle = 0.8$ and an inverse temperature of $\beta = 4/t$. Results were obtained on $N = 16{\times}4$ clusters with $t' = -0.25t$ and $U = 6t$ for different values of Ω.

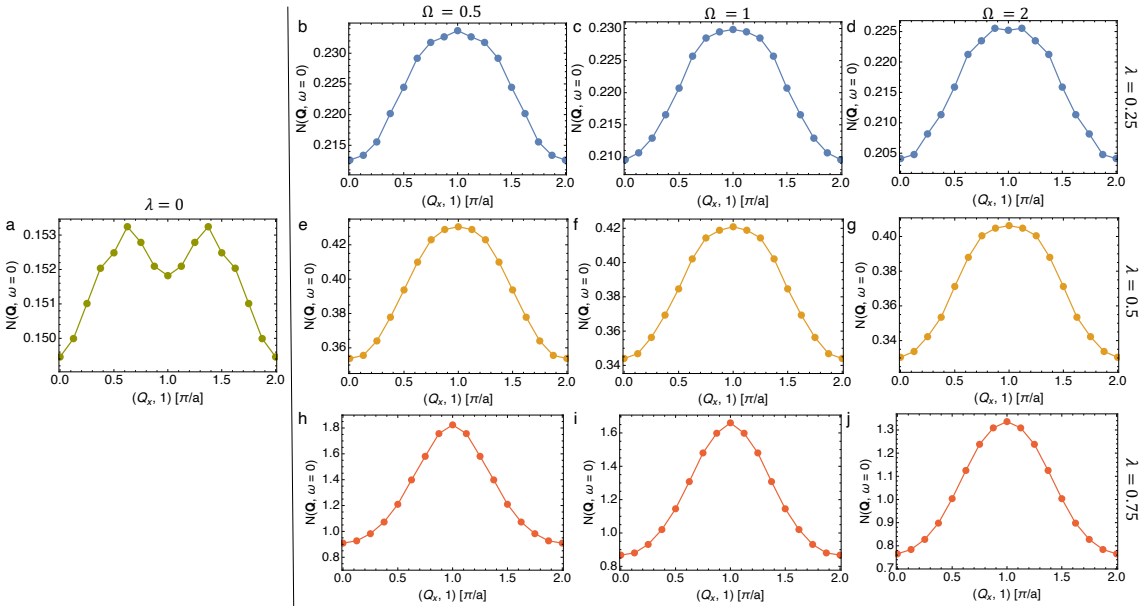

Figure A.7: DQMC results for the fluctuating charge stripes in the Hubbard-Holstein model at a filling of $\langle \hat{n} \rangle = 0.8$ and an inverse temperature of $\beta = 4/t$ and obtained on $N = 16 \times 4$ clusters with $t' = -0.25t$ and $U = 6t$. The panels show the static charge susceptibility at $Q_y = \pi$ as a function of Q_x for different values of λ and Ω.

APPENDIX 2:
FINITE SIZE EFFECTS IN VMC SIMULATIONS

In Chapter 3, we focused on VMC results obtained on rectangular 16×6 clusters. This cluster geometry supports several different potential stripe periods, allows us to draw more direct parallels between the VMC and DQMC results, and is computationally cheaper than square geometries of a comparable size. However, this geometry might also bias the solution towards stripe formation. For this reason, it is important to assess any finite size effects that might occur from this choice of this geometry.

Our results obtained on rectangular clusters for $\lambda = 0$ are in good agreement with Ref. [14], who studied the Hubbard model on 16×16 square clusters. This agreement suggests that any finite size effects associated with our rectangular geometry won't change our qualitative conclusions. To verify this, we performed additional calculations for $t' = -0.25t$, $U = 8t$, $\Omega = t$, and $\lambda = 0.25$ using $16 \times L_y$ clusters, with $L_y = 4 - 12$. The results, summarized in Figure B.1, indicate that there are some finite size effects in the quantitative results but that they do not alter our overall conclusions. For example, increasing the width of the cluster produces slight changes (on the order of 1% of t) in the variational energies but it does not produce a d-wave state with a lower variational energy in comparison to the stripe state.

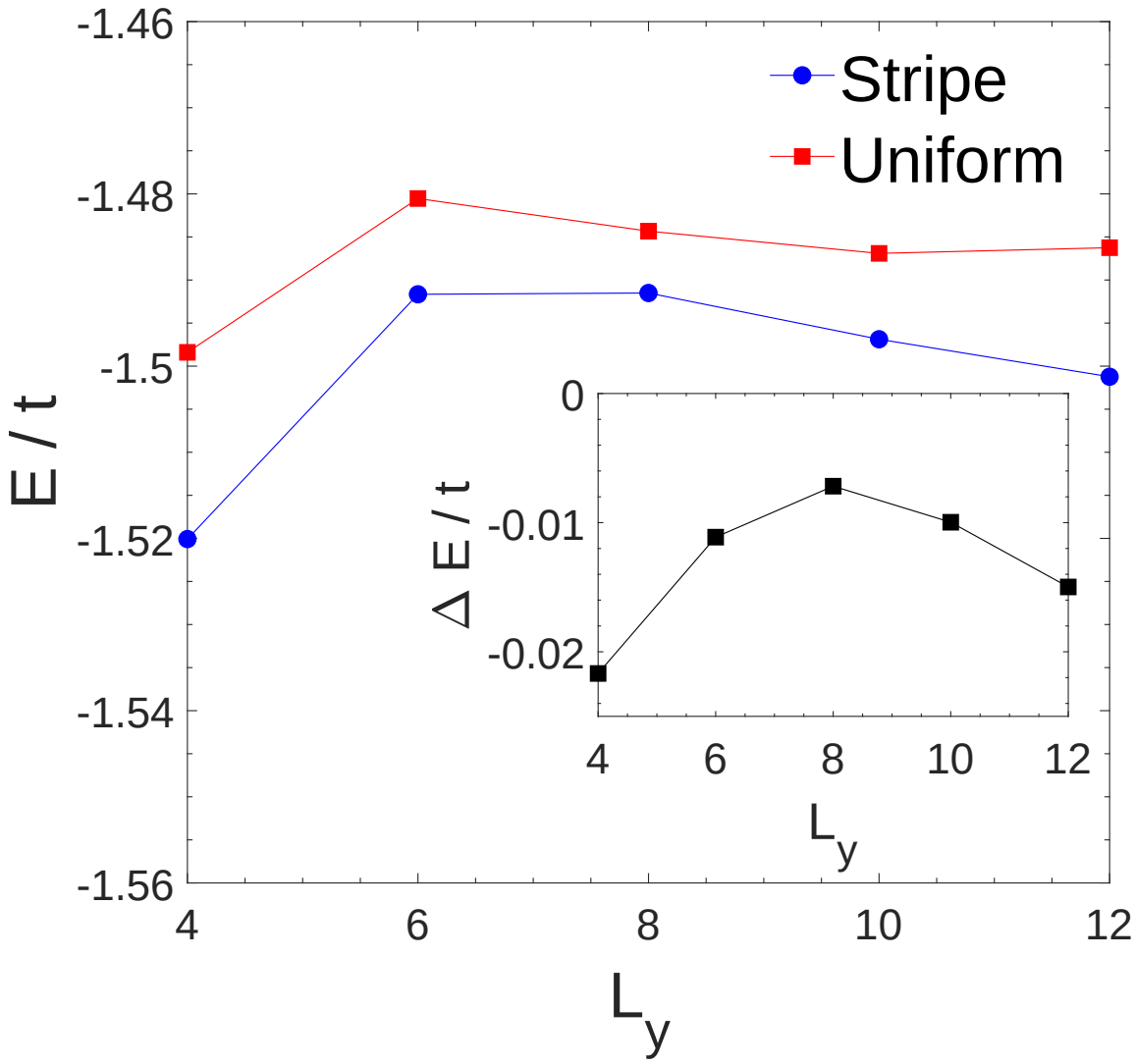

Figure B.1: The energies of the variational wave functions obtained on $16 \times L_y$ clusters with model parameters $t' = -0.25t$, $U = 8t$, $\Omega = t$, and $\lambda = 0.25$. Results are shown for states with uniform d-wave correlations (red squares) or stripe correlations (blue squares). The inset plots the difference in the variational energies $\Delta E = E_{\text{stripe}} - E_{\text{uniform}}$. Increasing the width of the rectangular cluster produces small variations in the variational energy, demonstrating that our quantitative results have some finite size dependence. However, increasing L_y does not lower the energy of the d-wave state below that of the stripe state. The statistical error bars in this figure are smaller than the data points.

APPENDIX 3:
SIGN CHANGES IN THE EFFECTIVE HOPPING INTEGRAL IN THE SU-SCHRIEFFER-HEEGER MODEL

Both the optical- and bond-SSH models approximate the nonlinear dependence of the hopping integrals on the atomic displacements within the linear approximation. At this level, both models allow the sign of the effective hopping integral to change when the lattice displacements become sufficiently large, which is frequently overlooked in non-perturbative numerical simulations. In principle, one can suppress the frequency of these sign changes by including nonlinear e-ph interactions [212] or additional anharmonic terms in the lattice potential [140], which tend to reduce the size of the lattice displacements found in the linear model. However, these terms can significantly affect the pairing and charge correlations in the linear model [184] and prevent comparisons to works that didn't include these interactions. For this reason, we have chosen to simulate the optical- and bond-SSH models as they are formulated in the linear approximation and not artificially prevented Monte Carlo updates that produce a sign change in the effective hopping.

To assess the severity of this problem, Fig. C.1 plots the percentage of times the effective hopping changes sign during our DQMC simulations for both the bond- and optical-SSH models. Note that we do *not* average the phonon positions over imaginary time before calculating this percentage. Results are shown here for $\Omega = 4t$, $\beta = 16/t$, $N = 14 \times 14$, and as a function of $\langle n \rangle$. Sign switching occurs more frequently in the optical model for fixed $\lambda = 0.3$, which can be understood once one recognizes that the displacement of two atoms controls the bond distance in the optical model. The bifurcation of the results for the optical-SSH model is due to forming the BOW phase, where inequivalent bond lengths appear along the x- and y- directions.

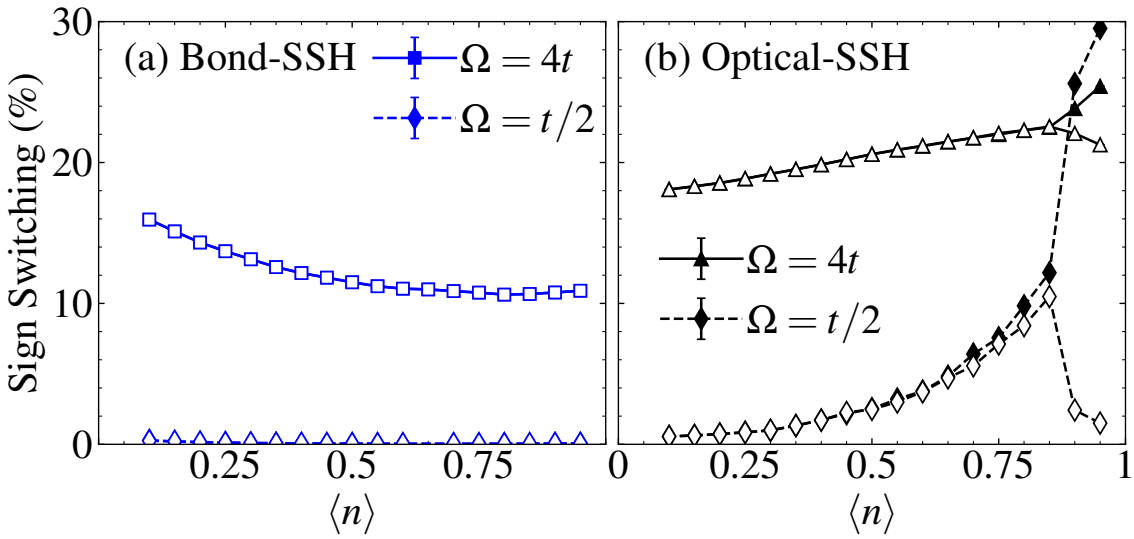

Figure C.1: Sign switching of the hopping integral as a function of filling for (a) the bond-SSH model in the x-direction (closed □) and in the y-direction (open □). Also shown are complementary results for (b) the optical-SSH model (closed and open △). All results for $\lambda = 0.3$ at $\beta t = 16$ on an $N = 14 \times 14$ cluster.

APPENDIX 4:
THE FERMION SIGN PROBLEM AND FINITE SIZE EFFECTS IN DQMC SIMULATIONS

The Holstein and SSH models considered Chapter 4 can be simulated with DQMC without a sign problem. However, all three models develop a sign problem once we include the Hubbard interaction [130] when doped away from half-filling. (Only the bond and optical-SSH models at half-filling remain sign-problem-free.) For reference, Figure D.1 plots the average value of the Fermion sign obtained for the simulations presented in Fig. 4.5 with a finite $U = t/2$. Interestingly, the bond-SSH model appears to have a less severe sign problem than the optical-SSH model.

Figure D.2 assesses the finite size effects for our simulations of the Holstein, bond-, and optical-SSH models. Here we fix the simulation parameters to $\Omega = 4t$, $\lambda = 0.3$, and $\beta = 16/t$ and vary carrier concentrations over $0 < \langle n \rangle < 1$. (Our model is particle-hole symmetric when $\mu = 0$ as we only include the nearest-neighbor hopping t.) The left column of Fig. D.2 plots the uniform s-wave pair-field susceptibility for the Holstein [Fig. D.2a], bond-SSH [Fig. D.2b], and optical-SSH [Fig. D.2c] models, respectively. Similarly, the right column of Fig. D.2 plots each model's dominant charge/bond order. Specifically, Fig. D.2d plots the $\mathbf{q} = (\pi, \pi)$ charge correlations for the Holstein model, while Figs. Fig. D.2e and Fig. D.2f plot the $\mathbf{q} = (\pi, \pi)$ bond susceptibilities for the bond- and optical-SSH models, respectively. The results indicate that all three models exhibit noticeable finite-size effects; however, the overall qualitative behavior remains the same across all system sizes. As the cluster size increases, there is an overall increase in the strength of the pairing correlations, which is accompanied by a shift of the peak position toward half-filling. At the same time, the strength of the CDW (BOW) correlations in the Holstein (optical-SSH) model near $\langle n \rangle = 1$ increase with cluster size, consistent with the presence of long-range order at this filling. Conversely, the strength of the BOW correlations in the bond-SSH model exhibits a much weaker finite size

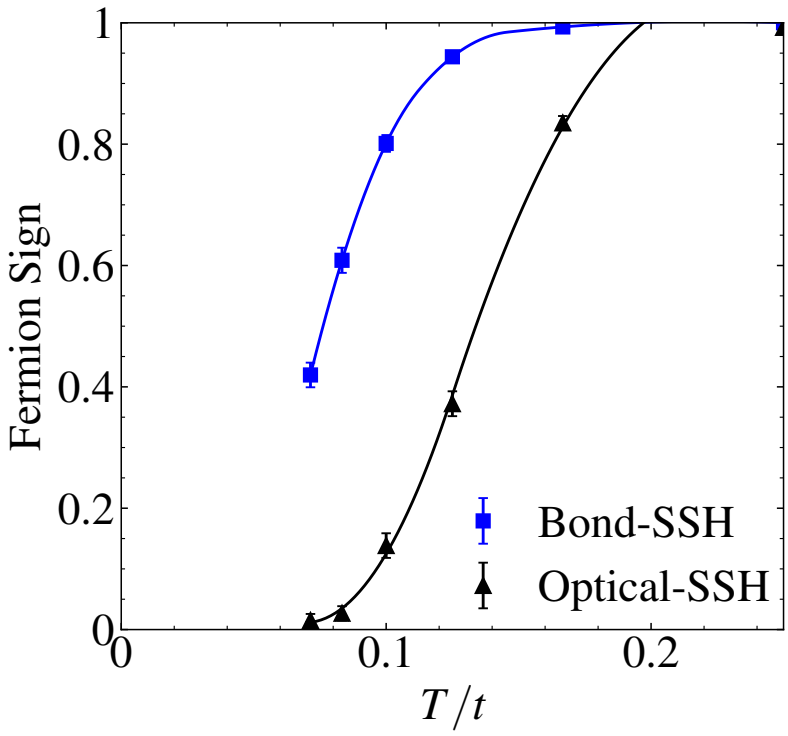

Figure D.1: The average value of the Fermion sign obtained for the simulations with $U = t/2$ presented in Fig. 4.5 of Chapter 4.

dependence, consistent with short-range correlations. Finally, all three models' charge and bond susceptibilities show a weaker dependence on cluster size for fillings less than $\langle n \rangle \lesssim 0.75$.

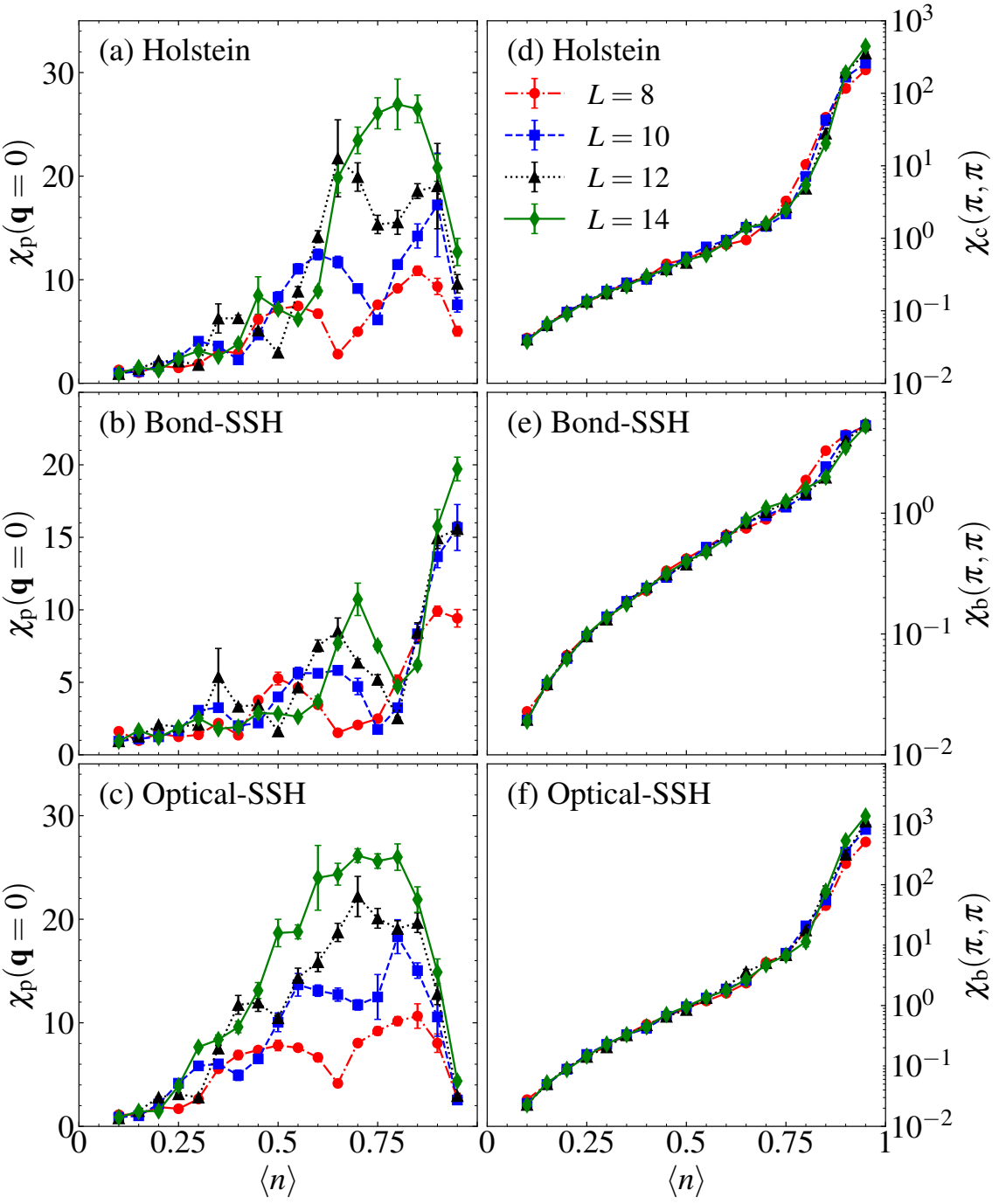

Figure D.2: All panels are DQMC results for $\Omega = 4t$, $\lambda = 0.3$ at $\beta t = 16$ on different $L \times L$ lattices. Panels (a) and (b) show the uniform ($q = 0$) s-wave pair-field $\chi_p(\mathbf{q})$ and $\mathbf{q} = (\pi, \pi)$ charge-density-wave $\chi_c(q)$ susceptibilities for the Holstein model. Panels (c) and (d) show χ_p and $\mathbf{q} = (\pi, \pi)$ bond-ordered-wave $\chi_b(\mathbf{q})$ susceptibility for the bond-SSH model. Similarly, panels (e) and (f) show χ_p and χ_b for the optical-SSH model.

APPENDIX 5:
EFFECTIVE INTERACTION OF THE OPTICAL SSH MODEL IN THE ANTI-ADIABATIC LIMIT

The action of the oSSH model on the imaginary time axis is given by

$$\begin{aligned} S\left[\bar{\psi},\psi,X\right] = \int \mathrm{d}\tau \sum_{i,\nu} \Bigg[& \bar{\psi}\partial_\tau \psi - t\hat{B}_{i,i+a_\nu} + \frac{M}{2}\left(\partial_\tau \hat{X}_{i,\nu}\right)^2 \\ + \quad & \frac{K}{2}X_{i,\nu}^2 + \alpha\left(\hat{X}_{i+a_\nu,\nu} - \hat{X}_{i,\nu}\right)\hat{B}_{i,i+a_\nu}\Bigg], \end{aligned} \tag{E.1}$$

where ν runs over the $\hat{x}$ and $\hat{y}$ spatial dimensions. Here, $a_x = (a,0)$ and $a_y = (0,a)$ are the primitive lattice vectors, $\hat{X}_{i,\nu}$ is the position operator for the atom at site i along each of the directions ν of the lattice, and $\hat{B}_{i,i+a_\nu} = \sum_\sigma \left(\bar{\psi}_i \psi_{i+a_\nu} + \mathrm{H.c.}\right)$ is the bond operator between lattice sites i and $i + a_\nu$.

In the anti-adiabatic limit, $M \to 0$ (or $\Omega \to \infty$) and the phonon kinetic term drops out of the integral

$$\begin{aligned} S\left[\bar{\psi},\psi,X\right] = \int \mathrm{d}\tau \sum_{i,\nu} \Bigg[& \bar{\psi}\partial_\tau \psi - t\hat{B}_{i,i+a_\nu} + \frac{K}{2}X_{i,\nu}^2 \\ & + \alpha\left(\hat{X}_{i+a_\nu,\nu} - \hat{X}_{i,\nu}\right)\hat{B}_{i,i+a_\nu}\Bigg]. \end{aligned} \tag{E.2}$$

Next, we redefine the *e*-ph interaction term to an equivalent form

$$\sum_{i,\nu} \alpha\left(\hat{X}_{i+a_\nu,\nu} - \hat{X}_{i,\nu}\right)\hat{B}_{i,i+a_\nu} = \sum_{i,\nu} \alpha \hat{X}_{i,\nu}\left(\hat{B}_{i,i+a_\nu} - \hat{B}_{i,i-a_\nu}\right). \tag{E.3}$$

This form allows us to complete the square and obtain

$$\begin{aligned} S[\bar{\psi},\psi,X] &= \int \mathrm{d}\tau \sum_{i,\nu} \left[\bar{\psi}\partial_\tau \psi - t\hat{B}_{i,i+a_\nu} + \frac{K}{2}X_{i,\nu}^2 + \alpha \hat{X}_{i,\nu}\left(\hat{B}_{i,i+a_\nu} - \hat{B}_{i,i-a_\nu}\right)\right] \\ &= \int \mathrm{d}\tau \sum_{i,\nu} \left\{ \bar{\psi}\partial_\tau \psi - t\hat{B}_{i,i+a_\nu} + \frac{K}{2}\left[X_{i,\nu} + \frac{\alpha}{K}\left(\hat{B}_{i,i+a_\nu} - \hat{B}_{i,i-a_\nu}\right)\right]^2 \right. \\ &\quad \left. - \frac{\alpha^2}{K}\left(\hat{B}_{i,i+a_\nu} - \hat{B}_{i,i-a_\nu}\right)^2 \right\} \\ &= \int \mathrm{d}\tau \sum_{i,\nu} \left[\bar{\psi}\partial_\tau \psi - t\hat{B}_{i,i+a_\nu} - \frac{\alpha^2}{K}\left(\hat{B}_{i,i+a_\nu} - \hat{B}_{i,i-a_\nu}\right)^2 \right], \end{aligned} \tag{E.4}$$

where we have explicitly integrated out the phonons in the last step. Expanding the $\left(\hat{B}_{i,i+a_\nu} - \hat{B}_{i,i-a_\nu}\right)^2$ term, we then obtain

$$\begin{aligned} S[\bar{\psi},\psi,X] &= \int \mathrm{d}\tau \sum_{i,\nu} \left[\bar{\psi}\partial_\tau \psi - t\hat{B}_{i,i+a_\nu} \right. \\ &\quad \left. - \frac{\alpha^2}{K}\left(\hat{B}_{i,i+a_\nu}^2 + \hat{B}_{i,i-a_\nu}^2 - \hat{B}_{i,i+a_\nu}\hat{B}_{i,i-a_\nu} - \hat{B}_{i,i-a_\nu}\hat{B}_{i,i+a_\nu}\right)\right] \\ &= \int \mathrm{d}\tau \sum_{i,\nu} \left[\bar{\psi}\partial_\tau \psi + \left(-t\hat{B}_{i,i+a_\nu} - \frac{\alpha^2}{K}\hat{B}_{i,i+a_\nu}^2 \right) \right. \\ &\quad \left. - \frac{\alpha^2}{K}\left(\hat{B}_{i,i-a_\nu}^2 - \hat{B}_{i,i+a_\nu}\hat{B}_{i,i-a_\nu} - \hat{B}_{i,i-a_\nu}\hat{B}_{i,i+a_\nu}\right)\right] \\ &= \int \mathrm{d}\tau \sum_{i,\nu} \left[\bar{\psi}\partial_\tau \psi - \left(t\hat{B}_{i,i+a_\nu} + \frac{2\alpha^2}{K}\hat{B}_{i,i+a_\nu}^2 \right) \right. \\ &\quad \left. + \frac{\alpha^2}{K}\left(\hat{B}_{i,i+a_\nu}\hat{B}_{i,i-a_\nu} + \hat{B}_{i,i-a_\nu}\hat{B}_{i,i+a_\nu}\right)\right]. \end{aligned} \tag{E.5}$$

The term $-(t\hat{B}_{i,i+a_\nu} + \frac{2\alpha^2}{K}\hat{B}_{i,i+a_\nu}^2)$ is also obtained in the bSSH model and it produces an effective Heisenberg-like Hamiltonian with an antiferromagnetic $J = 2\alpha^2/K$ [199]. Here, however, we have additional terms proportional to α^2/K. We can expand the products of operators and rearrange terms

$$
\begin{aligned}
&\frac{\alpha^2}{K}\sum_{i,\nu}\left(\hat{B}_{i,i+a_\nu}\hat{B}_{i,i-a_\nu}+\hat{B}_{i,i-a_\nu}\hat{B}_{i,i+a_\nu}\right)\\
&\qquad=-\frac{2\alpha^2}{K}\Bigg[\sum_{i,\nu}\sum_{\sigma}\left(c^\dagger_{i-a_\nu,\sigma}n_{i,\sigma}c_{i+a_\nu,\sigma}\;+\;c^\dagger_{i+a_\nu,\sigma}n_{i,\sigma}c_{i-a_\nu,\sigma}\right)\\
&\qquad+\sum_{i,\nu}\sum_{\sigma\neq\sigma'}\left(c^\dagger_{i+a_\nu,\sigma}c^\dagger_{i,\sigma'}c_{i,\sigma}c_{i-a_\nu,\sigma'}\;+\;c^\dagger_{i-a_\nu,\sigma}c^\dagger_{i,\sigma'}c_{i,\sigma}c_{i+a_\nu,\sigma'}\right)\Bigg]\\
&\qquad+\frac{\alpha^2}{K}\sum_{i,\nu}\hat{B}_{i+a_\nu,i-a_\nu},
\end{aligned}
\tag{E.6}
$$

where $\hat{B}_{i+a_\nu,i-a_\nu}=\sum_\sigma\left(c^\dagger_{i+a_\nu,\sigma}c_{i-a_\nu,\sigma}+\text{h.c}\right)=\sum_\sigma\left(\bar{\psi}_{i+a_\nu,\sigma}\psi_{i-a_\nu,\sigma}+\text{h.c}\right)$. The first term represents a hopping interaction that allows an electron to hop between next-nearest neighbor sites along the $\hat{x}$ or $\hat{y}$ directions with amplitude $2\alpha^2/K$ depending upon the density of the intermediate site. The second term represents an interaction that shifts a bond pair by one site. The final term allows electrons to hop between next-nearest neighbors along the crystallographic directions with amplitude α^2/K.

APPENDIX 6:
ADDITIONAL OBSERVABLES IN THE SSH-HUBBARD MODEL

To assess the transport properties of the system, we measured the system's compressibility $\kappa = \frac{\mathrm{d}\langle n \rangle}{\mathrm{d}\mu}$ and local Green's function $\beta G(r = 0, \tau = \beta/2)$ for an $L = 8$ cluster at $\beta t = 16$. The compressibility $\kappa = 0$ ($\neq 0$) for an insulating (metallic) system. Conversely, the local Green's function provides a measure of the integrated spectral weight near the Fermi energy [213]. Fig. F.1a plots the compressibility in the (λ, U)-plane. It is non-zero for $U \lesssim 2$ and $\lambda \lesssim 0.1$ indicating that this region of the phase diagram is metallic at this temperature. $\kappa = 0$ throughout the remainder of the phase diagram. Fig. F.1b plots the single particle Green's function. It is also largest in the same region where $\kappa \neq 0$.

Figure F.2 shows additional correlation ratio crossings for $U/t \in [0, 8]$ as indicated in each panel. Each (a) panel plots the BOW correlation ratios while each (b) panel plots the AFM correlation ratios. Next, we assess the low temperature AFM susceptibility and equal-time structure factors of the pure oSSH model ($U/t = 0$). Figs. F.3a and F.3b plot the AFM susceptibility χ_{AFM} obtained on an $L = 14$ cluster for $\beta t = 14$ and $\beta t = 28$, respectively, and two different phonon energies. For $\Omega/t = 0.5$, there is a weak enhancement in χ_{AFM} compared to the non-interacting ($\lambda = 0$) case. Increasing the phonon energy to $\Omega/t = 2$ results in a slightly larger enhancement. The dashed lines in each panel indicate the bond-order-wave quantum critical points λ_c^{BOW} for the two phonon frequencies. In this case, χ_{AFM} is suppressed with the onset of long-range BOW order.

Figs. F.3c and F.3d plot the corresponding structure factor S_{AFM}. Here we also observe a slight increase in the strength of the AFM correlations but the degree of the enhancement is much smaller than in the susceptibility. Since the latter integrates over all imaginary time fluctuations, this behavior is consistent with the presence of increased short-range fluctuating AFM correlations and a lack of long-range magnetic order at this temperature.

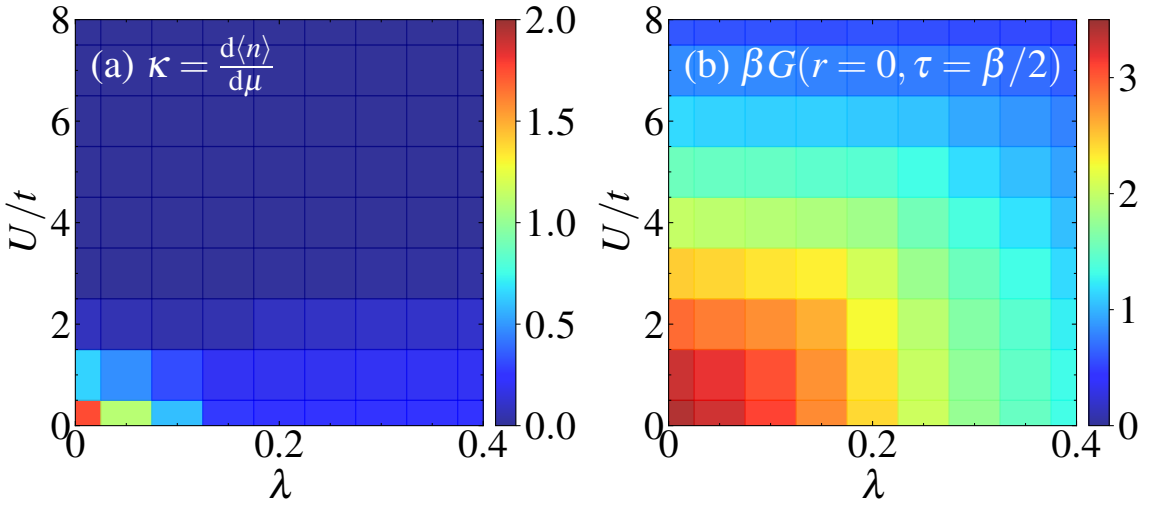

Figure F.1: The (a) compressibility κ and (b) local single particle Green's function $\beta G(r = 0, \tau = \beta/2)$ for the optical SSH-Hubbard model as a function of λ and U. All results are for an $L = 8$ cluster at $\beta t = 16$ with $\Omega/t = 0.5$.

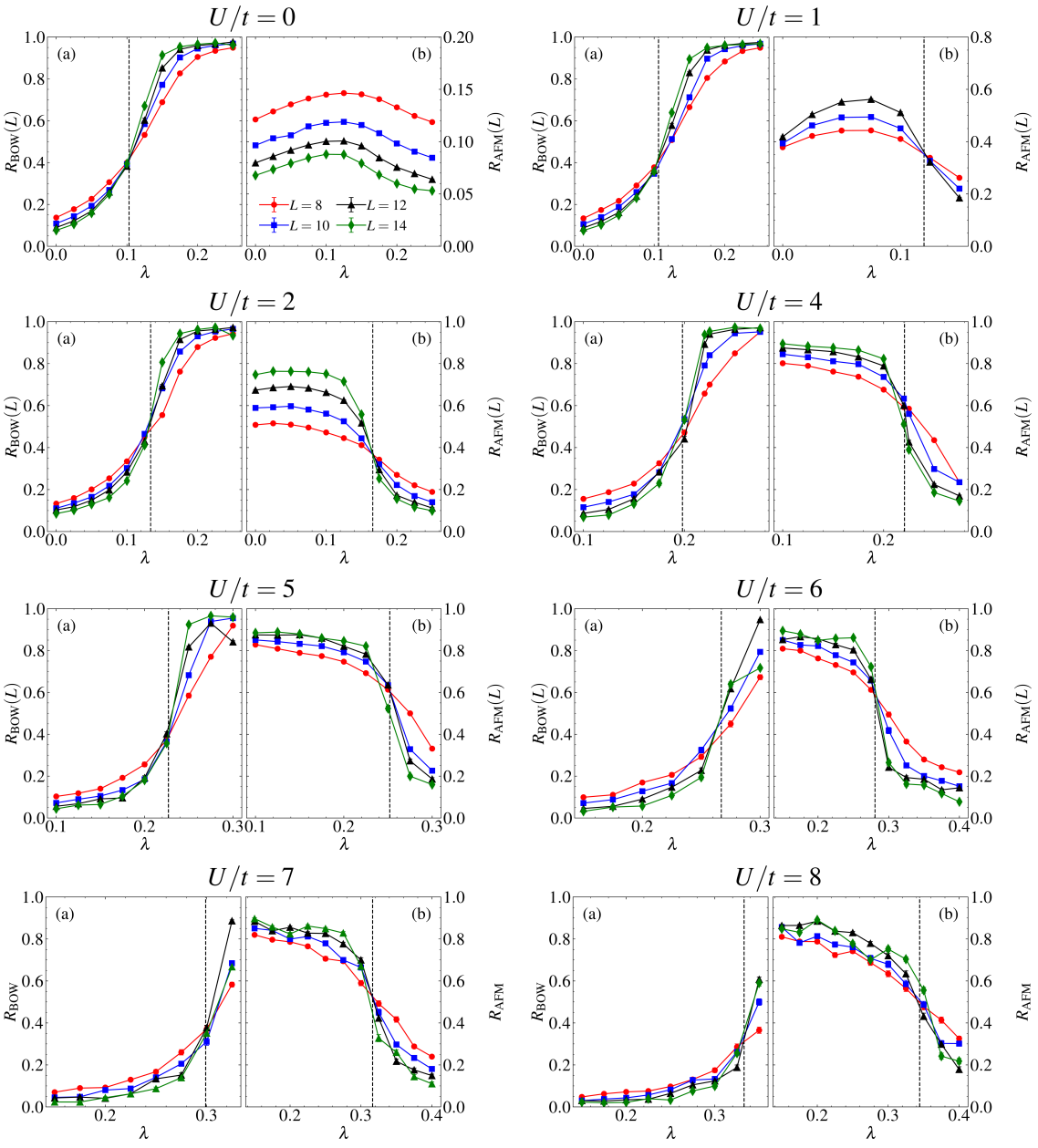

Figure F.2: (a) Bond-ordered-wave and (b) antiferromagnetic (AFM) correlation ratios for $U/t \in [0, 8]$, as indicated in each subplot. The dashed black line indicates the location of the quantum critical point (QCP).

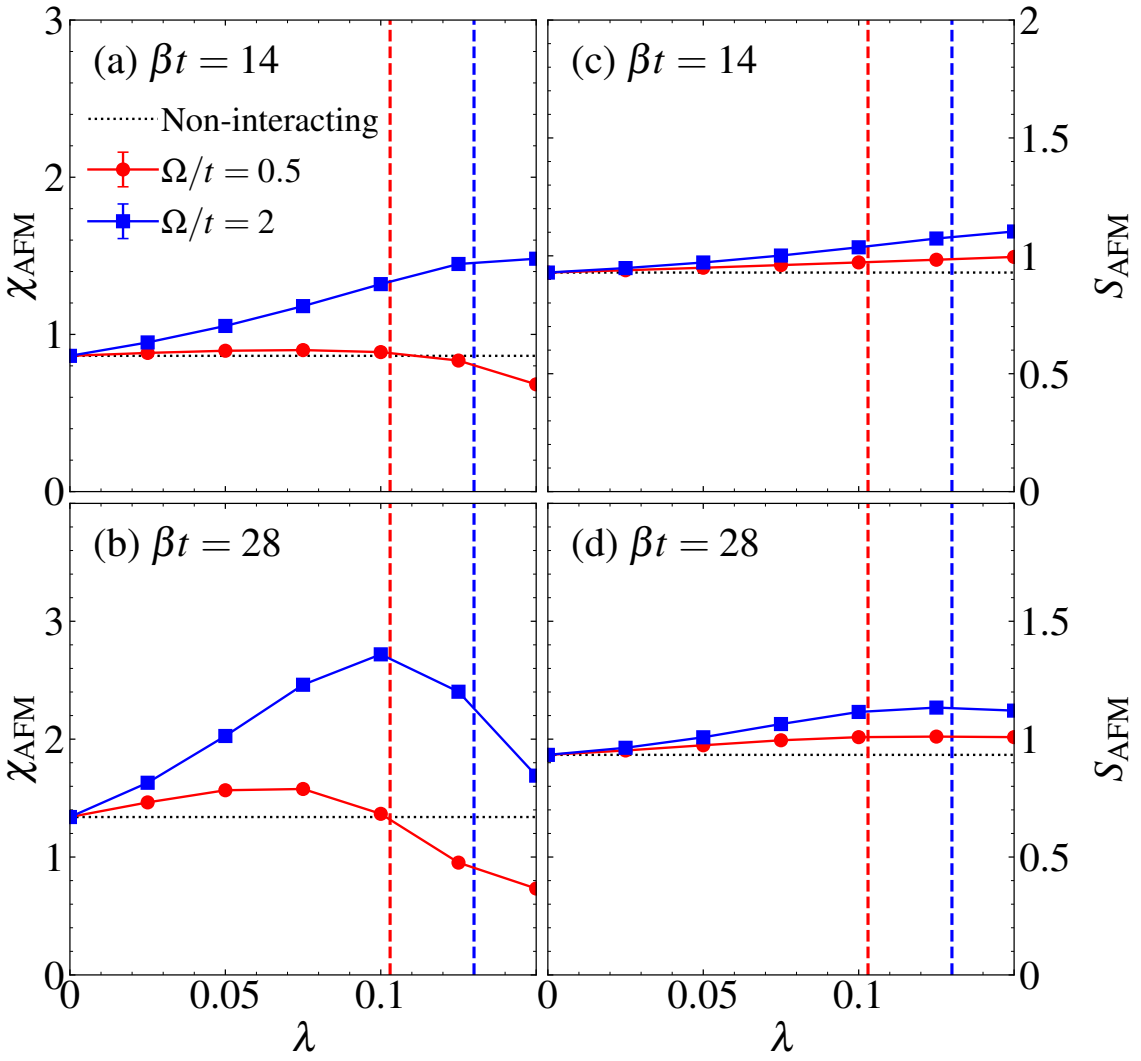

Figure F.3: Antiferromagnetic susceptibility χ_{AFM} for $L = 14$, $\Omega/t = 0.5$ and 2, $\beta t = 14$ [panel (a)], and $\beta t = 28$ [panel (b)] compared to the non-interacting solution (black dotted line). The vertical dashed lines denote the value of λ_c^{BOW} for each respective phonon frequency. The corresponding antiferromagnetic structure factors S_{AFM} are shown in panels (c) and (d).

CITATIONS TO PUBLISHED WORK

Primary works:

Stripe correlations in the two-dimensional Hubbard-Holstein model

S. Karakuzu, **A. Tanjaroon Ly**, P. Mai, J. Neuhaus, T.A. Maier and S. Johnston. *Communications Physics* **5**, 311 (2022)
DOI:10.1038/s42005-022-01092-x

Comparative study of the superconductivity in the Holstein and optical Su-Schrieffer-Heeger models

A. Tanjaroon Ly, B. Cohen-Stead, S.M. Costa and S. Johnston. *Physical Review B* **108**, 184501 (2023) **Editor's Suggestion**
DOI:10.1103/PhysRevB.108.184501

Antiferromagnetic and bond-order-wave phases in the two-dimensional optical Su-Schrieffer-Heeger-Hubbard model

A. Tanjaroon Ly, B. Cohen-Stead and S. Johnston. *Physical Review B* **111**, 245138 (2025)
DOI:10.1103/2bnf-tmtc

Other research contributions:

Comparative determinant quantum Monte Carlo study of the acoustic and optical variants of the Su-Schrieffer-Heeger model

S.M. Costa, B. Cohen-Stead, **A. Tanjaroon Ly**, J. Neuhaus and S. Johnston. *Physical Review B* **108**, 165138 (2023)
DOI:10.1103/PhysRevB.108.165138

SmoQyDQMC.jl: A flexible implementation of determinant quantum Monte Carlo for Hubbard and electron-phonon interactions

B. Cohen-Stead, S.M. Costa, J. Neuhaus, **A. Tanjaroon Ly**, Y. Zhang, R.T. Scalettar and S. Johnston. *SciPost Physics Codebases* **29** (2024) DOI:10.21468/scipostphyscodeb.29

VITA

Andy Tanjaroon Ly was born and raised in Saint Petersburg, Florida. After reading Richard Feynman's *Six Easy Pieces* and watching too many episodes of *Star Trek: The Next Generation*, he was enamored by the world of physics. He would go on to earn a B.S. in Physics and a B.A. in Mathematics from the University of Florida in 2018.

In August 2019, he began his Ph.D. in Physics at the University of Tennessee-Knoxville. After two years as a Graduate Teaching Assistant, he joined the research group of Professor Steven Johnston as a Graduate Research Assistant. His research focused on investigating orders in strongly correlated lattice models using Monte Carlo methods. He was a visiting Graduate Student at the University of Geneva and was awarded the Department of Energy Office of Science Graduate Student Research (SCGSR) fellowship to work at Oak Ridge National Laboratory in 2024. He defended his doctoral dissertation on July 15, 2026.

In September 2026, he will begin a Postdoctoral Research fellowship as part of the Quanutum Horizons initiative at the University of Alberta, working under the supervision of Prof. Frank Marsiglio.